

Aus dem Institut für Molekular- und Zellbiologie der Hochschule Mannheim

Leiter: Prof. Dr. rer. nat. Mathias Hafner

Separation and characterization of antibody-based protein variants in
column chromatography for the production of biopharmaceuticals

Inauguraldissertation

zur Erlangung des Doctor scientiarum humanarum (Dr. sc. hum.)

der

Medizinischen Fakultät Mannheim

der Ruprecht-Karls-Universität

zu

Heidelberg

vorgelegt von

Gabriela Sánchez Reyes

aus

Ciudad Victoria

2021

Dekan: Prof. Dr. med. Sergij Goerd

Referent: Prof. Dr. rer. nat. Mathias Hafner

TABLE OF CONTENTS

	Page
LIST OF ABBREVIATIONS	1
LIST OF SYMBOLS	4
1 INTRODUCTION	10
1.1 Biopharmaceuticals - monoclonal antibodies	10
1.2 Purification of therapeutic drugs - chromatography	12
1.3 Ligand density variation in IEC	13
1.4 Aim of this work	15
2 MATERIALS AND METHODS	16
2.1 Electronic equipment.....	16
2.2 Computer programs	16
2.3 Chemicals	17
2.4 Chromatography resins	18
2.4.1 Preparative anion exchange resins.....	18
2.4.2 Preparative cation exchange resins.....	19
2.4.3 HPLC resins	20
2.5 Proteins and sample preparation.....	20
2.5.1 Purification of BSA.....	21
2.5.2 Buffer exchange of mAb03 and BSA	22

2.5.3	Purification of mAb04 charge variants	22
2.6	Mechanistic modeling of chromatographic separation processes	23
2.6.1	Ion exchange equilibrium model	24
2.6.2	Ligand density dependency on the stoichiometric displacement model.....	25
2.6.3	Linear gradient elution model	29
2.6.4	Donnan ion exchange model	31
2.6.5	Determination of the model parameters.....	32
2.6.5.1	Linear gradient elution experiments	32
2.6.5.1.1	Anion exchange LGE experiments.....	33
2.6.5.1.2	Cation exchange LGE experiments.....	34
2.6.6	Column simulation model	35
2.6.6.1	Inverse estimation of the mass transfer coefficient.....	36
2.7	Determination of column parameters	36
2.7.1	Dead volumes of the Äkta system	36
2.7.2	Column porosities	37
2.7.2.1	Anion exchange porosities	37
2.7.2.2	Cation exchange porosities	38
2.7.3	Exclusion factor	38
2.7.4	Ligand density	39
2.7.5	Axial dispersion.....	39
2.8	Analytical size exclusion chromatography (SEC)	40
2.9	Analytical cation exchange chromatography (CEX)	40
3	RESULTS.....	41
3.1	Modeling of anion exchange resins	41

3.1.1	AEX column parameters	41
3.1.2	Salt gradient elution of mAb03 and BSA in the linear range	42
3.1.2.1	Ligand density dependency in the stoichiometric displacement model.....	43
3.1.2.2	Ligand density dependency of the characteristic charge (<i>vi</i>)	47
3.1.2.3	Ligand density dependency of $\Delta Gi0/RT$ and $\Delta Gs0/RT$	48
3.1.2.4	<i>In silico</i> validation – Chromatogram simulation of AEX resins.....	50
3.1.2.5	Ligand density dependency of the characteristic charge (<i>vi</i>)	
	– a Donnan equilibrium in ion exchange chromatography.....	53
3.2	Modeling of cation exchange resins	56
3.2.1	Purification of mAb04 charge variants	56
3.2.1.1	Characterization of mAb04	56
3.2.1.2	Preparative cation exchange	57
3.2.2	CEX column parameters.....	59
3.2.2.1	Dead volumes of the Äkta system	59
3.2.2.2	Porosities and ligand density	59
3.2.2.3	Exclusion factor	60
3.2.2.4	Axial dispersion coefficient	61
3.2.3	Linear gradient elution experiments.....	62
3.2.3.1	Salt gradient elution of mAb04 charge variants	62
3.2.3.2	pH gradient elution of mAb04 charge variants.....	63
3.2.3.3	Stoichiometric displacement model	63
3.2.3.4	Ligand density model based on a stoichiometric displacement	67
3.2.3.5	<i>In silico</i> validation – Chromatogram simulation of CEX resins.....	73
4	DISCUSSION	79
4.1	Modeling of anion exchange resins	79

4.1.1	Linear salt gradient elution experiments	79
4.1.1.1	Ligand density dependency in the stoichiometric displacement model.....	80
4.1.1.2	Ligand density dependency of the characteristic charge	81
4.1.1.3	Ligand density dependency of $\Delta Gi0/RT$ and $\Delta Gs0/RT$	84
4.1.1.4	<i>In silico</i> validation – Chromatogram simulation of AEX resins.....	87
4.1.1.5	Ligand density dependency of the characteristic charge (<i>vi</i>) – a Donnan equilibrium in ion exchange chromatography.....	88
4.2	Modeling of cation exchange resins	91
4.2.1	CEX column parameters.....	91
4.2.2	Linear gradient elution experiments.....	95
4.2.2.1	Stoichiometric displacement model	97
4.2.2.2	Ligand density model based on a Stoichiometric displacement model.....	98
4.2.2.3	<i>In silico</i> validation – Chromatogram simulation of CEX resins.....	101
5	CONCLUSIONS	103
6	ABSTRACT	105
7	REFERENCES	107
8	APPENDIX	117
9	CURRICULUM VITAE	118

10 ACKNOWLEDGMENT..... 120

LIST OF ABBREVIATIONS

ADCC	Antibody-dependent cellular cytotoxicity
ADCs	Antibody-drug conjugates
AEX	Anion-exchange chromatography
AEX-MMC	Multimodal chromatography with hydrophobic and positively charge groups
Bis-Tris	Bis(2-hydroxyethyl)amino-tris(hydroxymethyl)methane
BSA	Bovine serum albumin
CAPS	3-(Cyclohexylamino)-1-propanesulfonic acid
CEX	Cation-exchange chromatography
CHES	2-(Cyclohexylamino)ethanesulfonic acid
CIP	Cleaning in place
CV	column volume
CV (s)	Column volume (s)
DIX	Donnan ion-exchange model
EMG	exponentially modified gauss function
EPO	erythropoietin
FDA	Food and Drug Administration
FPLC	Fast protein liquid chromatography
HEPES	2-[4-(2-hydroxyethyl)piperazin-1-yl]ethanesulfonic acid
HIC	Hydrophobic interaction chromatography

HIV	Human immunodeficiency virus
HMW	High molecular weight species
HPLC	High-performance liquid chromatography
IEC	Ion exchange chromatography
kDa	Kilodalton
LGE	Linear gradient elution experiments
mAb	Monoclonal antibody
MES	2-(N-morpholino)ethanesulfonic acid
MMC	mix-mode chromatography
MOPS	2-(N-morpholino)ethanesulfonic acid
MOPSO	3-morpholino-2-hydroxy-propanesulfonic acid
MWCO	molecular weight cut-off
NaCl	Sodium chloride
NaH ₂ PO ₄ ·H ₂ O	Sodium dihydrogen phosphate monohydrate
NaN ₃	Sodium azide
NaOH	Sodium hydroxide
NMR	Nuclear magnetic resonance
PDE	Partial differential equation
pI	Isoelectric point
PTM	Post-translational modification
RI	Refractive index detector

SAXS	small-angle X-ray scattering
SD	Stoichiometric displacement model
SEC	Size exclusion chromatography
SO ₃ ⁻	Sulfoisobutyl
TAPS	N-tris(hydroxymethyl)methyl-3-aminopropanesulfonic acid
TFF	Tangential flow filtration
TMAE	Trimethylammoniummethyl
Tris	Tris(hydroxymethyl)aminomethane
UV	ultraviolet

LIST OF SYMBOLS

$A_{1/2}$	molecular interaction parameters between the present species in a binary mixture
$A_{2/1}$	molecular interaction parameters between the present species in a binary mixture
A	specific surface area
A_i	distribution coefficient / initial slope of the adsorption isotherm
$A_{i,\Delta}$	initial slope of the adsorption isotherm for the ligand density SD model
A_{IEC}	distribution coefficient in ion exchange
c	molar concentration of pure water
$c_{Cl^-}^B$	chloride concentration on the liquid phase
CF	compression factor
\bar{c}_n	concentration of a species in the adsorbate phase
c_n	concentration of a species in solution
$\frac{\bar{c}_P}{c_P}$	protein distribution ratio in a chromatographic resin
\bar{c}_P	concentration of the protein in the adsorbate
$c_{pH, final}$	final pH value in gradient
$c_{pH, initial}$	initial pH value in gradient
$c_{Cl^-}^R$	chloride concentration on the resin phase
\bar{c}_S	concentration of the counter-ion in the adsorbate phase

c_s	concentration of the counter-ion in solution
$c_{salt, final}$	initial salt concentration in the gradient
$c_{salt, initial}$	final salt concentration in the gradient
$\Delta\hat{G}_i^0$	practical Gibbs energy change of association of the protein
$\Delta\hat{G}_s^0$	practical Gibbs energy change of association of the counter-ion
ΔG_p^0	Gibbs energy change of association of the protein
ΔG_s^0	Gibbs energy change of association of the counter-ion
D_{ax}	axial dispersion coefficient
d_p	particle diameter
g^E	molar excess Gibbs energy
GH_{pH}	normalized gradient slope of the linear pH gradient
GH_{salt}	normalized gradient slope of the linear salt gradient
\bar{g}_i^E	partial molar excess Gibbs energy
g_{pH}	slope of the linear pH gradient
g_{salt}	slope of the linear salt gradient
$k_{d,i}$	exclusion factor of a protein
\tilde{K}_E	thermodynamic equilibrium constant including the asymmetric reference potentials
K_E	thermodynamic equilibrium constant
k_{eff}	effective mass-transfer coefficient
L_c	column length

N_1	number of amino acids involved on the protein-ligand binding
N_2	number of amino acids involved on the protein-ligand binding influenced by the ionic capacity
N_{+i}	number of basic amino acids
N_{-i}	number of acidic amino acids
$n_{j \neq i}$	number of moles of all components are kept constant except for i
\bar{n}_n	number of moles of a species in the adsorbate phase
n_n	number of moles of a species in solution
$n_{T, \Delta_{ref}}$	total number of moles of a bound species at the reference ligand density
$n_{T, \Delta}$	total number of moles of a bound species at a determined ligand density
P	pressure
pH_B	pH value in the liquid phase
pH_R	pH value in the resin phase
$pK a_i$	dissociation constant of a ionizable group
q_{eq}^*	hypothetical loading when both phases are in equilibrium
q_i^*	overall concentration in the accessible pore volume
R	Gas constant
r_D	ratio of the ion concentrations in between the adsorbate and the liquid phase
SF	swelling factor
S_{Cl^-, OH^-}	selectivity constant for the anions

S_{Na^+,H^+}	selectivity constant for the cations
T	temperature
t	time
u_{init}	interstitial mobile phase velocity
V_c	total column volume
V_{dex}	retention volume of a dextran pulse
V_g	gradient volume
V_{salt}	retention volume of a salt pulse
V_{system}	system dead volume
\bar{x}_n	mole fraction of a generic nth species in the adsorbate state
x_n	mole fraction of a generic nth species in solution
z_p	charge number of the protein
z_s	charge number of the counter-ion

GREEK LETTERS

a_i	Activity of the protein in solution
a_s	Activity of the counter-ion in solution
\bar{a}_i	Activity of the protein in the adsorbate state
\bar{a}_s	Activity of the counter-ion in the adsorbate state
$\overline{\alpha_{PS}}$	activity of the exchangeable ion with the protein
γ_i	activity coefficient of the protein in solution
γ_s	activity coefficient of the counter-ion in solution
$\bar{\gamma}_i$	activity coefficient of the protein in the adsorbate state
$\bar{\gamma}_i^\infty$	activity coefficient of the protein at infinite dilution
$\bar{\gamma}_s$	activity coefficient of the counter-ion in the adsorbate state
Γ	surface density
ε_{280}	extinction coefficient at 280 nm
ε	interstitial porosity
ε_p	intraparticle porosity
ε_t	total porosity
Λ	Ionic capacity / ligand density
$\Lambda_{settled}$	ionic capacity of the gravity settled resin
Λ_{packed}	ligand density of the packed bed
$\bar{\mu}_i^0$	standard state chemical potential of the protein in the adsorbate state
μ_s^0	standard state chemical potential of the counter-ion in solution

μ_i^0	standard state chemical potential of the protein in solution
$\bar{\mu}_s^0$	standard state chemical potential of the counter-ion in the adsorbate state
μ_{mom}	first central peak moment
ν_i	Characteristic charge
ν_0	Characteristic charge coefficient
σ_{mom}	second central peak moment
$\sum c_i$	sum of all species present in solution
$\sum \bar{c}_i$	sum of all species present in the adsorbate state

1 INTRODUCTION

1.1 Biopharmaceuticals - monoclonal antibodies

Biopharmaceuticals are defined by the U.S. Food and Drug administration (FDA) as recombinant proteins produced by means of biotechnological approaches. This term constitute a wide group of drugs such as hormones, monoclonal antibodies (mAbs), growth factors, vaccines, blood factors, nucleic acid-based drugs, among others (van Beers & Bardor, 2012). And these biologics can target more than hundreds of diseases, such as heart disease, multiple sclerosis, breast cancer, diabetes, cystic fibrosis, HIV, migraine, and many more (Marichal-Gallardo & Álvarez, 2012). Compared to small molecules, biopharmaceutical drugs are a class that offers the advantages of high specificity and potency. But the high structural complexity of proteins and an elaborated production process can create modifications on the intended product that may induce immune responses (Giezen, Mantel-Teeuwisse, & Leufkens, 2009). The data generated throughout the past 40 years of the biopharmaceuticals been in the market have shown that many factors can affect the immunogenicity of a protein (e.g., structural properties, storage conditions, impurities, dose and length of treatment, route of administration, among others) (Schellekens, 2005). The various factors that can influence the immunogenicity of the therapeutic drug can be roughly classified as product related, patient related and treatment related factors, for the purpose of this study, the product related factors will be explored.

Due to the complexity of the recombinant proteins, the majority of protein-based biopharmaceuticals approved or in clinical trials at the moment have a number of micro heterogeneities introduced through post-translational modifications (PTM) (Beck & Liu, 2019). Some of the most common PTMs associated with proteins are amidation, γ -carboxylation, β -hydroxylation, disulfide bond formation, glycosylation, phosphorylation, sulfation, and are known to alter the biopharmaceutical characteristics, such as product stability and biological activity (Walsh & Jefferis, 2006). Glycosylation represents the most widespread PTM in biopharmaceutical products and may impact the glycoprotein folding, stability, trafficking and immunogenicity as well as its clinical efficacy (Walsh, 2010). For instance, it has been reported that the deglycosylated Cetuximab has no *in vitro* affinity to the Fc γ RI and Fc γ RIIIa receptors and its antibody-dependent cellular cytotoxicity (ADCC) activity is

lost on this version of the protein (Váradi, Jakes, & Bones, 2020). While the removal of N-glycosylation sites on erythropoietin (EPO) reduces the in vivo activity (Delorme et al., 1992). Even further, a recent study demonstrated that the C-terminal lysine clipping is essential for antibodies to achieve their maximal complement-activating capability, effect that for years was neglected by other study groups; which stated that the C-terminal lysines did not affect the antibody function (van den Bremer et al., 2015). In general, these small modifications can alter the overall surface-charge distribution of the therapeutic protein either by changing the number of charged groups or indirectly by altering the structural composition of the protein (Khawli et al., 2010). And several studies had demonstrated how these charge variants affect the in vitro and in vivo properties of antibodies, for instance, an increase of 0.5 pI units on an antibody leads to a noticeable difference in pharmacokinetics and the shift of approximately one isoelectric point affects the tissue distribution of mAbs (Boswell et al., 2010; Khawli et al., 2010; Zhao et al., 2016). Therefore, the monitor, control and characterization of antibody variants are of great importance to the biotechnology industry.

Biotech manufacturers are required to demonstrate product consistency and assure the quality and stability of the therapeutic products. Issue that nowadays is even more critical, since blockbuster biopharmaceuticals are running out of patent protection and therefore a growing interest in biosimilars is emerging. Biosimilars are defined as: “copy versions of an already authorized biological medicinal product” and had to demonstrate the similarity in molecular and biological terms to the reference medicinal product (Barbier et al., 2020; Y. J. Zhang & An, 2017). Since biopharmaceuticals are produced in living organisms they cannot be fully copied. Meaning that any change in cell host, growth conditions, purification process, formulation or storage conditions will lead to different structural changes in the protein (Beck et al., 2013). Making imperative a thorough study of the biosimilar and the reference product to ensure efficacy and safety of the new drug. Achieving this is not a simple task, it is necessary the use of new and innovative approaches to detect small product-related differences and separate them from the main product. All of these facts underline the importance of the biopharmaceuticals and why are considered to be one of the most challenging molecules to produce, formulate and deliver.

1.2 Purification of therapeutic drugs - chromatography

A typical production process for biopharmaceuticals can be divided in four general segments: media preparation, fermentation (upstream), purification (downstream) and formulation (Strube, Grote, Josch, & Ditz, 2011). The downstream processing of a biologic has the main goal of isolate and purify the target component to reach a final product quality. To achieve this, many different unit operations can be used, such as centrifugation, ultrafiltration, chromatography, membrane chromatography, etc. In this work, the focus will be in chromatography, since is the dominant technique for the purification of biologicals, as well as for the analysis of proteins (Hanke & Ottens, 2014). This predominance is mainly attributed to the high-resolution purification that can be achieved even for analogous components. Chromatography uses the different characteristics of the analyte to purify it, for instance, separation in size exclusion chromatography (SEC) is based on differences in the molecular size; ion exchange chromatography (IEC) exploits differences in charge; hydrophobic interaction chromatography (HIC) separates base on surface hydrophobicity; and mix-mode chromatography (MMC) exploits the combination of some of the ligands mentioned above (Rathore, Kumar, & Kateja, 2018).

More specifically, ion exchange chromatography has become a key component in the downstream process (Klutters, Wittkopp, Jöhnck, & Frech, 2016). IEC is a powerful and ubiquitous unit operation in the purification of therapeutic proteins (S. Yamamoto, Nakanishi, Matsuno, & Kamikubo, 1983). Ion exchange processes are basically chemical reactions between ions in solution and ions in an insoluble stationary phase. Here, certain ions are removed by the ion-exchange solid, and since electroneutrality must be maintained, the solid releases replacement ions to the solution (Mollerup, 2008). This technique is often used as a polishing step on the purification train of biopharmaceuticals because it provides effective removal of product-related impurities and contaminants. Protein purification processes generally rely on anion exchange resins (AEX) for the removal of endotoxins, viruses, host-cell proteins (HCPs) and DNA, whereas the cation exchange resins (CEX) are used for the separation of charge variants, aggregates, low molecular weight degradation products or HCPs (Marichal-Gallardo & Álvarez, 2012). The popularity of IEC comes from the ability to promptly scale up the process from a laboratory level to an industrial scale, as well as the achievement of high-purity products (Schmidt-Traub, Schulte, & Seidel-Morgenstern, 2012).

But as mentioned before, the purification of biopharmaceuticals is not a simple task. Novel molecular formats display a pattern of similar product-related impurities and have become a real challenge to obtain a reliable separation method. These new modalities have not only the intrinsic heterogeneity of the host mAb (e.g., glycosylation, aggregation, etc.) but are also very susceptible to production process modifications and storage conditions, leading to a complex purification process. New high-resolution methods can be applied, but this comes with their limitations such as high sensitivity (i.e., small variations will lead to different attributes in the final product). Therefore, to ensure the quality and consistency of a product, the variability of process parameters and raw material attributes in the downstream process must be investigated and understood.

1.3 Ligand density variation in IEC

The performance of an ion-exchange process depends on a complex interrelationship between several parameters, such as protein properties, mobile phase conditions, and chromatographic resin characteristics (Hardin, Harinarayan, Malmquist, Axen, & van Reis, 2009). Consequently, the understanding of the influence of stationary phase properties (e.g., particle size, pore size, ligand density, etc.) on the purification process has gained attention. Special focus has been placed on the batch variations of IEC resins since it has been proven that it can play a significant role in the robustness of the downstream process (Deitcher, Rome, Gildea, O'Connell, & Fernandez, 2010; Shuichi Yamamoto, Watler, Feng, & Kaltenbrunner, 1999). Ligand density is known to be one of the main lot-to-lot variations, affecting protein adsorption and separation performance (Aono, Iliescu, Cecchini, Wood, & McCue, 2013; D. Wu & Walters, 1992; Shuichi Yamamoto et al., 1999).

The variations of ionic capacities in the stationary phase material and their effect in the elution behavior of proteins has been studied throughout the years. Wu and Walters (D. Wu & Walters, 1992) observed a change in the retention of Lysozyme and cytochrome c when the ligand density of the silica resin was increased, and a characteristic band-broadening when a low ligand density was used. Langford et al. (Langford, Xu, Yao, Maloney, & Lenhoff, 2007) investigated the transport behavior of lysozyme, cytochrome c and ribonuclease A in cation exchange chromatography with varying ligand densities. Studies directed to monoclonal antibodies showed an increase in the static (Wrzosek, Gramblicka, & Polakovic, 2009) and dynamic (Hardin

et al., 2009) binding capacity (SBC and DBC, respectively) with an increase in resin ligand density until a threshold is reached and an improvement in absorption is not possible anymore. The same observation was reported by Franke et al. (Franke et al., 2010) showing that an optimal ligand density can be achieved for a specific purification process, but a compromise between higher ligand densities to enhance equilibrium capacity or lower ligand densities to obtain higher mass transfer rates must be made. Subsequent studies focusing on process performance showed no effect of the ligand density variation on yield, HCP clearance or aggregates removal (Fogle, Mohan, Cheung, & Persson, 2012; Fogle & Persson, 2012). Although it is important to mention that this observation is valid for the specific protein purification presented and it cannot be generalized to other processes. Another important aspect of the variability of ligand density on tentacular ion exchange resins is the transport behavior of proteins. Several authors have shown a correlation of structural effects and transport rates (e.g., pore accessibility, pore diffusion, etc.) with the variation of resin ligand density (Bhambure et al., 2017; Bhambure, Gillespie, Phillips, Graalfs, & Lenhoff, 2016; Franke et al., 2010; Thomas et al., 2013). And although evidently, there exists a complicated relationship between the resin properties and resin performance, the mechanistic understanding of it is still limited. To address this drawback, the use of a model-based approach can be an effective tool for comprehending the impact of parameter variations (e.g., ligand density) and their influence on the process. This modeling and simulation approach can be used for faster development of new chromatographic separations, optimization of existing processes, process validation and scale-up (Ishihara, Kadoya, & Yamamoto, 2007; Kaltenbrunner, Giaverini, Woehle, & Asenjo, 2007).

1.4 Aim of this work

The objective of this work was to apply mechanistic modeling to gain a deeper understanding of the influence of ligand density variations on the performance of ion exchange chromatography on the purification of biopharmaceuticals. First, two kinds of proteins, BSA and a monoclonal antibody (mAb03) with different isoelectric points and molecular weight, were chosen as model proteins to evaluate the influence of ligand density variation on the retention behavior on anion exchange resins. Additionally, a remarkable monoclonal antibody (mAb04) was used because of its high portion of charge variants on cation exchange chromatography.

To achieve this, the well-known and established stoichiometric model (SD model) according to Kopaciewicz et al. was introduced (Kopaciewicz, Rounds, Fausnaugh, & Regnier, 1983). The investigation in AEX resins is accomplished by the use of 13 prototype resins having the same support as the strong anion exchange resin Fractogel[®] EMD TMAE (M), but differing ligand densities. While the investigation in CEX resins is performed by the use of 5 prototype resins having the same support as the strong cation exchange resin Fractogel[®] EMD SO₃⁻ (M), but differing ligand densities. Furthermore, the impact of modulators such as pH and counter-ion concentrations is also accounted for and will be correlated to the elution data from the model proteins in the linear salt and pH gradient elution (LGE) experiments. The observations on the elution behavior of the model proteins when the ligand density varies should give a good approximation to describe this influence in the IEC adsorption equilibrium.

Moreover, the obtained model parameters, in addition to the lumped rate model, will be used to perform *in silico* chromatograms in linear dual gradients of salt and pH, which can prove the reliability of the model. The use of this mathematical modeling and simulation methodology allows the increase in the theoretical understanding of the separation process of proteins and can help to obtain a faster development of new chromatographic separations, optimization of existing processes, process validation or scaling-up. Therefore, the results presented in this work will have a significant impact not only in the area of modeling and simulation of chromatography but, more importantly, on the process development in the biopharmaceutical industry. Because to ensure quality and consistency in a product, the variability of process parameters and raw material attributes must be addressed.

2 MATERIALS AND METHODS

2.1 Electronic equipment

The electronic equipment used in this work is listed in **Table 1**.

Table 1: Electronic equipment used in this research project.

Instrument	Technique	Manufacturer
ÄKTA™ Purifier 10	FPLC	GE Healthcare
ÄKTA™ Explorer 100	FPLC	GE Healthcare
ÄKTA™ Crossflow	TFF	GE Healthcare
ÄKTA™ Micro	HPLC	GE Healthcare
Hanna Edge HI2020-02	pH meter	Hanna Instruments
inoLab™ Multi 9420 IDS™	pH and conductivity meter	WTW
Agilent 8453	Spectrophotometer	Agilent
Smartline RI Detector 2300	RI detector	Knauer
Milli-Q® Gradient	Water purification system	EMD Millipore
Sonorex™ Super 10P	Ultrasonic bath	Bandelin Electronic
Sartorius Research R200D	Analytical balance	Sartorius

2.2 Computer programs

The software used to analyze the data produced in this work are listed in **Table 2**.

Table 2: Software used in this research project.

Software	Technique	Manufacturer
Berkley Madonna™ Version 8.3.23	Differential equation	R. Macey and G. Oster, University of California

Software	Technique	Manufacturer
Peakfit® v.4.12	Peak convolution	SeaSolve software
Unicorn™ 5.31	ÄKTA system control system	GE Healthcare
Buffer Maker	Buffer calculator	BPP Marcel Borowski
TableCurve 3D v4.0	3D surface fitting	Systat software, Inc.
TableCurve 2D v5.01	2D surface fitting	Systat software, Inc.
MATLAB R2019a	Numerical computing	MathWorks

2.3 Chemicals

The following chemicals (e.g., to produce buffers used in the chromatographic experiments) were used:

Table 3: Chemicals used in this research project.

Chemical	Grade/Purity	Manufacturer
1,2 Diaminopropane	≥98%	Merck
1,3 Diaminopropane	≥99%	Merck
Acetic acid, 100%	≥99%	Applichem
Bis-Tris	≥99%	Sigma-Aldrich
Blue Dextran		Sigma-Aldrich
CAPS	≥99%	Applichem
CHES	≥99%	Applichem
Citric acid	≥99%	Applichem
Dextran (MW ~ 2,000,000 g/mol)		Sigma-Aldrich

Chemical	Grade/Purity	Manufacturer
Ethanol	≥96%	Berkel
HEPES	≥99.5%	Applichem
Hydrochloric acid (HCl), 0.1 mol/L	Ph.Eur.	Merck
Hydrochloric acid (HCl), 37%	24 – 25 %	Applichem
MES monohydrate	≥99%	Applichem
MOPS	≥99.5%	Applichem
MOPSO	≥99%	Applichem
Pyridine	≥99%	Applichem
Sodium azide (NaN ₃)	≥99%	Applichem
Sodium chloride (NaCl)	p.A.	Applichem
Sodium dihydrogen phosphate monohydrate (NaH ₂ PO ₄ ·H ₂ O)	Ph.Eur.	Merck
Sodium hydroxide (NaOH)	p.A.	Applichem
TAPS	≥99%	Applichem
Tris	≥99%	Applichem

2.4 Chromatography resins

2.4.1 Preparative anion exchange resins

Thirteen strong anion exchange resin prototypes with a cross-linked polymethacrylate support and trimethylammonium ethyl groups as ligands were provided by Merck KGaA (Darmstadt, Germany). These prototypes are based on the same support used for Fractogel[®] EMD TMAE (M) and were synthesized with different ligand densities. All resins were packed in OPUS[®] MiniChrom columns by Repligen (Weingarten, Germany) with an inner diameter of 8 mm and a length of 50 mm ($V_c = 2.5$ mL).

Table 4 shows the anion exchange columns used for the modeling and simulation in this work. The ionic capacity values needed for this investigation must refer to the ligand density in the pore volume therefore this calculation will be explained in section 3.1.1.

Table 4: Ligand density of the anion exchange resins used in this research project.

Resin ID	LOT	$\Lambda_{\text{Dry gel}} (\mu\text{eq}\cdot\text{g}^{-1})$	$\Lambda_{\text{packed}} (\mu\text{eq}\cdot\text{mL}^{-1})$
Prototype resin 1	K22635181	203.6	47.91
Prototype resin 2	K92904881	243.6	57.32
Prototype resin 3	K32861081	263.1	61.91
Prototype resin 4	K32872381	290.0	68.24
Prototype resin 5	K93133985	306.0	72.00
Prototype resin 6	K91208381	315.1	74.14
Prototype resin 7	K92905285	336.0	79.06
Prototype resin 8	K93052085	346.0	81.41
Prototype resin 9	K33692716	356.6	83.91
Prototype resin 10	K33692816	432.0	101.65
Prototype resin 11	K33796416	534.0	125.65
Prototype resin 12	K31678016	662.0	155.76
Prototype resin 13	K32215716	799.6	188.14

2.4.2 Preparative cation exchange resins

Five strong cation exchange resin prototypes with a cross-linked polymethacrylate support and sulfoisobutyl groups as ligands were provided by Merck KGaA (Darmstadt, Germany). These prototypes are based on the same support used for Fractogel[®] EMD SO₃⁻ (M) and were synthesized with different ligand densities. All resins were packed in OPUS[®] MiniChrom columns by Repligen (Weingarten, Germany) with an inner

diameter of 8 mm and a length of 50 mm ($V_c = 2.5$ mL). **Table 5** shows the cation exchange columns used for the modeling and simulation in this work. Once again, the ionic capacity values needed for this investigation must refer to the ligand density in the pore volume (see section 3.2.2.2).

Table 5: Ligand density of the cation exchange resins used in this research project.

Resin ID	LOT	$\Lambda_{\text{Dry gel}} (\mu\text{eq}\cdot\text{g}^{-1})$	$\Lambda_{\text{packed}} (\mu\text{eq}\cdot\text{mL}^{-1})$
Prototype resin 1	12Pt1022-01	395	82.94
Prototype resin 2	K93137182	439	103.29
Prototype resin 3	K93554082	483	113.65
Prototype resin 4	K93557682	548	128.94
Prototype resin 5	12Re007-01	645	151.76

2.4.3 HPLC resins

The analyses of the samples following the methodology in sections 2.8 and 2.9 were performed on the HPLC columns shown in **Table 6**.

Table 6: HPLC columns used in this work.

Name	Type	Dimensions	Manufacturer
BioPro SP-F	CEX	4.6 x 50 mm	YMC Europe GmbH
BioSep s3000	SEC	7.8 x 300 mm	Phenomenex

2.5 Proteins and sample preparation

The monoclonal antibody (mAb03) used in this work (**Table 7**) was provided by the manufacturer as a post-protein A purification sample, no further polishing step was needed. While the BSA sample had to be polished with anion exchange chromatography to remove high molecular weight impurities. For the monoclonal antibody mAb04, a cation exchange chromatography was performed to obtain individual samples of the charge variants (as described in section 2.5.3). Prior to the

modeling runs, all purified proteins were concentrated and conditioned into the respective equilibration buffer by ultra- and diafiltration unless indicated otherwise (refer to section 2.5.2).

Table 7: Proteins used in this work.

Protein	pI	ϵ_{280} (mL·mg ⁻¹ ·cm ⁻¹)	Manufacturer
mAb03	8.20 – 8.60 ^{a)}	1.34	Merck KGaA
mAb04	8.15 – 8.40 ^{b)}	1.41	Boehringer Ingelheim
BSA	4.8 ^{c)}	0.667	Applichem

^{a)} As reported in Kullasakboonsri Bachelor's thesis (Kullasakboonsri, 2016).

^{b)} Determined isoelectric points based on the results of the isoelectric focusing (see **Appendix**).

^{c)} As reported in literature (Whitley, Wachter, Liu, & Wang, 1989).

2.5.1 Purification of BSA

The removal of high molecular weight impurities in the BSA sample was achieved with a strong anion exchange resin. A pre-packed column with Fractogel[®] EMD TMAE (M) resin in an OPUS[®] MiniChrom column (Repligen, Weingarten, Germany) with an inner diameter of 8 mm and a length of 20 cm ($V_c = 10$ mL) was used.

The purification was conducted using 1,2-diaminopropane buffers (30 mol/L, pH 7.0) with 0.05 - 1.0 mol/L NaCl as the mobile phase. The sample was diluted to obtain a concentration of 0.5 mg/mL. To process the entire amount of BSA required to perform the modeling experiments, several runs of AEX chromatography were needed. Prior to each chromatography experiment, the column was equilibrated with 5 CVs of the mobile phase at 1 mL/min. The sample was injected with the same flow rate, and the elution was carried out with a linear gradient elution of 40 CV. The elution step was fractionated and only the first peak was collected and conditioned for further experiments.

2.5.2 Buffer exchange of mAb03 and BSA

Prior to the modeling runs, the purified proteins (BSA and mAb03) were concentrated and conditioned into the respective equilibration buffer by ultra- and diafiltration using a Kwick™ Start cassette with a membrane area of 50 cm³ and a molecular weight cut-off (MWCO) of 30 kDa (GE Healthcare, Uppsala, Sweden) in an ÄKTAcrossflow™ system. The concentrated protein solutions were diafiltrated against a maximum of 8 diavolumes of the respective equilibration buffer until the conductivity reached a constant value. The transmembrane pressure was set to 2.39 bar and the maximum operating pressure to 4 bar.

2.5.3 Purification of mAb04 charge variants

The high portion of charge variants in the mAb04 sample (see section 3.2.1.1), makes this protein remarkable. To study this unique characteristic, the separation of the charge variants was crucial, so the influence of each one of them can be investigated separately in the modeling runs.

To isolate the mAb04 charge variants, an Eshmuno® CPX strong cation exchange resin was used. The stationary phase was packed with a compression factor of 17% in a Superperformance® column by Merck (Darmstadt, Germany) and an inner diameter of 10 mm and length of 20 cm ($V_c = 15.71$ mL). The buffers shown in **Table 8** were applied to achieve the desired elution steps.

Table 8: Buffers for the purification of mAb04 charge variants.

Substance	Binding buffer concentration (mmol·L⁻¹)	Elution buffer concentration (mmol·L⁻¹)
MES	10.0	10.0
MOPSO	6.0	6.0
HEPES	4.0	4.0
TAPS	8.0	8.0
CHES	8.0	8.0
CAPS	11.0	11.0

Substance	Binding buffer concentration (mmol·L⁻¹)	Elution buffer concentration (mmol·L⁻¹)
Acetic acid	12.0	12.0
NaOH	10.0	53.0
NaCl	44.0	0.0
pH	5.00	10.50

All buffers were vacuum filtered through a 0.45 µm cellulose nitrate filter (Sartorius, Gottingen, Germany) and degassed for 20 minutes in an ultrasonic bath at room temperature.

To achieve the required amount of mAb04 charge variants needed to perform the modeling experiments, several runs of CEX chromatography were performed. Prior to each chromatography experiment, the column was equilibrated with 5 CVs of the mobile phase with a volumetric flow rate of 1.56 mL/min (i.e., a linear flow rate of 119 cm/h). A volume of 15.7 mL of the sample (load: 14 mg/mL packed resin) was injected with the same flow rate.

The elution was performed with four pH steps by mixing both equilibration buffer and elution buffer on the ÄKTA system™ at different buffer ratios. The first step was performed at 75% elution buffer to equilibration buffer ratio in 3.2 CV, the second step was 85% in 2.0 CV, the third step was 90% in 3.0 CV and the final step was 100% in 2.0 CV. The elution peaks were fractionated in fractions of 3 mL and later analyzed with the CEX-HPLC method described in section 2.9. According to the analytic results, the fractions were pooled to obtain the three main mAb04 charge variants.

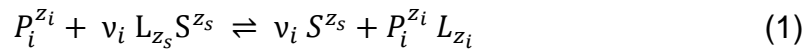
2.6 Mechanistic modeling of chromatographic separation processes

The theoretical foundations of the modeling of chromatographic separation processes are summarized in the following chapters. First, a model (stoichiometric displacement model – SD model) capable to describe the adsorption isotherm of a protein in ion exchange chromatography is described. Then, a couple of assumptions on the SD model were reconsidered, leading to the introduction of an extended model that

account for the ligand density variation of the resin. Finally, the mathematical description of the column, using a partial differential equation (PDE) is shown.

2.6.1 Ion exchange equilibrium model

The adsorption of a protein P with the ligands L on an ion exchange resin can be described by the stoichiometric displacement model (SD). A displacement of counter-ions S takes place when the protein associates with a number of immobilized ligands v_i on the stationary phase. Assuming that the ligand L has a unit charge, the equilibrium scheme of a component i , on this exchange can be described as (Mollerup, Hansen, Frederiksen, & Staby, 2010):



where z_s is the charge number of the counter-ion, z_i is the binding charge number of the protein, and $v_i = z_i/z_s$ is the stoichiometric coefficient or characteristic charge. The thermodynamic equilibrium constant K_E for a single component can be defined using the activities a of the participating species as (Mollerup et al., 2010):

$$K_E = \frac{a_s^{v_i} \bar{a}_i}{\bar{a}_s^{v_i} a_i} \quad (2)$$

where the subscript S, and i , describe the activities of the counter-ion and the protein, respectively. Whereas the overbar represents the species in the adsorbate state, and the lack of it denotes the species in solution.

According to Gerstner et al. (Gerstner, Bell, & Cramer, 1994) the equilibrium constant K_E can be calculated from the change in the standard Gibbs energy of exchange as follows:

$$-RT \ln K_E = \bar{\mu}_i^0 + v_i \cdot \mu_s^0 - \mu_i^0 - v_i \cdot \bar{\mu}_s^0 = \Delta G_i^0 - v_i \cdot \Delta G_s^0 \quad (3)$$

Here $\bar{\mu}_i^0$ and μ_i^0 are the reference state chemical potentials of the adsorbate and solute component, respectively. While $\bar{\mu}_s^0$ and μ_s^0 are the standard state chemical potential of the adsorbate and solute counter-ions. With the universal gas constant, R, the absolute temperature, T, the Gibbs energy change of association of the protein, ΔG_i^0 , which is specific to the protein-adsorbent pair, and ΔG_s^0 as the Gibbs energy change of

association of the counter-ion, which is also specific to the salt-adsorbent pair (Mollerup, 2008).

The practical equilibrium constant is defined as:

$$\hat{K}_E = K_E \frac{\bar{\gamma}_s^{v_i} \cdot \gamma_i}{\gamma_s^{v_i} \cdot \bar{\gamma}_i} \quad (4)$$

where the activity coefficients of the counter-ion are represented as γ_s and $\bar{\gamma}_s$, while the protein activity coefficients are γ_i and $\bar{\gamma}_i$ in the liquid and solid phases, respectively. With this definition, the practical thermodynamic equilibrium constants can be expressed as follows (Mollerup et al., 2010):

$$-RT \ln \hat{K}_E = (\Delta G_i^0 - RT \ln(\gamma_i/\bar{\gamma}_i)) - v_i \cdot (\Delta G_s^0 - RT \ln(\gamma_s/\bar{\gamma}_s)) = \Delta \hat{G}_i^0 - v_i \cdot \Delta \hat{G}_s^0 \quad (5)$$

where $\Delta \hat{G}_i^0$ and $\Delta \hat{G}_s^0$ are the practical Gibbs energy change of association of the protein and the counter-ion, respectively.

The initial slope of the adsorption isotherm is equal to the thermodynamic retention factor A_i , at very low loadings and can be expressed as (Gerstner et al., 1994):

$$A_i \equiv \lim_{c_p \rightarrow 0} \left(\frac{\bar{c}_i}{c_i} \right) = \hat{K}_E \cdot \left(\frac{\Lambda}{c_s} \right)^{v_i} \quad (6)$$

where the protein concentration on the bound state is \bar{c}_i , the protein concentration in the mobile phase is c_i , the ligand density of the stationary phase in the pore volume is represented as Λ , and c_s is the concentration of the counter-ion free in solution.

2.6.2 Ligand density dependency on the stoichiometric displacement model

To derivate an equation that takes into account the ligand density variation of ion exchange resins, the following steps were followed. First, the thermodynamic equilibrium constant for the exchange scheme in Eq. (1) is described as:

$$K_E = \frac{a_s^{v_i} \cdot \bar{a}_i}{\bar{a}_s^{v_i} \cdot a_i} = \frac{(x_s \cdot \gamma_s)^{v_i} \cdot (\bar{x}_i \cdot \bar{\gamma}_i)}{(x_i \cdot \gamma_i) \cdot (\bar{x}_s \cdot \bar{\gamma}_s)^{v_i}} \quad (7)$$

where the subscript S, and i , describe the activities of the counter-ion and the protein, respectively. Whereas the overbar represents the species in the adsorbate state, and the lack of it denotes the species in solution. The mole fraction and the activity coefficient of the counter-ion are represented as x_s and γ_s , while the protein mole

fraction and activity coefficient are x_i and γ_i . The number of binding sites that the protein interacts with upon association is denoted as ν_i and is defined as characteristic charge.

Subsequently, the definition of mole fraction for a generic n^{th} species in the solid \bar{x}_n and the mobile phase x_n is introduced:

$$\bar{x}_n = \frac{\bar{c}_n}{\sum_{m=1}^P \bar{c}_m} \quad (8)$$

$$x_n = \frac{c_n}{\sum_{m=1}^P c_m} \quad (9)$$

where \bar{c}_n represents the concentration of a species in the adsorbate phase, and c_n represents the concentration of a species in the mobile phase. Whereas, $\sum \bar{c}_m$ and $\sum c_m$ represent the sum of all species in the adsorbate and mobile phase, respectively.

Expressing Eq. (7) in terms of the concentrations in the solid and the mobile phase gives:

$$K_E = \frac{\left(\frac{c_s}{\sum c_m} \cdot \gamma_s\right)^{\nu_i} \cdot \left(\frac{\bar{c}_i}{\sum \bar{c}_m} \cdot \bar{\gamma}_i\right)}{\left(\frac{c_i}{\sum c_m} \cdot \gamma_i\right) \cdot \left(\frac{\bar{c}_s}{\sum \bar{c}_m} \cdot \bar{\gamma}_s\right)^{\nu_i}} = \left(\frac{\bar{c}_i}{c_i} \cdot \frac{\sum c_m}{\sum \bar{c}_m} \cdot \frac{\bar{\gamma}_i}{\gamma_i}\right) \cdot \left(\frac{c_s}{\bar{c}_s} \cdot \frac{\sum \bar{c}_m}{\sum c_m} \cdot \frac{\gamma_s}{\bar{\gamma}_s}\right)^{\nu_i} \quad (10)$$

The practical equilibrium constant \hat{K}_E is defined as:

$$\hat{K}_E = K_E \cdot \left(\frac{\sum c_m}{\sum \bar{c}_m} \cdot \frac{\bar{\gamma}_i}{\gamma_i}\right)^{-1} \cdot \left(\frac{\sum \bar{c}_m}{\sum c_m} \cdot \frac{\gamma_s}{\bar{\gamma}_s}\right)^{-\nu_i} = \left(\frac{\bar{c}_i}{c_i}\right) \cdot \left(\frac{c_s}{\bar{c}_s}\right)^{\nu_i} \quad (11)$$

Taking Eq. (10) and performing some mathematical rearrangements, the thermodynamic equilibrium constant is given by:

$$\ln \hat{K}_E = \left(-\frac{\Delta G_i^0}{RT} + \ln\left(\frac{\gamma_i}{\bar{\gamma}_i}\right) + \ln\left(\frac{\sum \bar{c}_m}{\sum c_m}\right)\right) + \nu_i \cdot \left(\frac{\Delta G_s^0}{RT} - \ln\left(\frac{\gamma_s}{\bar{\gamma}_s}\right) - \ln\left(\frac{\sum \bar{c}_m}{\sum c_m}\right)\right) \quad (12)$$

Following the model, the cluster of parameters in Eq. (12) represent the practical thermodynamic equilibrium constants, obtained from the SD model, as follows:

$$\ln \hat{K}_E = -\frac{\Delta \hat{G}_i^0}{RT} + \nu_i \cdot \frac{\Delta \hat{G}_s^0}{RT} \quad (13)$$

For further derivation, it is advantageous to introduce some approximations.

The density of the immobilized ligand, Λ (mol/L of pore volume) is fixed; and the material balance is given by:

$$\Lambda = \bar{c}_s + v_i \cdot \bar{c}_p \quad (14)$$

All experiments in this investigation were performed at low protein concentrations (i.e., working in the linear range of the isotherm). The concentration of the counter-ion in the adsorbate is much higher, compared to the protein concentration ($\bar{c}_s \gg \bar{c}_p$). As a result, the sum of all species in the bound state can be simplified to $\Lambda \approx \bar{c}_s \approx \sum \bar{c}_m$.

Additionally, the sum of all molar concentrations in solution $\sum c_m$, can be reduced to the molarity of pure water c , since the major constituent is water (Mollerup et al., 2010).

For the species in solution ideal behavior is assumed and the activity coefficients $\gamma_{s/i}$ are set to 1. Models for activity coefficients of simple electrolytes (Hückel & Debye, 1923; Pitzer, 1991) and proteins (Mollerup, Breil, Vogelpohl, & Sadowski, 2011) in solution are available, but it will make the isotherm models much more elaborate to include such models. Besides, Mollerup et al. (Mollerup, 2014) showed that the equilibrium excess energy is not sensitive to salt concentration variations when using halides salts in IEC, and therefore can be disregarded. These assumptions lead to the expression of Eq. (12) as:

$$\ln \hat{K}_E = \left(-\frac{\Delta G_i^0}{RT} + \ln\left(\frac{1}{\bar{\gamma}_i}\right) + \ln\left(\frac{\Lambda}{c}\right) \right) + v_i \cdot \left(\frac{\Delta G_s^0}{RT} - \ln\left(\frac{1}{\bar{\gamma}_s}\right) - \ln\left(\frac{\Lambda}{c}\right) \right) \quad (15)$$

To determine the exchanger phase activity coefficients, the Wilson model is introduced (Binh S. Vo & David C. Shallcross, 2005; Wilson, 1964). For a single binary system, the activity coefficients for the first species γ_1 and second species γ_2 , can be expressed as:

$$\ln \bar{\gamma}_1 = -\ln(x_1 + A_{1/2} \cdot x_2) + x_2 \cdot \left(\frac{A_{1/2}}{x_1 + A_{1/2} \cdot x_2} - \frac{A_{2/1}}{x_2 + A_{2/1} \cdot x_1} \right) \quad (16)$$

$$\ln \bar{\gamma}_2 = -\ln(x_2 + A_{2/1} \cdot x_1) + x_1 \cdot \left(\frac{A_{1/2}}{x_1 + A_{1/2} \cdot x_2} - \frac{A_{2/1}}{x_2 + A_{2/1} \cdot x_1} \right) \quad (17)$$

where, $A_{1/2}$ and $A_{2/1}$ represent the molecular interaction parameters between the present species in a binary mixture. Being, x_1 the mole fraction of the first species (i.e.,

protein) and x_2 the mole fraction of the second species (i.e., salt). Following the same useful considerations as before ($\bar{c}_s \gg \bar{c}_p$), the mole fraction of the salt will tend to 1 ($x_2 \approx 1$), and the activity coefficient of the protein at infinite dilution is,

$$\ln \bar{\gamma}_i^{\infty} = 1 - \ln(A_{1/2}) - (A_{2/1}) \quad (18)$$

The activity coefficient of the counter-ion in the adsorbate state $\bar{\gamma}_s$, is 1 ($\ln \bar{\gamma}_s \rightarrow 0$), when ($x_1 \rightarrow 0$) in Eq. (17).

On the other hand, the activity coefficient of the protein in the adsorbate state $\bar{\gamma}_i$, shows a ligand density dependency, which can be derived from the partial molar excess function (Prausnitz, 1999):

$$\left(\frac{\partial(n_T g^E / RT)}{\partial n_i} \right)_{T,P,n_{j \neq i}} = \bar{g}_i^E = \ln \bar{\gamma}_i \quad (19)$$

where n_i is the number of moles of i , n_T is the total number of moles of the bound species, g^E is the molar excess Gibbs energy, \bar{g}_i^E the partial molar excess Gibbs energy, and the subscript T and P represents a constant temperature and pressure, while $n_{j \neq i}$ indicates that the number of moles of all components are kept constant except for i .

Multiplying Eq. (19) on both sides of the equation with $(n_{T,\Lambda} / n_{T,\Lambda_{ref}})$, gives:

$$\begin{aligned} \left(\frac{n_{T,\Lambda}}{n_{T,\Lambda_{ref}}} \right) \cdot \left(\frac{\partial(n_{T,\Lambda_{ref}} g^E / RT)}{\partial n_i} \right)_{T,P,n_{j \neq i}} &= \left(\frac{n_{T,\Lambda}}{n_{T,\Lambda_{ref}}} \right) \cdot \ln \bar{\gamma}_{i,n_{T,\Lambda_{ref}}} \\ \therefore \left(\frac{\partial(n_{T,\Lambda} g^E / RT)}{\partial n_i} \right)_{T,P,n_{j \neq i}} &= \ln \bar{\gamma}_{i,n_{T,\Lambda}} \end{aligned} \quad (20)$$

where $n_{T,\Lambda}$ is the total number of moles of a bound species at a determined ligand density and $n_{T,\Lambda_{ref}}$ is the total number of moles of a bound species at the reference ligand density. For low protein concentrations, $(n_{T,\Lambda} / n_{T,\Lambda_{ref}})$ can be expressed in terms of the ligand density $((n_{T,\Lambda} / n_{T,\Lambda_{ref}}) \approx (\Lambda / \Lambda_{ref}))$ as follows:

$$\ln \bar{\gamma}_{i,n_T,\Lambda} = \left(\frac{n_{T,\Lambda}}{n_{T,\Lambda_{ref}}} \right) \cdot \ln \bar{\gamma}_{i,n_T,\Lambda_{ref}} = \left(\frac{\Lambda}{\Lambda_{ref}} \right) \cdot \ln \bar{\gamma}_{i,n_T,\Lambda_{ref}} \quad (21)$$

When choosing an appropriate reference state (e.g., $\Lambda_{ref} = 1$ mol/L of pore volume), the activity coefficient at infinite dilution of the protein can be expressed as:

$$\ln \bar{\gamma}_{i,\Lambda}^{\infty} = \Lambda \cdot \ln \bar{\gamma}_{i,\Lambda_{ref}}^{\infty} = \Lambda \cdot \left(1 - \ln(A_{1/2}) - (A_{2/1}) \right) \quad (22)$$

The introduction of Eq. (22) into Eq. (15) shows that the equilibrium distribution is affected by changes in the total resin capacity. The thermodynamic retention factor $A_{i,\Lambda}$ at low protein concentrations, when considering Eqs. (15) and (22), yield the following expression:

$$A_{i,\Lambda} = \exp \left(-\frac{\Delta G_i^0}{RT} + \ln \frac{\Lambda}{c} - \Lambda \cdot \left(1 - \ln(A_{1/2}) - (A_{2/1}) \right) + v_i \left(\frac{\Delta G_s^0}{RT} - \ln \frac{\Lambda}{c} \right) \right) \cdot \left(\frac{\Lambda}{c_s} \right)^{v_i} \quad (23)$$

2.6.3 Linear gradient elution model

By using a continuous-flow plate model, Yamamoto et al. (S. Yamamoto et al., 1983) developed a mathematical model describing the retention of proteins in ion exchange chromatography from linear gradient elution (LGE) experiments. In this work, LGE experiments were performed by a linear increase in the counter-ion concentration overtime at a fixed pH value or an increase on the pH overtime at a fixed counter-ion concentration. The correlation of the normalized gradient slope and the retention factor A_i is described as (Y. F. Lee, Graalfs, & Frech, 2016):

$$\frac{dGH_{salt}}{dc_{s,elu}} = \frac{dGH_{pH}}{dc_{pH,elu}} = \frac{1}{k_{d,i} \cdot A_i + k_{d,i} - 1} \quad (24)$$

where $c_{s,elu}$ is the eluting salt concentration, $k_{d,i}$ is the exclusion factor of the protein and the normalized salt gradient slope GH is given as (L. Pedersen, Mollerup, Hansen, & Jungbauer, 2003):

$$GH_{salt} = g_{salt} (V_c(1 - \varepsilon)\varepsilon_P) = \frac{c_{salt, final} - c_{salt, initial}}{V_g} (V_c(1 - \varepsilon)\varepsilon_P) \quad (25)$$

where, g_{salt} is the gradient slope, $c_{salt, initial}$ is the initial and $c_{salt, final}$ is the final counter-ion concentration in the gradient. V_g is the gradient volume, V_c is the total

column volume, ε is the interstitial porosity of the packed column, and ε_p the intraparticle porosity. Meanwhile, the normalized pH gradient slope is described as:

$$GH_{pH} = g_{pH} (V_c(1 - \varepsilon)\varepsilon_p) = \frac{c_{pH, final} - c_{pH, initial}}{V_g} (V_c(1 - \varepsilon)\varepsilon_p) \quad (26)$$

where, g_{pH} is the gradient slope, $c_{pH, initial}$ is the initial and $c_{pH, final}$ is the final pH in the linear pH gradient.

The relationship between the eluting counter-ion concentration and the normalized gradient slope in the linear range of the isotherm is given by (S. Yamamoto et al., 1983):

$$\int_{c_{s,initial}}^{c_{s,elu}} c_s^{\nu_i} dc_s = GH_{salt} \frac{A_i}{L_c} \int_0^{L_c} dx \quad (27)$$

with the column length L_c and the peak position from the column inlet x .

To describe the characteristic charge ν_i on the AEX resins, a pH and ligand density approximation was considered. Since it is well known that the characteristic charge ν_i is directly influenced by the protein, the pH and the chromatographic medium (Linda Pedersen, 2003; L. Pedersen et al., 2003). In this work, a protein charge model based on Schmidt et al. (Schmidt, Hafner, & Frech, 2014) equation was used. The narrow operational pH range at which the experiments in this work were performed allows the simplification of the characteristic charge to a single ionizable group. Additionally, we propose that a simple linear empirical model is sufficient to describe the ligand density dependency on the characteristic charge, as follows:

$$\nu_i = \nu_0 + \frac{N_1}{1 + 10^{(pKa_i - pH)}} + \frac{N_2 \cdot \Lambda}{1 + 10^{(pKa_i - pH)}} \quad (28)$$

where pKa_i is the dissociation constant of the ionizable group, and ν_0 describes the charge of the protein at pH values that are well below the pKa. Here, a distinction in between the number of amino acids involved on the protein-ligand binding which are affected by the ligand density variation (N_2) and those which are not (N_1) was included.

On the other hand, the broad pH range applied on the CEX experiments did not allowed the use of the simplified equation of the characteristic charge (Eq. (28)). Therefore, the protein net charge model of Schmidt et al. was used without any modification as follows (Schmidt et al., 2014):

$$v_i = \sum_i - \frac{N_{-i}}{1 + 10^{(pKa_i - pH)}} + \sum_i \frac{N_{+i}}{1 + 10^{(pH - pKa_i)}} \quad (29)$$

being N_{-i} the number of acidic amino acids and N_{+i} the number of basic amino acid, which are contributing to the interaction in between the protein and the chromatographic resin. Here, it was assumed, that the position of the amino acid in the protein sequence does not influence the pKa value of each amino acid.

2.6.4 Donnan ion exchange model

The SD model has some limitations since it is derived assuming a complete exclusion of co-ions in the stationary phase, and the maximum uptake of counter-ions in the resin phase is equivalent to the ligand density. These assumptions lead to a complete disregard to the change in the protein charge caused by electrostatic interactions with the adsorbent surface (e.g., differences in the intraparticle pH), even though this effect has been extensively studied and shown in the literature (Hardin & Ivory, 2006; Jansen, Straathof, Wielen, Luyben, & Tweel, 1996; Shen & Frey, 2004, 2005; Wittkopp, Peeck, Hafner, & Frech, 2018). To investigate this effect further, the ratio of the ion concentrations between the adsorbate and the liquid phase (r_D) in AEX was calculated by using the equation presented by Wittkopp et al. (Wittkopp et al., 2018),

$$r_D = \frac{c_{Cl^-}^R}{c_{Cl^-}^B} = \frac{\Lambda}{2c_{Cl^-}^B} + \sqrt{S_{Cl^-,OH^-} S_{Na^+,H^+} + \left(\frac{\Lambda}{2c_{Cl^-}^B}\right)^2} \quad (30)$$

where the superscripts R and B refers to the chloride concentration on the resin and the mobile phase, respectively, Λ denotes the ligand density per pore volume and S symbolizes the selectivity constant for the anions and cations. As long as the system contains only NaCl, and the pH is not extremely low or high (i.e., the concentrations of OH^- and H^+ are small compared to the concentration of other ions), Eq. (30) can be applied. For simplicity, in this work, the selectivity of all ions was set to 1, an assumption that has been proved to be pertinent in previous publications (Jansen et al., 1996; Kawakita & Matsuishi, 1991; Wittkopp et al., 2018). Hence, the pH value in the resin phase for AEX resins can be calculated as:

$$pH_R = pH_B + \log_{10}(r_D) \quad (31)$$

where pH_B refers to the pH value in the mobile phase. The evaluation of cation exchange resins is possible by considering the negative charge of the ligand and the presence of the respective counter-ion.

2.6.5 Determination of the model parameters

For each linear salt and pH gradient experiment run the normalized gradient slope was calculated with Eq. (25) and (26), respectively. Subsequently, the data points correlating the eluting chloride concentration and the eluting pH values with the normalized gradient slope were transferred to Berkeley Madonna™. The results of the LGE experiments, at fixed pH values, were fitted simultaneously into Eqs. (5) and (6) in Berkeley Madonna™ (fourth-order Runge-Kutta). By using the “Curve-fit” function of the software, the thermodynamic parameters $\Delta\hat{G}_p^0/RT$ and $\Delta\hat{G}_s^0/RT$ as well as the number of binding sites ν_i , were determined for each protein at a given resin. The applicability of the ligand density SD model to cation exchange resins was done with the same fitting approach as described before with the addition of Eq. (23) and the description of the number of binding sites showed in Eq. (29).

As shown in literature (Osberghaus et al., 2012; Pfister, Steinebach, & Morbidelli, 2015), the determination of the number of binding sites by solving the partition coefficient A_i of the SD model with the 0th order approximation (i.e., $k_{d,i} = 1$), significantly deviates from the solution obtained when using a numerical solution. Therefore, in this work, the guess values for the number of binding sites (ν_i) were set to a boundary condition of $\pm 20\%$ of the solution with the 0th order approximation (or Yamamoto’s equation). The curve fits were repeated using different combinations of guess values, until achieving the combination with the smallest root mean square deviation.

For the simulation, the column was divided into $N = 20$, evenly sized sections. Berkeley Madonna™ was used to solve the differential equations by applying the Rosenbrock (stiff) solver.

2.6.5.1 Linear gradient elution experiments

The production of samples that represents a wide range of biopharmaceutical types was the main concern when developing the data sets for mechanistic modeling in this project. The LGE runs were carried out with different model proteins and their preparation previous to these runs are shown in section 2.5. The sequence followed to

perform the LGE experiments is described in **Table 9**. After the gradient a cleaning in place (CIP) step was performed to ensure the removal of precipitated proteins or other contaminants. The anion exchange cleaning buffer contain 0.02 mol/L Bis-Tris propane and 1.0 mol/L NaCl at pH 7.0. For the cation exchange pH gradients a buffer containing 0.10 mol/L CAPS and 1.0 mol/L NaCl at pH 10.50 was applied. Whereas for the CEX salt gradients the CIP-buffer consisted of 0.02 mol/L Na₂PO₄ and 1.0 mol/L NaCl at pH 7.0.

Table 9: Chromatographic steps to perform a bind and elute mode.

Step	Buffer	Duration
Equilibration	Binding buffer	5 CV
Sample application	Sample + Binding buffer	*
Wash	Binding buffer	10 CV
Elution	Binding and Elution buffer	*
Cleaning	CIP buffer	10 CV
Reequilibration	SEC	10 CV

^{*)} meaning a variable condition specific to each LGE run.

The buffers used for each LGE condition are described in the following sections in accordance to the functional group of the prototype resin.

2.6.5.1.1 Anion exchange LGE experiments

The LGE experiments with BSA and mAb were carried out on an ÄKTA purifier™ 100 system. Five salt gradients were performed at constant pH values; mAb experiments were performed from pH 9.0 to 10.0 and BSA experiments from pH 7.0 to 8.0, with an increment of 0.25 pH units in between. The equilibration buffer consisted of 0.03 mol/L 1,2-diaminopropane, and HCl was added to obtain a final concentration of 0.05 mol/L. Additionally, the elution buffer contained 0.95 mol/L NaCl, and the desired pH value was finally adjusted with NaOH. This was done to keep a constant chloride concentration within the equilibration (0.05 mol/L) and the elution buffer (1.0 mol/L), and therefore a constant gradient slope at all pH values. The gradient volumes tested were 15, 25, 40, 65 and 100 column volumes (CV). The volumetric flow rate was

1.0 mL/min and the sample loading was fixed to 1 mg/mL packed resin for all proteins. The position of the eluting peak was determined using PeakFit v4.12. The UV signal was fitted to an exponentially modified gauss function (EMG) and the eluting salt concentration c_s was determined from the conductivity at the peak center. The dead volume between the UV and the conductivity cell was taken into account, for each system as shown in section 2.7.1.

2.6.5.1.2 Cation exchange LGE experiments

After the knowledge gained with the anion exchange results, a decision to expand the design space was done. The CEX dataset includes salt and pH gradients. All the experiments with mAb04 charge variants were carried out on an ÄKTA purifier™ 10 system. The pH LGE experiments were carried out with a discontinuous buffer system as shown in **Table 10**. The linear pH gradient elution experiments were performed in the presence of constant counter-ion concentrations. These concentrations were set to 100, 125, 150, 175 and 200 mmol/L.

Table 10: Discontinuous buffer system to achieve a linear pH gradient.

Substance	Binding buffer concentration (mmol/L)	Elution buffer concentration (mmol/L)
Acetic acid	11.5	-
MES monohydrate	2.4	-
MOPSO	3.5	3.5
CAPS	3.0	2.2
Succinic acid	-	22.0
HEPES	-	5.8
TAPS	-	3.6
CHES	-	2.3
NaOH	7.4	59.7
NaCl	92.6	40.3

Substance	Binding buffer concentration (mmol/L)	Elution buffer concentration (mmol/L)
pH	4.75	10.00

To achieve interchangeability between the pH and salt gradients, and rule-out any influences on the presence of co-ions in the chromatography resin, a mixture of the buffer system in **Table 10** to prepare the salt gradients at a fix pH was done. The substances concentration needed of the binding and elution buffer, to obtain the desire pH value, was calculated. This method ensures the same concentration of each buffer substance in the salt and pH gradients. The salt LGE experiments were carried-out with a homogeneous buffer system as shown in **Table 11**.

Table 11: Homogeneous buffer system to achieve a linear salt gradient.

pH value	Buffer substance	Na⁺ concentration
7.0	Mixture of Table 10	50 – 1000 mmol/L
7.5	Mixture of Table 10	50 – 1000 mmol/L
8.0	Mixture of Table 10	50 – 1000 mmol/L

The sample loading was fixed to 1 mg/mL, 0.5 mg/mL and 0.2 mg/mL packed resin for the basic, neutral and acidic variant, respectively. The shortage of the amount of charge variant sample led to set different protein concentrations. Nevertheless, the low concentrated sample proved to be sufficient for the LGE experiments. A volumetric flow rate of 1.67 mL/min, which equals a linear flow rate of 200 cm/h was applied. The gradient slopes were generated by using gradient volumes of 40, 60, 80 and 120 CV. The dead volume between the UV and the conductivity cell was taken into account, for each system as shown in section 2.7.1.

2.6.6 Column simulation model

For the simulation of the protein elution profiles in salt and pH gradient elution, a lumped rate model was applied (Schmidt-Traub et al., 2012):

$$\frac{\partial c_i}{\partial t} + u_{init} \cdot \frac{\partial c_i}{\partial x} + \frac{(1 - \varepsilon)\varepsilon_P k_{d,i}}{\varepsilon} \cdot \frac{\partial q_i^*}{\partial t} = D_{ax} \cdot \frac{\partial^2 c_i}{\partial x^2} \quad (32)$$

being, c_i the mobile phase concentration of species i , u_{init} the interstitial mobile phase velocity, q_i^* the overall concentration in the accessible pore volume and D_{ax} the axial dispersion coefficient. A linear driving force approximation is used to describe the mass transfer in the column:

$$\frac{\partial q_i^*}{\partial t} = k_{eff} \cdot \frac{6}{d_p} \cdot (q_{eq}^* - q_i^*) \quad (33)$$

with the effective mass-transfer coefficient k_{eff} , the particle diameter d_p and the hypothetical loading when both phases are in equilibrium q_{eq}^* . The adsorption equilibrium for the ligand density SD model ($A_{i,\Lambda}$) at low protein loadings is represented as:

$$q_{eq}^* = (A_{i,\Lambda} + 1) \cdot c_i \quad (34)$$

$$= c_i \cdot \left(\exp\left(-\frac{\Delta G_i^0}{RT} + \ln \frac{\Lambda}{c} - \Lambda \cdot (1 - \ln(A_{1/2}) - (A_{2/1}))\right) + \left(v_i \frac{\Delta G_s^0}{RT} - \ln \frac{\Lambda}{c}\right) \right) \cdot \left(\frac{\Lambda}{c_s}\right)^{v_i} + 1$$

2.6.6.1 Inverse estimation of the mass transfer coefficient

The effective mass transfer coefficient k_{eff} was estimated by fitting the protein elution curves of the salt and pH gradients at low protein load. This parameter was the only parameter that was varied to fit the experimental data.

2.7 Determination of column parameters

Before performing the modeling experiments, it is necessary to characterize the system and the chromatographic columns. The plant dispersion and the column effects causes dead times and band broadening. Therefore, to obtain reasonable agreement between experimental results and process simulation, these contributions have to be determined.

2.7.1 Dead volumes of the Äkta system

The dead volumes of the system are determined without columns. The system is filled with 0.2 mol/L MES, 150 mM NaCl at pH 6.0. To calculate the delay volume between the UV, conductivity and pH detectors, an individual tracer of 1 mg/mL Dextran (blue), 1 mol/L NaCl and 0.1 mol/L NaOH are injected using a 50 μ L sample loop. The

experiment is performed with a flow rate of 1.0 mL/min, and the retention volume is read-out from the chromatogram. The measurements are done in triplicates. To calculate the dead volumes is important to remember that the tracer starts in the injection valve, then passes to the bypass pipe and exit to the UV detector, then passes the conductivity cell and finally to the pH electrode. The tracer injection of salt and UV without column are defined as $V_{system-salt}$ and $V_{system-UV}$, respectively.

2.7.2 Column porosities

The interstitial porosity ε , is the volume between the particles, while the intraparticle porosity ε_p , is the fraction of the volume occupied by the pore inside the particle. The total porosity ε_t , is the volume fraction of the liquid phase in the column. The porosities are related by (L. Pedersen et al., 2003):

$$\varepsilon_t = \varepsilon + (1 - \varepsilon) \cdot \varepsilon_p \quad (35)$$

The total porosity is determined by a pulse injection of a small tracer that can enter the pores in the stationary phase. Then, the measured retention volume is corrected by the dead volume as follows:

$$\varepsilon_t = \frac{V_{salt} - V_{system-salt}}{V_c} \quad (36)$$

The interstitial porosity is determined by a pulse injection of a large tracer that cannot enter the pores in the stationary phase. Then, the measured retention volume is corrected by the dead volume as follows:

$$\varepsilon = \frac{V_{dex} - V_{system-UV}}{V_c} \quad (37)$$

While the intraparticle porosity can be calculated from the relation in Eq. (35) as follows:

$$\varepsilon_p = \frac{(\varepsilon_t - \varepsilon)}{(1 - \varepsilon)} \quad (38)$$

2.7.2.1 Anion exchange porosities

For the determination of the interstitial porosity, a pulse with 1.0 mg/mL dextran (MW ~ 2,000,000 g/mol) in 0.15 mol/L NaCl, in a 50 μ L sample loop was applied and

the elution volume of dextran was detected by an external Smartline RI-detector. For the determination of the total porosity, a salt pulse of 1.0 mol/L NaCl was injected and the elution volume was detected by the conductivity cell in the ÄKTA purifier™ 100 system. For both methods, the system dead volume between the injection valve and the detector was taken into account.

2.7.2.2 Cation exchange porosities

To assess the influence of the mobile pH on the determination of the porosities two buffers of 0.02 mol/L MES with 0.05 mol/L NaCl at pH 6.0 and 0.02 mol/L MOPSO with 0.05 mol/L NaCl at pH 7.0 were tested. The influence of the salt concentration in the mobile phase was also investigated on the buffer at pH 6.0 with 0.05 mol/L NaCl, 0.10 mol/L NaCl and 0.15 mol/L NaCl. For the determination of the interstitial porosity, a pulse with 1.0 mg/mL dextran blue (MW ~ 2,000,000 g/mol) in a 50 µL sample loop was applied and the elution volume of dextran was detected by the UV cell in the ÄKTA purifier™ 10 system. For the determination of the total porosity, a salt pulse of 1.0 mol/L NaCl was injected and the elution volume was detected by the conductivity cell in the ÄKTA purifier™ 10 system. For both methods, the system dead volume between the injection valve and the detector was taken into account.

2.7.3 Exclusion factor

The volume in the particle available for a molecule is $\varepsilon_p k_d$, where k_d is an exclusion factor that per definition is 1 for salt and less than 1 for large molecules like proteins. The exclusion factor $k_{d,i}$ is determined from the retention volume of the protein at non-binding conditions:

$$k_{d,i} = \frac{\frac{V_{NA}}{V_c} - \varepsilon}{(1 - \varepsilon) \cdot \varepsilon_p} \quad (39)$$

For BSA and mAb03 the exclusion factor $k_{d,i}$ was estimated for each protein with values obtained from published data. Having the lowest $k_{d,i}$ value for the high molecular weight protein, and the highest $k_{d,i}$ value for the lower molecular weight protein; $k_{d, \text{mAb}} = 0.6$ (Thomas et al., 2013), and $k_{d, \text{BSA}} = 0.7$ (L. Pedersen et al., 2003).

To determine the charge variants exclusion factors, non-binding conditions at high salt concentration, and high pH were evaluated. A protein pulse of each purified charge

variant (1.0 mg/mL) was injected into the column equilibrated with 0.02 mol/L TAPS in 1.0 mol/L NaCl buffer at pH 8.0. A sample loop of 50 μ L was used to inject the sample. Whereas, the high pH influence was investigated with 0.02 mol/L CAPS in 0.05 mol NaCl at pH 10.50. In all cases the dead volumes between the injection valve and the respective detector was taken into account.

2.7.4 Ligand density

The ionic capacity of the gravity settled resin of each prototype was provided by the manufacturer (see **Table 4** and **Table 5**). The ligand density of the settled resin is calculated using a constant swelling factor SF that is assumed to be constant for all resins used in this work ($SF = 5$).

$$\Lambda_{settled} = \frac{\Lambda_{dry}}{SF} \quad (40)$$

The ligand density of the packed bed is associated to the ionic capacity of the settled resin with the following equation:

$$\Lambda_{packed} = \Lambda_{settled} \frac{1}{(1 - CF)} \quad (41)$$

where CF is the compression factor used to pack the resin. For the chromatographic resin family Fractogel[®] EMD a CF of 0.15 was applied. The ionic capacity of the resins, in relation to the pores, is calculated as:

$$\Lambda_{pore} = \frac{\Lambda_{packed}}{(1 - \varepsilon) \cdot \varepsilon_p} \quad (42)$$

2.7.5 Axial dispersion

In preparative chromatography the packing of the column and the fluid dynamics deviations coming from the plug flow can be represented with the axial dispersion coefficient D_{ax} (Schmidt-Traub et al., 2012). To determine the D_{ax} coefficient for the CEX resins, a buffer with 0.02 mol/L MES and 0.05 mol/L NaCl at pH 6.0 was used as the mobile phase. A tracer pulse with 1.0 mg/mL dextran blue (MW ~ 2,000,000 g/mol) in a 50 μ L sample loop was applied and different flow rates were tested in triplicates. The elution volume of the dextran was detected by the UV cell in the ÄKTA purifier[™] 10 system and analyzed with the Peakfit[®] software. The investigated volumetric flow rates

were 1.67, 1.50, 1.25, 1.00, 0.75 and 0.5 mL/min. The chromatograms at each velocity were evaluated with the EMG function and the first and second moments were determined. With this parameters, the D_{ax} value can then be calculated as follows (Osberghaus et al., 2012):

$$D_{ax} = \frac{\sigma_{mom}^2 L_c u_{int}}{\mu_{mom}^2 2} \quad (43)$$

with L_c being the column length, u_{int} the interstitial velocity and μ_{mom} and σ_{mom} the first respectively second central moment of the non-binding and non-penetrating tracer peaks.

2.8 Analytical size exclusion chromatography (SEC)

The stability of the monoclonal antibodies was monitored through the content of dimers and high molecular weight species (HMW) in the sample by SEC analysis. All samples were analyzed in a Phenomenex® BioSep-SEC-S3000 column ($V_c = 14.34$ mL) running on an ÄKTA™ micro system. The mobile phase buffer contained 0.05 mol/L NaH_2PO_4 , 0.3 mol/L NaCl and 0.02% NaN_3 . The final pH of the buffer was adjusted with NaOH until a value of 7.0 was achieved. The column was operated at a volumetric flow rate of 1 mL/min. The injection volume of the sample was 100 μL , and the protein concentration was always lower than 1 mg/mL. An isocratic elution of the sample was performed in this analysis.

2.9 Analytical cation exchange chromatography (CEX)

The analysis of mAb04 charge variants was carried out using a BioPro™ SP-F column ($V_c = 0.83$ mL) from YMC Europe GmbH. The binding and elution buffers described in **Table 8** were used for the CEX analysis. The injection volume of the sample was 100 μL , and the protein concentration was always lower than 1 mg/mL. After the sample injection, the column was washed with 1 CV of equilibration buffer, followed by 1 CV of 50% elution buffer before eluting the proteins using a linear pH gradient from 50 to 85% elution buffer in 8.75 CV. A final step to 100% elution buffer in 2.25 CV was applied to strip the remaining of the protein in the column. The column was operated at a volumetric flow rate of 0.83 mL/min.

3 RESULTS

3.1 Modeling of anion exchange resins

3.1.1 AEX column parameters

To determine the column parameters is imperative to account for the dead volumes of the chromatographic system. The determination of the Äkta Explorer 100, where the experiments for BSA and mAb03 were carried out, yielded a dead volume of 0.07 mL between the UV signal measurement and the conductivity cell. This value was used to adjust all the conductivity measurements coming from the retention values read-outs from the UV signal.

Table 12 shows the experimentally measured values for the total porosity (ε_t), interstitial porosity (ε) and the intraparticle porosity (ε_p) obtained from the injection of dextran on all 13 prototype resins. Examining the values for the total porosity (ε_t), a decrease is observed when the ligand density is increased. But the variability of the data on the interstitial porosity (ε) and the intraparticle porosity (ε_p) is significant and no clear trend is observed. The difference on the standard deviation between the resins shown in **Table 12** indicates the variability on the experimental determination. Although the values are relatively consistent, it is difficult to determine if the variability is coming from the practical determination, or the measurement is really showing the influence of the ligand density on the parameters.

Since literature has shown that the practical determination of the porosities often experiences difficulties (Carta & Jungbauer, 2011; Linda Pedersen, 2003; L. Pedersen et al., 2003; Schmidt-Traub et al., 2012), especially on anion exchange resins, a simplification of the values was made. The interstitial porosity ε and the total porosity ε_t were estimated as 0.35 and 0.8, respectively (Schmidt-Traub et al., 2012). The intraparticle porosity ε_p was calculated from the total porosity and the interstitial porosity (i.e., using Eq. (38)). This assumption was made since previous publications had shown that the correlation of the data, is not sensible to the choice of the porosity, when reasonable values of ε are used (L. Pedersen et al., 2003). Lastly, the ligand density in the pore volume was calculated with equation (42) and by implementing the estimated porosities ($\varepsilon = 0.35$ and $\varepsilon_t = 0.8$).

Table 12: Determined porosities and ionic capacity of thirteen strong anion exchange prototype resins.

Fractogel® EMD TMAE (M) prototypes:

Resin ID ^{a)}	Λ_{packed} ($\mu\text{eq}\cdot\text{mL}^{-1}$)	ε	ε_t	ε_p	$\Lambda_{\text{pore}}^{\text{b)}$ ($\text{mmol}\cdot\text{L}_{\text{pore}}^{-1}$)
RES 1	47.91	0.357 ± 0.008	0.832 ± 0.002	0.739	106.5
RES 2	57.32	0.360 ± 0.004	0.824 ± 0.002	0.725	127.4
RES 3	61.91	0.380 ± 0.002	0.837 ± 0.002	0.738	137.6
RES 4	68.24	0.369 ± 0.002	0.823 ± 0.003	0.719	151.6
RES 5	72.00	0.339 ± 0.007	0.796 ± 0.002	0.692	160.0
RES 6	74.14	0.375 ± 0.003	0.811 ± 0.003	0.697	164.8
RES 7	79.06	0.348 ± 0.002	0.816 ± 0.005	0.718	175.7
RES 8	81.41	0.355 ± 0.003	0.804 ± 0.002	0.696	180.9
RES 9	83.91	0.357 ± 0.002	0.803 ± 0.006	0.693	186.5
RES 10	101.65	0.343 ± 0.003	0.808 ± 0.002	0.708	225.9
RES 11	125.65	0.324 ± 0.002	0.795 ± 0.003	0.696	279.2
RES 12	155.76	0.323 ± 0.007	0.761 ± 0.005	0.648	346.1
RES 13	188.14	0.339 ± 0.003	0.747 ± 0.003	0.617	418.1

^{a)} sorted by Λ_{pore} in ascending order.^{b)} calculated from the Λ_{packed} according to Eq. (42) with $\varepsilon = 0.35$ and $\varepsilon_t = 0.8$.

3.1.2 Salt gradient elution of mAb03 and BSA in the linear range

The influence of ligand density variation on the elution behavior of mAb03 and BSA was investigated by the application of linear salt gradients at different pH values on thirteen prototype resins. The symbols in **Figure 1**, **Figure 2**, **Figure 3**, and **Figure 4** depict the experimentally determined eluting chloride concentrations for the model proteins, where mAb03 is represented by circles and BSA with squares. These series of experiments were performed at pH values of 9.0, 9.25, 9.5, 9.75, and 10.0 for mAb03 and at pH 7.0, 7.25, 7.5, 7.75, and 8.0 for BSA. By increasing the pH value in the mobile phase, the counter-ion elution concentration of both proteins increases. In these figures, it can be observed the disparity in the elution behavior of the proteins on the Fractogel® EMD TMAE (M) prototypes from the lowest to the highest ligand density (top to bottom). Noticeably, the eluting salt (chloride ion) concentration of both proteins is shifted to higher counter-ion concentrations when the ligand density is increased.

Similar elution behaviors have been observed in the literature, showing stronger retention of the protein in the resins with a higher ionic capacity (Fausnaugh, Kennedy, & Regnier, 1984; Y. F. Lee et al., 2016; D. Wu & Walters, 1992).

3.1.2.1 Ligand density dependency in the stoichiometric displacement model

The first step to understanding the effect of the ligand density variation was done by implementing the stoichiometric displacement (SD) model. The correlation of the experimental gradient elution data at different pH values, according to Eq. (5) and (6) is illustrated in **Figure 1**, **Figure 2**, **Figure 3**, and **Figure 4**. The predicted curves, represented by the straight/dashed lines in the figures, are described by the model parameters; $\Delta\hat{G}_i^0/RT$, $\Delta\hat{G}_s^0/RT$ and the number of binding sites (v_i). **Table 13** shows a summary of the fitted parameters for the thirteen ligand densities, and the graphical representation of this data can be found in **Figure 5** and **Figure 6**. The curve fitting results, when applying the SD model, showed that the predicted normalized gradient slope data is in good agreement with the experimental data.

Table 13: Fitted model parameters $\Delta\hat{G}_i^0/RT$, $\Delta\hat{G}_s^0/RT$, and v when applying the SD model for mAb03, and BSA on thirteen strong anion exchange prototype resins.

mAb		RES	RES	RES	RES	RES	RES	RES	RES	RES	RES	RES	RES	
		1	2	3	4	5	6	7	8	9	10	11	12	13
	$\Delta\hat{G}_i^0$	9.48	9.48	9.19	9.28	9.40	9.74	9.38	9.35	9.16	10.03	10.03	10.48	11.40
	$\Delta\hat{G}_s^0$	1.61	1.40	1.31	1.24	1.16	1.12	1.09	1.08	0.97	0.87	0.67	0.35	0.15
pH 9.00	v	5.76	6.22	6.11	6.05	6.55	6.74	6.51	6.41	6.59	6.71	6.60	7.19	7.84
pH 9.25	v	6.53	6.97	6.89	6.81	7.30	7.55	7.36	7.25	7.51	7.62	7.56	8.25	8.92
pH 9.50	v	7.50	8.05	7.96	7.84	8.58	8.90	8.59	8.37	8.83	8.91	8.87	9.85	10.58
pH 9.75	v	8.34	9.08	8.94	8.84	9.72	10.10	9.66	9.42	10.05	10.06	9.99	11.16	12.09
pH 10.0	v	10.25	11.19	11.07	10.87	12.13	12.62	12.10	11.80	12.81	12.45	12.28	14.21	15.67
BSA		RES	RES	RES	RES	RES	RES	RES	RES	RES	RES	RES	RES	
		1	2	3	4	5	6	7	8	9	10	11	12	13
	$\Delta\hat{G}_i^0$	4.25	3.86	3.95	3.79	4.17	3.95	3.57	3.70	3.74	4.16	4.23	4.08	4.73
	$\Delta\hat{G}_s^0$	1.24	1.01	1.00	0.87	0.90	0.84	0.76	0.75	0.71	0.53	0.36	0.11	-0.07
pH 7.00	v	5.29	5.55	5.52	5.59	5.86	5.83	5.98	5.85	6.01	6.70	6.75	7.20	7.74
pH 7.25	v	5.94	6.32	6.15	6.23	6.58	6.46	6.68	6.44	6.82	7.46	7.47	8.00	8.62
pH 7.50	v	6.42	6.94	6.72	6.91	7.10	7.11	7.28	7.10	7.40	8.13	8.19	8.75	9.57
pH 7.75	v	6.86	7.47	7.28	7.53	7.75	7.64	8.01	7.77	8.12	8.95	8.88	9.54	10.43
pH 8.00	v	7.27	8.11	7.71	7.91	8.29	8.19	8.62	8.31	8.53	9.39	9.39	10.10	10.99

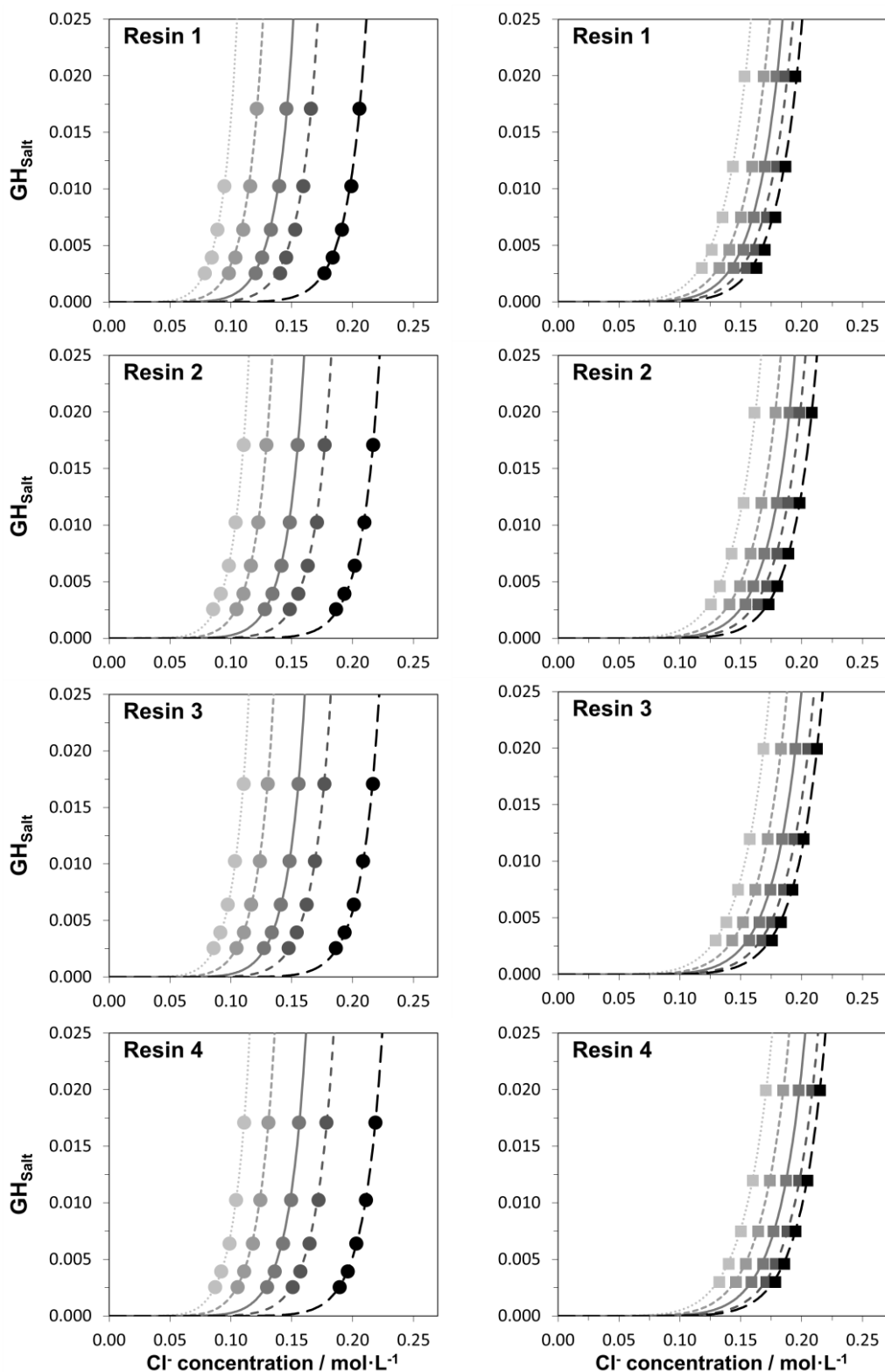


Figure 1. Eluting Cl^- concentrations of mAb (circles and lines) and BSA (squares and lines) as a function of the normalized salt gradient slope (GH_{salt}) on resin 1, 2, 3, and 4. The experiments were performed at pH values of 7.0 and 9.0 (● ■), 7.25 and 9.25 (◐ ◑), 7.5 and 9.5 (◒ ◓), 7.75 and 9.75 (◔ ◕), and 8.0 and 10.0 (◗ ◘) for mAb and BSA, respectively. Straight lines depict the fitting result with the SD model, whereas the symbols represent the experimental data obtained from the LGE runs.

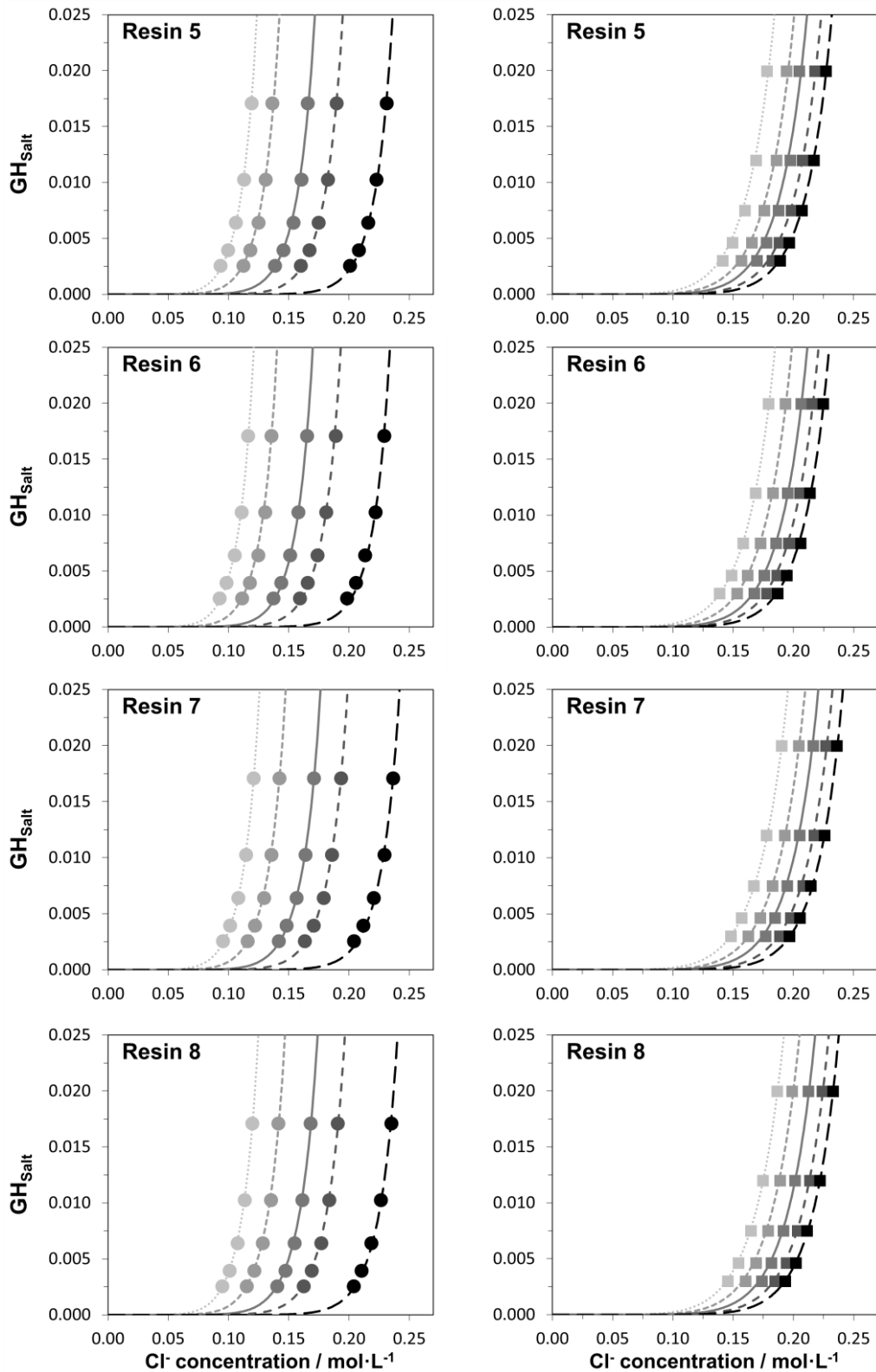


Figure 2. Eluting Cl^- concentrations of mAb (circles and lines) and BSA (squares and lines) as a function of the normalized salt gradient slope (GH_{salt}) on resin 5, 6, 7, and 8. The experiments were performed at pH values of 7.0 and 9.0 (● ■), 7.25 and 9.25 (● ■), 7.5 and 9.5 (● ■), 7.75 and 9.75 (● ■), and 8.0 and 10.0 (● ■) for mAb and BSA, respectively. Dashed/straight lines depict the fitting result with the SD model, whereas the symbols represent the experimental data obtained from the LGE runs.

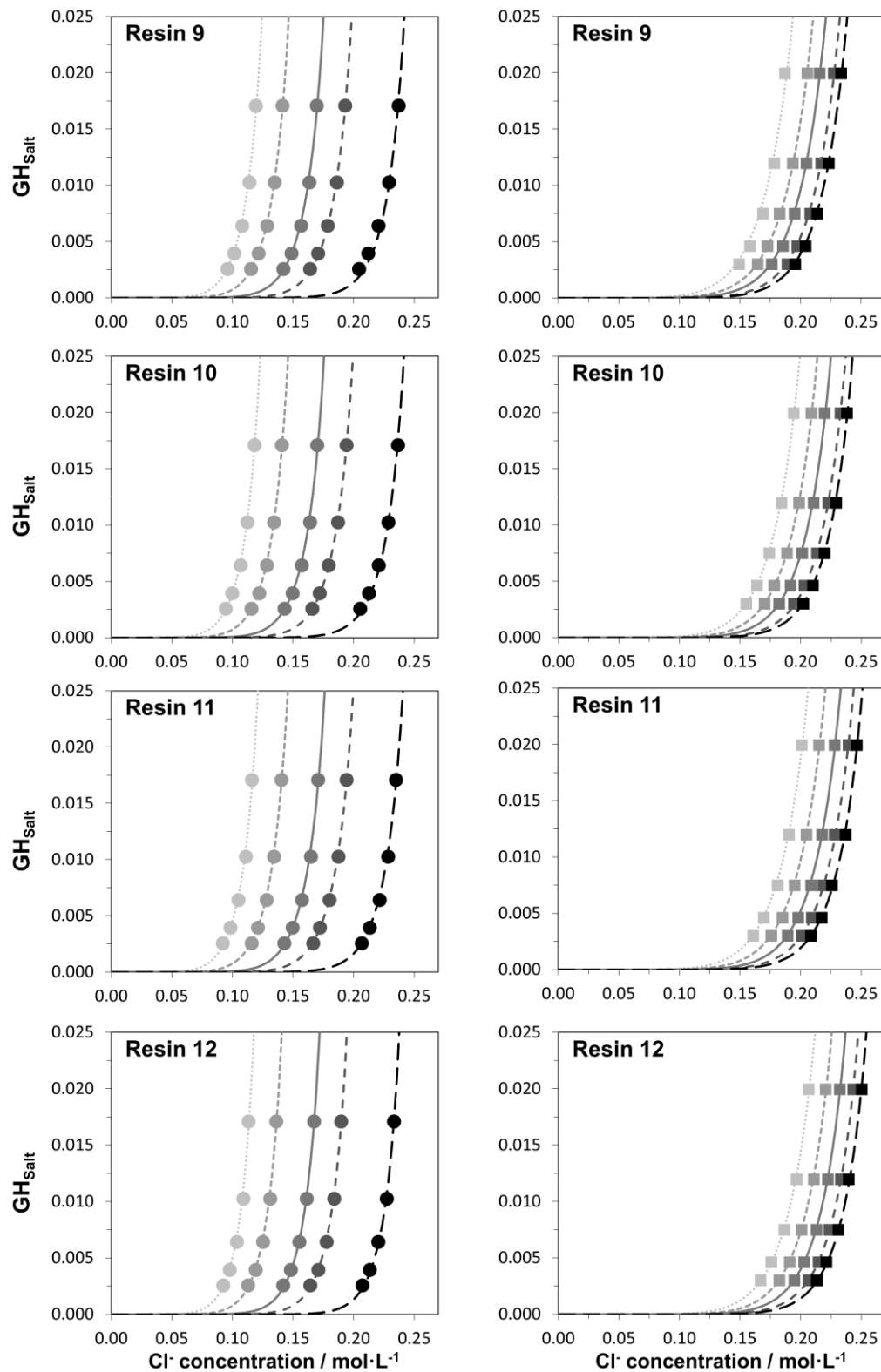


Figure 3. Eluting Cl^- concentrations of mAb (circles and lines) and BSA (squares and lines) as a function of the normalized salt gradient slope (GH_{salt}) on resin 9, 10, 11, and 12. The experiments were performed at pH values of 7.0 and 9.0 (\bullet \blacksquare), 7.25 and 9.25 (\circ \blacksquare), 7.5 and 9.5 (\bullet \blacksquare), 7.75 and 9.75 (\circ \blacksquare), and 8.0 and 10.0 (\bullet \blacksquare) for mAb and BSA, respectively. Straight lines depict the fitting result with the SD model, whereas the symbols represent the experimental data obtained from the LGE runs.

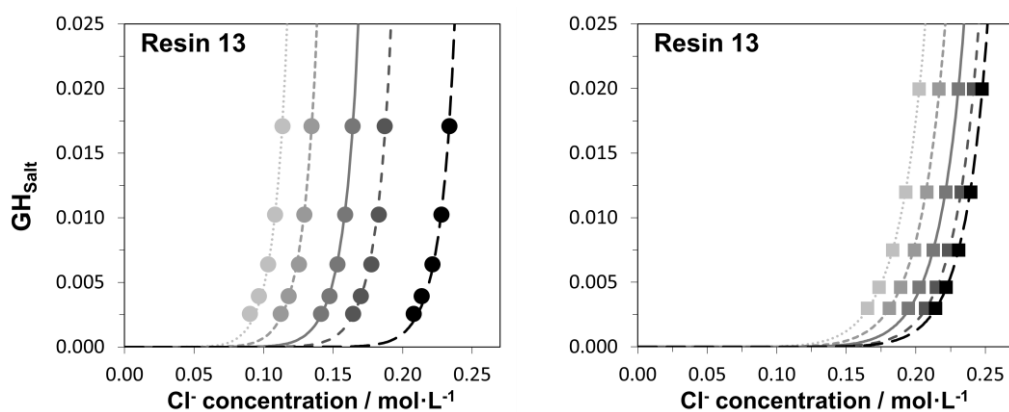


Figure 4. Eluting Cl^- concentrations of mAb (circles and lines) and BSA (squares and lines) as a function of the normalized salt gradient slope (GH_{salt}) on resin 13. The experiments were performed at pH values of 7.0 and 9.0 (• ■), 7.25 and 9.25 (• ■), 7.5 and 9.5 (• ■), 7.75 and 9.75 (• ■), and 8.0 and 10.0 (• ■) for mAb and BSA, respectively. Straight lines depict the fitting result with the SD model, whereas the symbols represent the experimental data obtained from the LGE runs.

3.1.2.2 Ligand density dependency of the characteristic charge (ν_i)

The obtained number of binding sites from the SD model (**Table 13**) for both proteins are displayed in **Figure 5**, where mAb03 is represented by black dots and BSA with squares. As previously mentioned, the initial guess values to calculate the number of binding sites was set to the ν_i values derived from the $\log\text{GH}_{\text{salt}} - \log\text{C}_s$ graphical determination by Yamamoto's approach (data not shown). This assumption was made based on Pfister and coworkers' results, where they observed a relative error of the number of binding sites of up to 12% when solving for the 0th order approximation solution (Pfister et al., 2015). Therefore, in this work, these values were used as a first approximation, and a variation of $\pm 20\%$ was allowed to ensure the ν_i values were in the correct range.

For both model proteins, a dependency on pH and ligand density is noted. An apparent increase in the estimated ν_i values is observed when either the pH or the ligand density is increased. Under all investigated conditions, the characteristic charge ν_{mAb} of the mAb is greater than the characteristic charge ν_{BSA} of BSA. To describe the observed dependencies, a modified protein net charge model was implemented (see equation (28)). The surface in **Figure 5** represents the prediction of ν_i when using the parameters in **Table 14** for mAb03 and BSA. This shows that the prediction with the obtained model parameters is in good agreement and that the simplified protein net charge model is able to describe the observed effects.

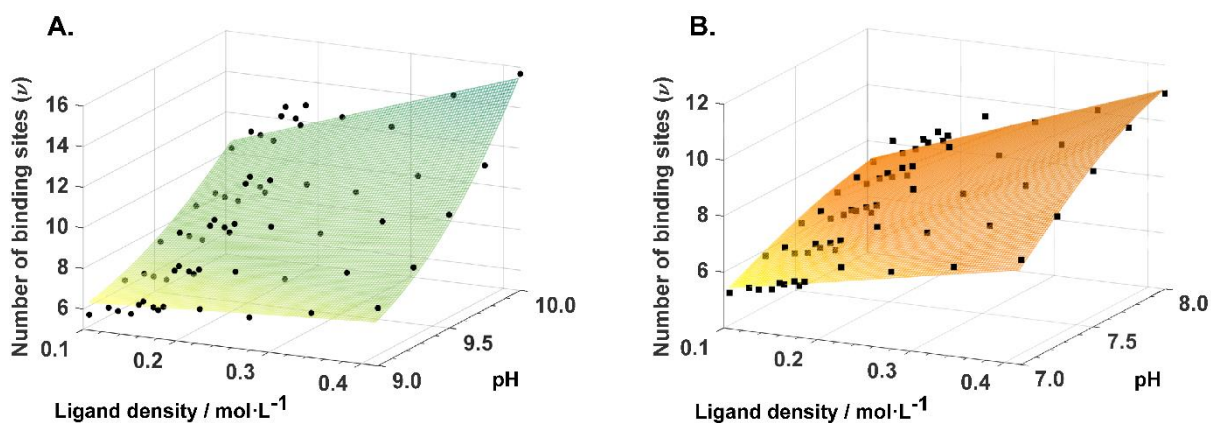


Figure 5. pH and ligand density dependency on the number of binding sites on mAb03 (A, green), and BSA (B, orange) on the strong anion exchange prototypes. Black circles (mAb03) and squares (BSA) represent the data obtained from the fitting of the SD model, while the surface represents the empirical ν_i description proposed in this study.

3.1.2.3 Ligand density dependency of $\Delta\hat{G}_i^0/RT$ and $\Delta\hat{G}_s^0/RT$

According to the results in **Table 13**, the practical Gibbs energy change upon adsorption of the chromatographed component ($\Delta\hat{G}_i^0/RT$) is protein and ligand density-dependent. A slight increase in $\Delta\hat{G}_i^0/RT$ is observed, when the ligand density is increased (**Figure 6.A**). Additionally, the practical Gibbs energy change upon adsorption of the salt counter-ion ($\Delta\hat{G}_s^0/RT$) shows a dependency on the ligand density. A decrease in the standard Gibbs energy for binding of the counter-ion is obtained when the ionic capacity is increased (**Figure 6.B**).

The model parameters obtained from the SD model at different ligand densities are shown in **Figure 6**; the mAb data is represented with circles and BSA is represented with squares. These results (SD model parameters) and the description of the number of binding sites in equation (28) were fitted to equation (23) to determine the ligand density SD model parameters. All fitted parameters are given in **Table 14**. The obtained model parameters for the developed isotherm model show an excellent correlation with the experimental data throughout the whole range of pH and ligand density variation investigated in this work. When using the description of the adsorption isotherm that takes into account the activity coefficient of the protein in the adsorbate state, it is possible to describe the ligand density dependency on both thermodynamic parameters $\Delta\hat{G}_i^0/RT$ and $\Delta\hat{G}_s^0/RT$. This is represented in **Figure 6**; the dash lines depict the prediction using the ligand density SD model for both model proteins.

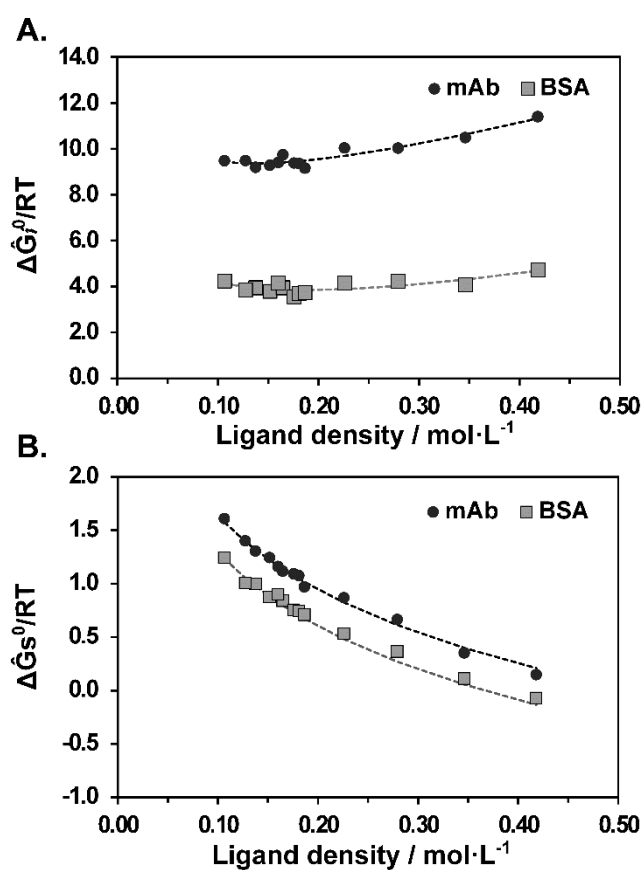


Figure 6. Dependency of the SD model parameters $\Delta\hat{G}_i^0/RT$ (A) and $\Delta\hat{G}_s^0/RT$ (B) of BSA (■) and mAb (●) on the ligand density. The prediction curves using the ligand density SD model parameters are represented by the dashed lines, BSA- grey, and mAb-black.

A small average difference of ~ 0.3 units on both model parameters $\Delta\hat{G}_s^0/RT$ and $\Delta G_p^0/RT$ between the mAb and BSA can be observed (**Table 14**). The ligand density SD model results also show the standard Gibbs energy changes of BSA as a negative value, while the mAb has a positive value (**Table 14**).

Table 14. Fitted model parameters for mAb03 and BSA when applying the ligand density SD model.

Parameter	mAb	BSA
$\Delta G_p^0/RT$	1.97	-2.91
$\Delta G_s^0/RT$	-4.71	-5.03
$A_{1/2}$	24.91	14.98
$A_{2/1}$	-12.39	-7.84
ν_0	5.52	3.39
N_1	7.80	3.05
N_2	35.74	13.33
pKa_i	10.11	7.06

The calculated equilibrium constant for both model proteins using equation (15) and the values in **Table 14** are depicted in **Figure 7**. The mathematical descriptions of the thermodynamic parameters with the ligand density SD model accurately describe the elution of both model proteins in the whole range of pH and ligand density variation investigated in this work. Slight deviations on the equilibrium constant for both proteins can be observed at high pH values. Overall, the model accurately describes the observed equilibrium constant of mAb03 and BSA, and it confirms that when using a proper description of the equilibrium constant, the variation on the ligand density can be characterized.

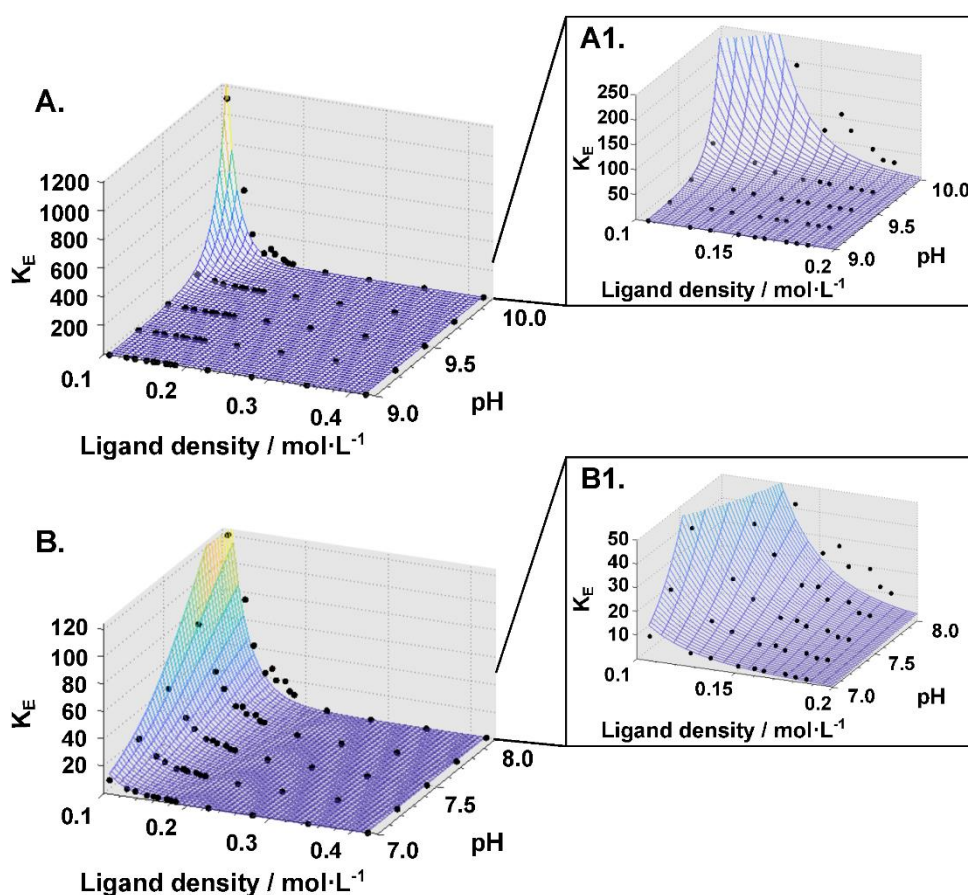


Figure 7. Equilibrium constant (K_E) description of mAb03 (A, top) and BSA (B, bottom), relative to the pH and ligand density. Results of the SD model parameters are represented as black dots and the colorful surface represents the prediction of K_E using the ligand density SD model. For better visibility of the correlation throughout the low ligand density area, a zoom of the graph is illustrated on the right-hand side (A1 and B1).

3.1.2.4 *In silico* validation – Chromatogram simulation of AEX resins

In order to validate the proposed thermodynamic model, the experimental runs were compared to the predicted *in silico* chromatograms. Representative sets of linear-

gradient experiments and corresponding model simulations on the strong anion exchange with the lowest, middle, and highest ligand density are depicted in **Figure 8**. For reasons of clarity, **Figure 8** only shows the *in silico* chromatograms at a gradient column of 40 CV. The verification of the model at 60, 80, and 120 CV for mAb03 and BSA demonstrated a good correlation to the experimentally determined salt LGE experiments (data not shown). The lumped rate model was applied to obtain the *in silico* chromatograms.

The mass transfer coefficients (k_{eff}) were obtained by the reverse fitting of the chromatograms; the results for each salt gradient in the figure are shown in **Table 15**. The model does not contain a description of the pH dependence of the effective film transfer coefficient. Therefore, this parameter was estimated separately for each elution profile.

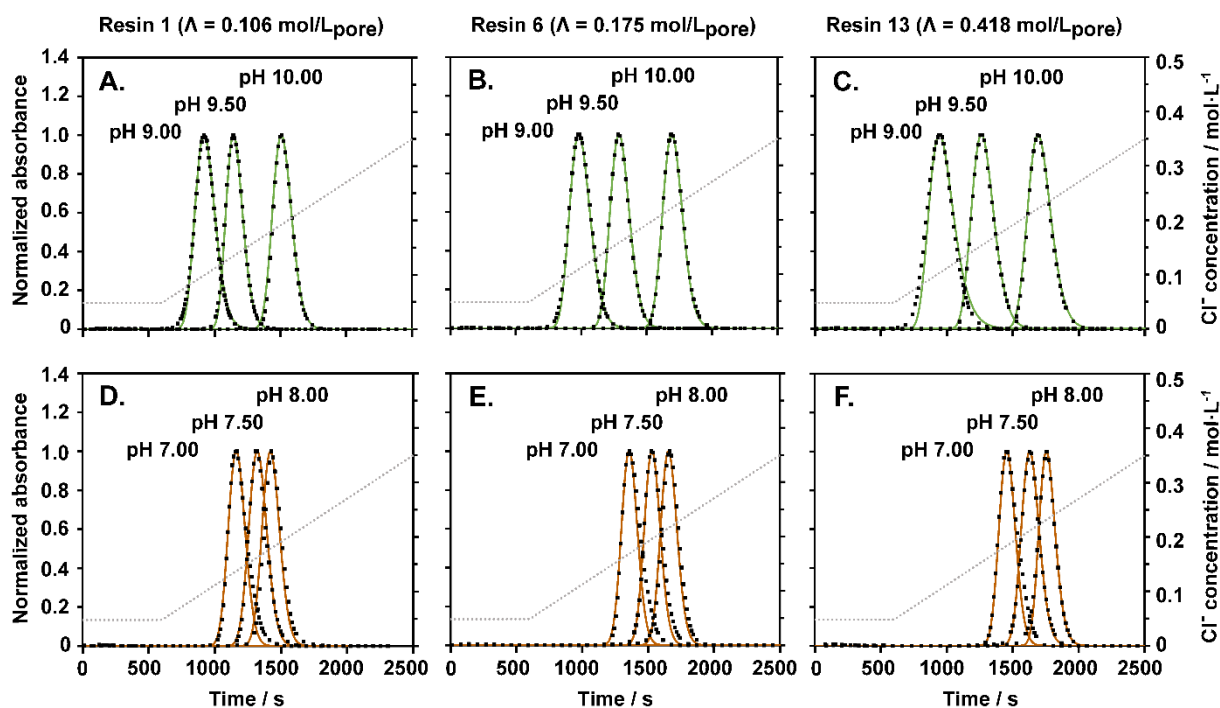


Figure 8. *In silico* chromatograms of salt gradients at different pH values for resin 1 (A and D), resin 6 (B and E), and resin 13 (C and F). Linear salt gradient elution from 0.05 mol/L to 1 mol/L in 40 CV. The gradient experiments for mAb (A-C) were performed at pH 9.0, 9.5, and 10.0. For BSA (D-F), the experiments were performed at pH 7.0, 7.5, and 8.0. Experimental data (black squares) at different pH values are superimposed onto column simulations (mAb-green and BSA-orange solid lines). $D_{ax} = 1.17 \times 10^{-2} \text{ cm}^2/\text{s}$. Flow rate = 1.0 mL/min. Protein load of 1 g/L packed bed.

The results in **Figure 8** show a good correlation between the experimental data and the *in silico* chromatograms. Deviations are observed for BSA on all three resins at pH 7.00 (**Figure 8.D-F**). Under these conditions, a slight broadening of the base peak is

observed and can be explained due to the well-known heterogeneity of BSA (Foster, 1977).

The results of the mass transfer coefficients of the monoclonal antibody on the salt gradients displayed an increase in the k_{eff} values, independent of the ligand density, when the pH is increased. While the increase of the ligand density at a fix pH value showed a decrease of the k_{eff} values. Similar tendencies were observed for BSA on the salt gradients at a fix pH value, where a ligand density increase exhibited a decrease on the k_{eff} values. However, the change in the pH of the mobile phase showed an almost unaffected k_{eff} value for BSA.

Table 15. Estimated effective mass transfer coefficients (k_{eff}) for mAb03 and BSA at low (Res 1), middle (Res 6), and high (Res 13) ligand density.

mAb03 k_{eff} (cm ² ·s ⁻¹)			
pH value	RES 1	RES 6	Res 13
9.00	3.5 × 10 ⁻⁵	3.1 × 10 ⁻⁵	1.3 × 10 ⁻⁵
9.50	7.8 × 10 ⁻⁵	6.2 × 10 ⁻⁵	2.2 × 10 ⁻⁵
10.00	8.5 × 10 ⁻⁵	6.5 × 10 ⁻⁵	2.9 × 10 ⁻⁵
BSA k_{eff} (cm ² ·s ⁻¹)			
pH value	RES 1	RES 6	Res 13
7.00	6.3 × 10 ⁻⁵	5.9 × 10 ⁻⁵	4.1 × 10 ⁻⁵
7.50	5.9 × 10 ⁻⁵	5.8 × 10 ⁻⁵	3.5 × 10 ⁻⁵
8.00	6.0 × 10 ⁻⁵	5.9 × 10 ⁻⁵	3.1 × 10 ⁻⁵

Additionally, to prove the reliability of the model, dual gradient experiments were simulated and experimentally verified. The dual gradient elution of mAb03 and BSA was successfully predicted using the obtained model parameters determined from the salt gradient experiments, which demonstrates the transferability between pH and salt gradient experiments. The results for the lowest and the highest ligand density are displayed in **Figure 9**. Once more, the heterogeneity of BSA can be visualized on the separation of the dual gradient runs. This outcome reflects the susceptibility of BSA isoforms to pH and salt changes. Nonetheless, a good correlation between the *in silico* chromatograms and the experimentally obtained UV curves is observed.

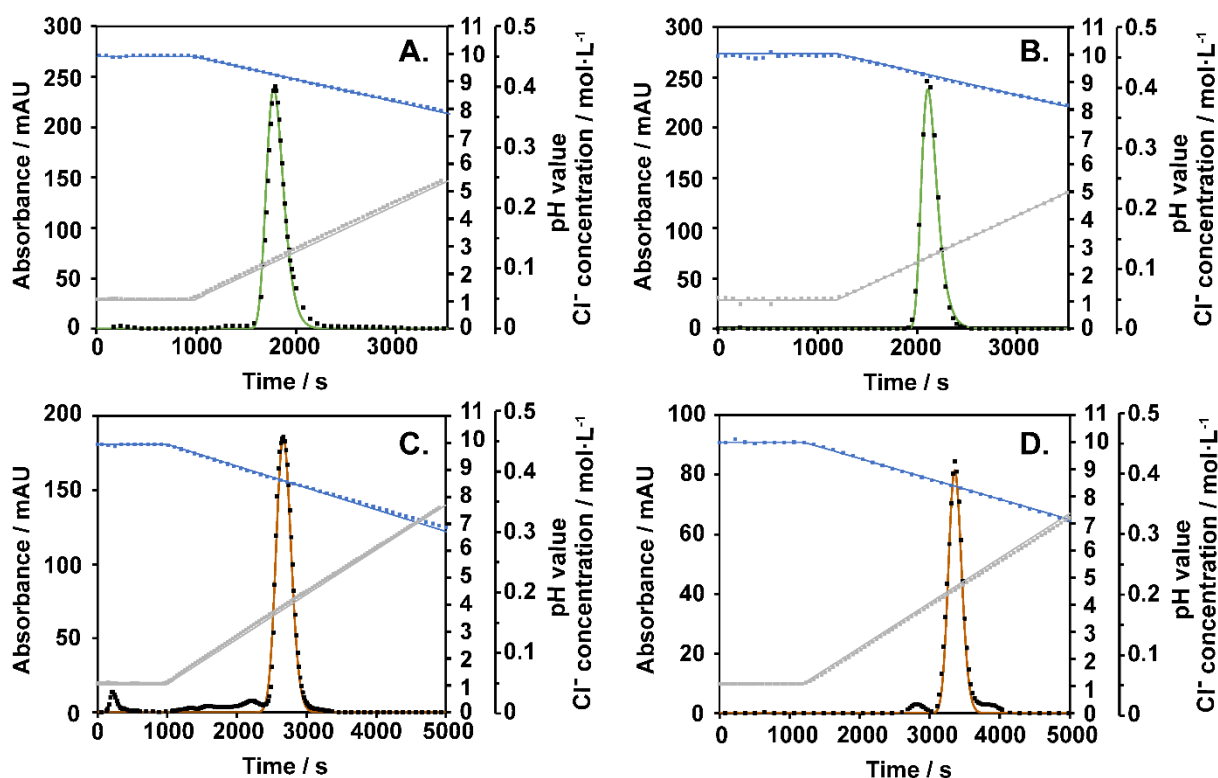


Figure 9. *In silico* chromatograms of a dual gradient from pH 10.0 to 5.0 and a chloride concentration of 0.05 mol/L to 0.5 mol/L in 40 CV for resin 1 (A, C) and 13 (B, D) of mAb (A-B) and BSA (C-D). Experimental data (black squares) and simulations (solid lines) of UV signal (mAb-green and BSA-orange), chloride concentration (gray) and pH (blue). $D_{ax} = 1.17 \times 10^{-2} \text{ cm}^2/\text{s}$. $k_{eff, mAb} = 1.29 \times 10^{-5} \text{ cm}^2/\text{s}$. $k_{eff, BSA} = 3.11 \times 10^{-5} \text{ cm}^2/\text{s}$. Flow rate = 1.0 mL/min. mAb03 load of 1 g/L packed bed (A-B). BSA load of 2 and 1 g/L packed bed (C-D), respectively.

3.1.2.5 Ligand density dependency of the characteristic charge (ν_i) – a Donnan equilibrium in ion exchange chromatography

In the present work, the modeling of the ligand density dependency on the ν_i values were achieved by introducing an empirical model (Eq. (28)). The description allows the prediction of the binding charge of the proteins but does not give any physico-chemical explanation for this effect.

The introduction of the Donnan ratio (r_D) (Eq. (30)) allows the estimation of the counterion concentration in both phases, as well as the calculation of the intraparticle pH (Eq. (31)). **Figure 10** shows the characteristic charge for mAb and BSA (**Figure 10.A** and **Figure 10.B**, respectively) against the r_D values and the pH in the mobile phase, where the different ligand densities of the resins are depicted with colorful dots; yellow represents the lower ligand density and the increase in hue illustrates an increase in ligand density (mAb-green and BSA-orange). As previously shown, an increase in the pH of the mobile phase reflects an increase in the number of binding sites. Additionally,

in **Figure 10**, the correlation of v_i on the intraparticle conditions of the pore volume can be observed.

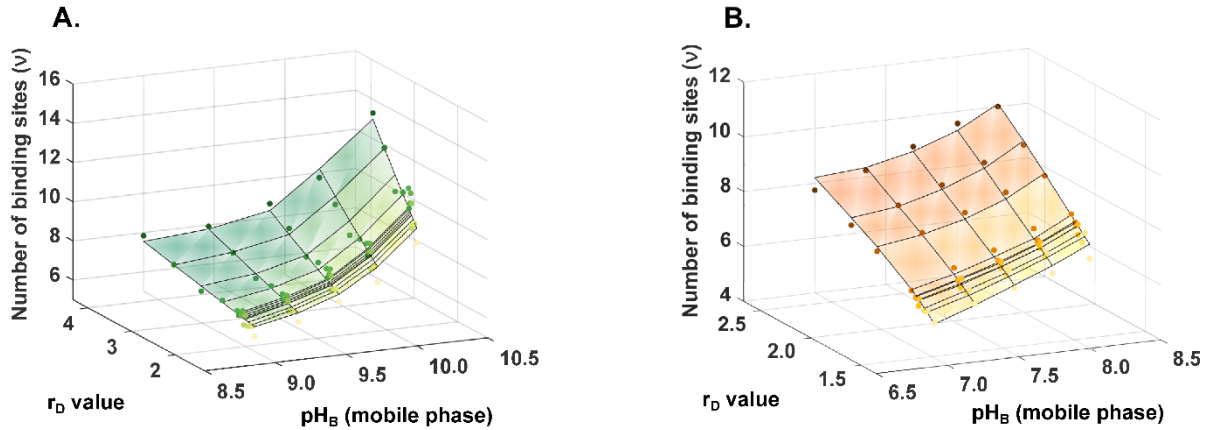


Figure 10. The number of binding sites in relation to the calculated r_D value and the pH in the mobile phase (pH_B). mAb03 (A) and BSA (B) are depicted in a shade of green and orange, respectively. Being the light yellow dots, the lowest ligand density and an increase in hue represent an increase in ligand density. While the surface represents the proposed v_i description in Eq. (44), and the fit results are shown in **Table 16**.

To describe the observed dependencies of the characteristic charge, involving the interactions between the protein and the intraparticle conditions described by the Donnan ratio, the r_D in the resin (Eq. (30)) was introduced to the protein net charge model for v_i (Schmidt et al., 2014). The proposed v_i description is given by:

$$v_i = \frac{N_{D,1}}{1 + 10^{(pKa_{D,1} - [pH_B + \theta_i \cdot \log(r_D)])}} + \frac{N_{D,2}}{1 + 10^{(pKa_{D,2} - [pH_B + \theta_i \cdot \log(r_D)])}} \quad (44)$$

As shown in **Figure 10**, the proposed v_i description is able to describe the dependency on intraparticle conditions and pH of the mobile phase for both proteins with the distinction of two ionizable groups. The green (mAb) and orange (BSA) surface depicted in the picture represents the fit of Eq. (44). All fitted parameters are given in **Table 16**.

The θ_i factors are needed to describe both proteins, showing that the value for the mAb is close to 1 and for BSA is above 1. For a θ_i factor of 1, $[pH_B + \theta_i \cdot \log(r_D)]$ is equal to the Donnan model pH_{resin}^θ (Eq. (31)), otherwise $pH_{resin}^\theta = pH_B + \theta_i \cdot \log(r_D)$.

Table 16. Fitted model parameters for mAb03 and BSA applying the v description that takes into account the Donnan equilibrium.

Parameter	mAb03	BSA
$N_{D,1}$	5.93	6.99
$pKa_{D,1}$	8.35	7.22
$N_{D,2}$	43.85	7.09
$pKa_{D,2}$	11.01	9.19
θ_i	1.13	3.78

Additional evidence on the influence of the ligand density on the intraparticle conditions is indicated by plotting the number of binding sites against the protein-specific pH_{resin}^{θ} as shown in **Figure 11**. The increase in the number of binding sites can be described solely by the changes in the pH of the resin phase.

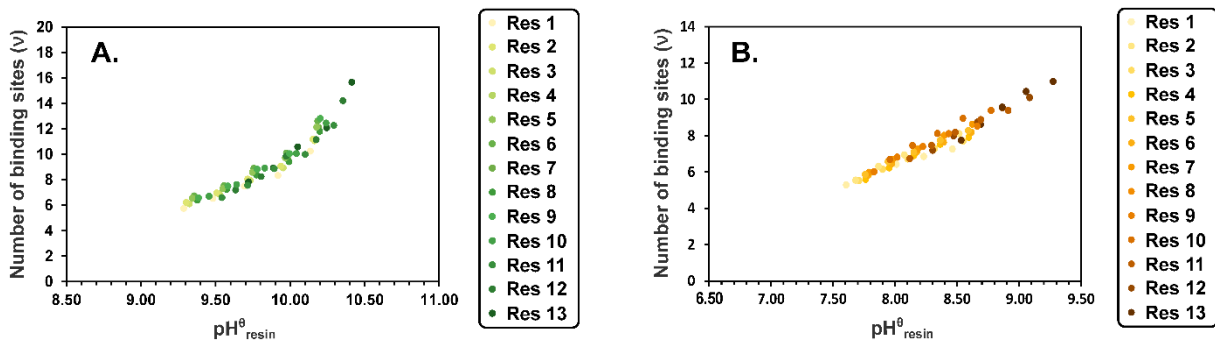


Figure 11. The number of binding sites in relation to the calculated intraparticle pH in the resin phase (pH_{resin}^{θ}). mAb (A) and BSA (B) are depicted in a shade of green and orange, respectively. Being the light yellow dots, the lowest ligand density, and an increase in hue represent an increase in ligand density.

An additional effect can be observed when a $\theta_i = 1$ is applied to BSA, as shown in **Figure 12**. The results of $\theta_{BSA} = 1$, reflects a partition of the data points with a ligand density above 200 mmol/L_{pore}. The partition showing a higher number of binding sites indicates the elution of the protein above 0.30 mol/L Cl⁻ concentration. A clear difference in the dependencies of mAb03 and BSA with the characteristic charge is observed.

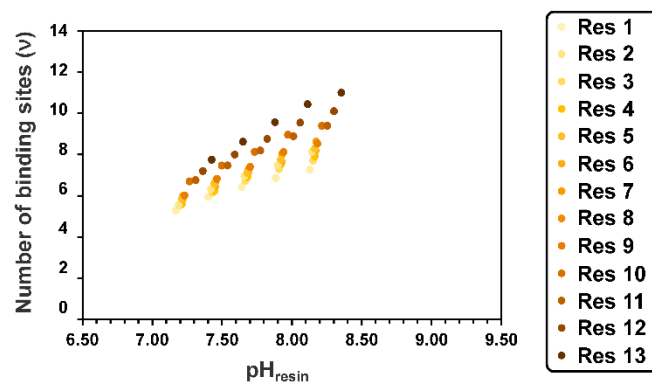


Figure 12. The number of binding sites in relation to the calculated intraparticle pH ($\theta = 1.0$) in the resin phase for BSA. The different ligand density is depicted in a shade of orange, being the light yellow dots, the lowest ligand density, and an increase in hue represents an increase in ligand density.

3.2 Modeling of cation exchange resins

3.2.1 Purification of mAb04 charge variants

The high portion of charge variants in the mAb04 sample makes this protein remarkable. To study this unique characteristic, the separation of the charge variants was crucial. The isolated samples will allow investigating the influence of each variant separately in the modeling runs. In the following chapters (section 3.2.1.1 and 3.2.1.2), the charge variants' characterization and purification will be discussed.

3.2.1.1 Characterization of mAb04

The monoclonal antibody (mAb04) sample was obtained from the company Boehringer Ingelheim (Biberach, Germany). The characterization of the purified Protein A elution sample of mAb04 was done with SEC-HPLC and CEX-HPLC, as described in section 2.8 and 2.9, respectively. The two techniques give information on the size of the molecules and the charge isoforms of the mAb04 sample.

The results in **Figure 13.A** shows the SEC-HPLC analysis of mAb04. Here the elution takes place in two peaks; a peak with high molecular height species (HMW) at 7.6 mL of the elution volume and a monomer peak at 8.5 mL of the elution volume. The HMW species accounts for 6.0 % of the total peak area, while the monomer accounts for 94.0 % of the sample.

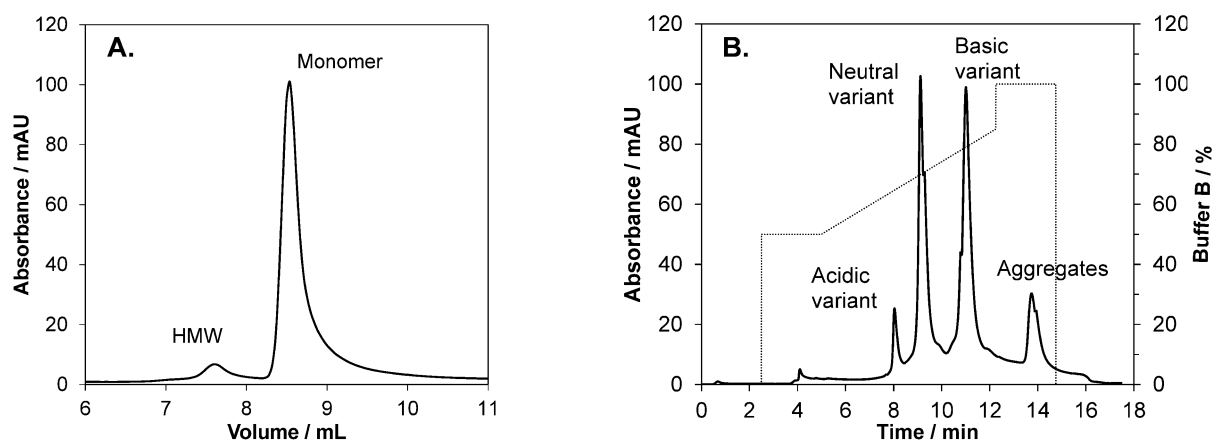


Figure 13. SEC-HPLC (A) and CEX-HPLC (B) analysis of the mAb04 sample. The SEC-HPLC analysis was performed with a Phenomenex® BioSep-SEC-S3000 column with a flow rate of 1 mL/min and a protein load of 100 μ L. The CEX-HPLC analysis was performed with a BioPro™ SP-F column with a flow rate of 0.83 mL/min and a protein load of 1 mg/mL_{Cv}.

The CEX-HPLC analysis of mAb04 is depicted in **Figure 13.B**. By the application of a pH gradient from pH 5.0 to 10.5, the separation of the charge variants was achieved. Here, the elution takes place in 4 main peaks, the first peak inside the gradient was designated as the acidic variant, the second peak was identified as the neutral variant, and the third peak as the basic variant. While the peak eluting at a high pH value was identified as the HMW species present in the sample.

3.2.1.2 Preparative cation exchange

The purification of the charge variants from mAb04 was achieved with a step elution (as described in section 2.5.3) with a binding buffer of pH 4.75 and an elution buffer of pH 10.50 at a fixed concentration of 0.054 mol/L Na⁺ ions. A summary of the steps performed to isolate the mAb04 charge variants is shown in **Figure 14**.

The preparative CEX purification run showed a good separation of the charge variants and the HMW species (**Figure 14.A**). To get a better understanding of the separation quality, the elution volume during the steps was fractionated, as shown by the black line with red termini in **Figure 14.A**. The individual fractions were analyzed by CEX-HPLC to determine the distribution of the individual charge variants in the collected fractions, as seen in **Figure 14.B**. The preparative CEX run was repeated several times in order to obtain sufficient material for subsequent investigations.

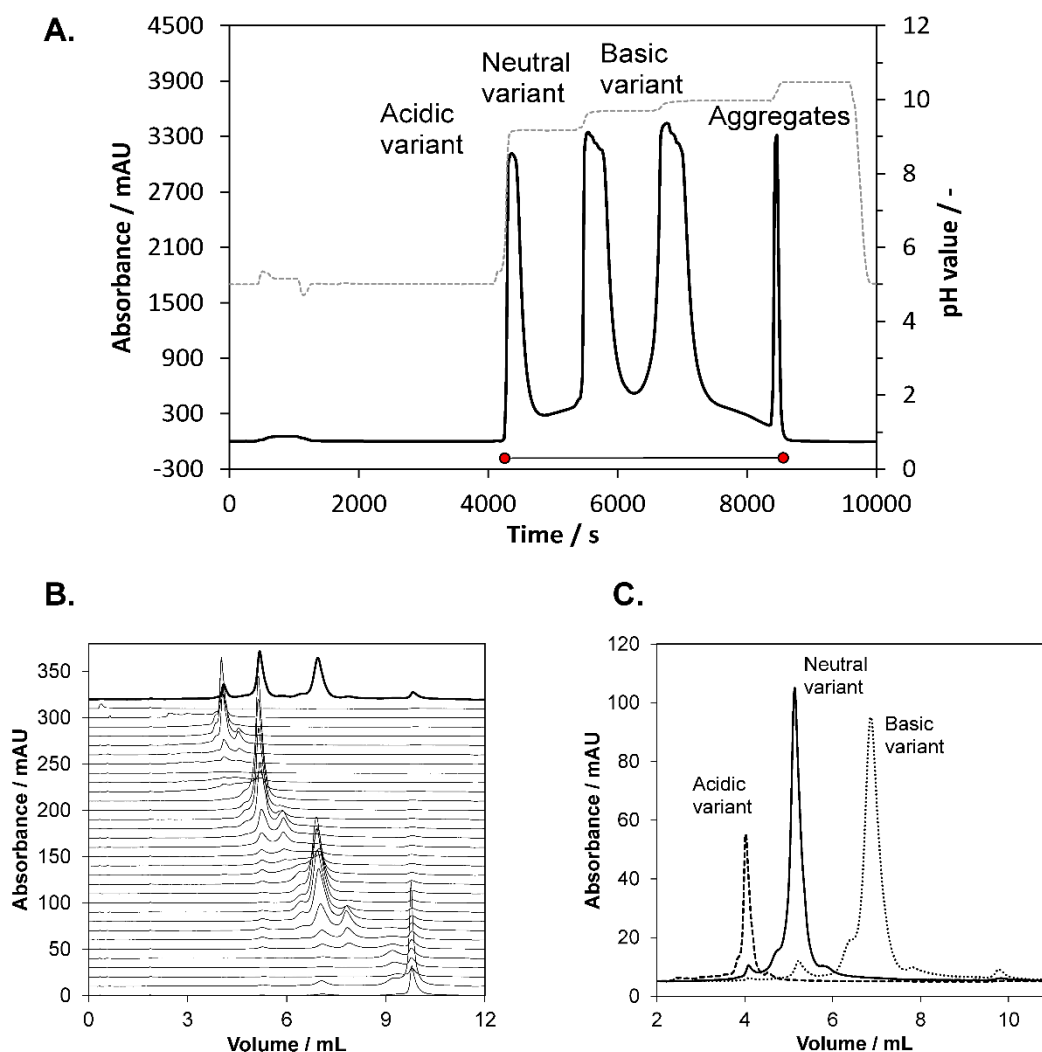


Figure 14. Experimental outline: Purification of mAb04 charge variants. (A) Step elution preparative CEX for the separation of the charge variants with UV signal at 280 nm (—), pH trace (---), and fractionated volume (●●). (B) CEX-HPLC analysis of the preparative CEX fractions. (C) CEX-HPLC analysis of the pooled fractions.

Based on the CEX-HPLC analysis, fractions containing the individual charge variants were pooled to create one sample with each main variant. The pooled fractions were re-analyzed to calculate the purity of the sample. The analysis showed that the individual pools are enriched in the acidic, neutral, and basic variants compared to the original sample (**Figure 14.C**). The acidic variant analysis showed a purity of 92.0 %, with only the neutral variant as an impurity. On the other hand, the neutral variant showed a purity of 87.0 %, with the acidic and basic variant as the main impurities (6.2 % and 5.3 %, respectively), and a small percentage of HMW species (1.4 %). While the basic variant showed a purity of 78.3 %, being the HMW species and the neutral

variant as the main impurities. The enriched charge variant samples were used to investigate the influence of the ligand density on cation exchange chromatography.

3.2.2 CEX column parameters

3.2.2.1 Dead volumes of the Äkta system

To determine the column parameters is imperative to account for the dead volumes of the chromatographic system. The determination of the Äkta Purifier 10, where the experiments for the mAb04 charge variants were carried out, yielded a dead volume of 0.12 mL between the UV signal measurement and the conductivity cell. This value was used to adjust all the retention values read-outs coming from the UV signal. At the same time, the read-outs from the pH signal were adjusted with 0.25 mL.

3.2.2.2 Porosities and ligand density

Different conditions for the determination of the porosities in the cation exchange resins were tested. First, the influence of the mobile pH was investigated. As shown in **Figure 15.A**, no influence in the retention of the compound was observed at the evaluated pH values. Subsequently, the influence of NaCl concentration was tested at a fixed pH value (**Figure 15.B**). The results show a strong shift in retention when the salt concentration is increased, as well as a change in the peak shape.

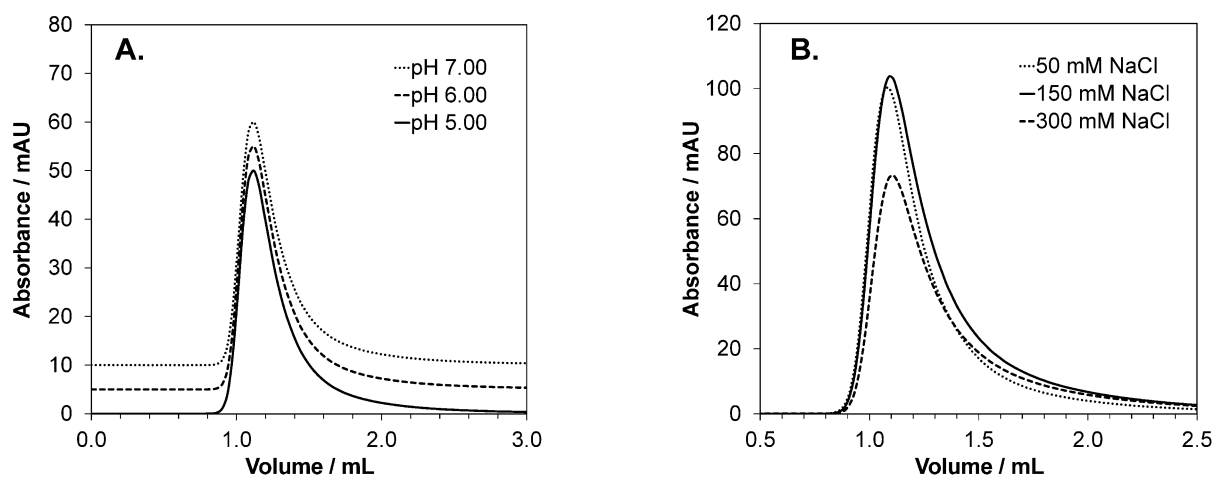


Figure 15. Porosity determination at different conditions in Resin 1. (A) Retention of dextran blue at different pH values: 5.00, 6.00 and 7.00. (B) Retention of dextran blue at pH 6.00 at different salt concentrations: 0.05 mol/L, 0.15 mol/L and 0.30 mol/L.

The porosity results obtained with a low salt concentration and pH 6.0 were used for further determination and evaluation. **Table 17** shows the experimentally measured values for the total porosity (ϵ_t), interstitial porosity (ϵ) and the intraparticle porosity (ϵ_p)

obtained from the injection of dextran blue on all five prototype resins. Examining the values for the total porosity (ε_t) and the intraparticle porosity (ε_p), a decrease is observed when the ligand density is increased. The interstitial porosity (ε) on the other hand, shows a very consistent value independent of the ligand density variation.

Table 17: Determined porosities and ionic capacity of thirteen strong cation exchange prototype resins.

Fractogel® EMD SO₃⁻ (M) prototypes:

Resin ID ^{a)}	Λ_{packed} ($\mu\text{eq}\cdot\text{mL}^{-1}$)	ε	ε_t	ε_p	$\Lambda_{\text{pore}}^{\text{b)}$ ($\text{mmol}\cdot\text{L}_{\text{pore}}^{-1}$)
RES 1	82.94	0.347 ± 0.002	0.779 ± 0.009	0.661	202.3
RES 2	103.29	0.351 ± 0.003	0.774 ± 0.003	0.652	251.9
RES 3	113.65	0.347 ± 0.000	0.760 ± 0.007	0.632	277.2
RES 4	128.94	0.337 ± 0.001	0.741 ± 0.009	0.610	314.5
RES 5	151.76	0.347 ± 0.088	0.737 ± 0.007	0.598	370.1

^{a)} sorted by Λ_{pore} in ascending order.

^{b)} calculated from the Λ_{packed} according to Eq. (42) with $\varepsilon = 0.35$ and $\varepsilon_t = 0.76$.

As discussed previously, the uncertainty on the porosity measurement led to a simplification on the interstitial porosity ε and the total porosity ε_t . These two values were estimated as 0.35 and 0.76, respectively. At last, the ligand density in the pore volume was calculated with equation (42) and the implementation of the estimated porosities for the CEX resins ($\varepsilon = 0.35$ and $\varepsilon_t = 0.76$).

3.2.2.3 Exclusion factor

The elution volume of a size excluded compound under non-binding conditions is used to determine the exclusion factor ($k_{d,i}$) of the acidic, neutral and basic variant of mAb04. **Table 18** shows the determined values for the charge variants of mAb04 in the five strong cation exchange prototype resins using the methods described in section 2.7.3.

The results in **Table 18** indicate that independent of the charge variant, a significant decrease in the $k_{d,i}$ value is observed when the ligand density is increased.

Table 18: Determined exclusion factors of the acidic (V1), neutral (V2), and basic (V3) variants of mAb04 on five strong cation exchange prototype resins.

Fractogel® EMD SO₃⁻ (M) prototypes:

Resin ID	$k_{d,V1}$ (Acidic variant)	$k_{d,V2}$ (Neutral variant)	$k_{d,V3}$ (Basic variant)	$k_{d,average}$
RES 1	0.360 ± 0.001	0.350 ± 0.005	0.345 ± 0.002	0.35
RES 2	0.292 ± 0.001	0.278 ± 0.002	0.281 ± 0.003	0.28
RES 3	0.249 ± 0.003	0.243 ± 0.003	0.235 ± 0.002	0.24
RES 4	0.230 ± 0.007	0.228 ± 0.003	0.224 ± 0.001	0.23
RES 5	0.144 ± 0.003	0.140 ± 0.001	0.134 ± 0.003	0.14

On the other hand, the variability detected between the charge variants at a fixed prototype resin is minimal. The range of the difference obtained on the mAb04 charge variants' exclusion factor is equal to 0.015 or lower. As the ligand density increases, the differences in the variability of the charge variants become less pronounced. Therefore, a protein independent $k_{d,i}$ value was implemented in the mechanistic modeling of the mAb04 charge variants.

3.2.2.4 Axial dispersion coefficient

The influence of the ligand density on the axial dispersion coefficient (D_{ax}) was investigated, as described in section 2.7.5. The measured values at different volumetric flow rates are displayed in **Figure 16**. Such experiments were performed equally in five strong cation exchange prototype resins with varying ligand densities at six different flow rates. The volumetric flow rates used were 0.5, 0.75, 1.0, 1.25, 1.5 and 1.67 mL/min (the linear flow rate is equal to 59.7, 89.5, 119.4, 149.2, 179.0, 199.3 cm/h, respectively).

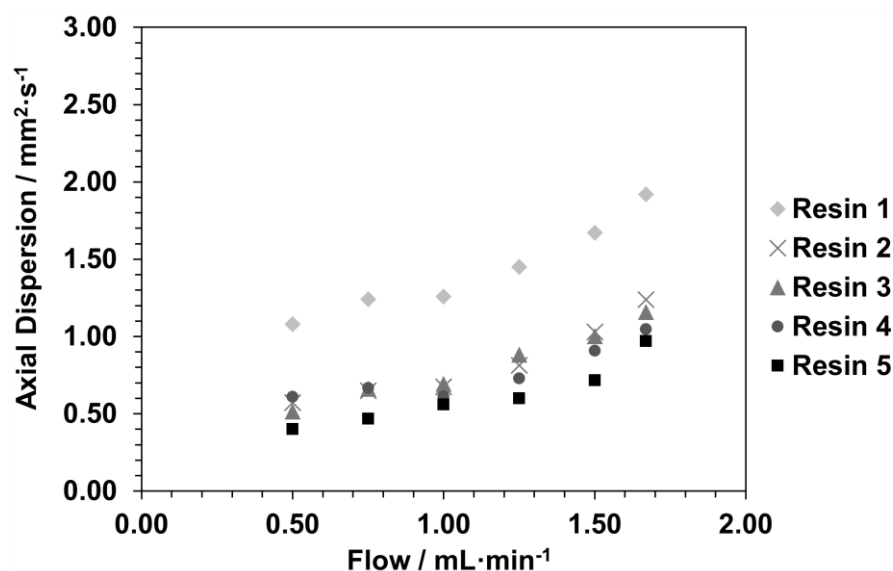


Figure 16. Axial dispersion coefficient in relation to the volumetric flow rate of five strong cation exchange prototype resins.

The results in **Figure 16** indicate that independent of the resin used, the D_{ax} value increases as the volumetric flow rate are increased, displaying a non-linear increase. Additionally, the figure shows the difference between the resins with ligand density variation. The measured D_{ax} values for the prototype resin 1 are considerably higher than the rest of the ligand density prototypes used in this work. While the values for resin 2, resin 3, resin 4, and resin 5 display a high similarity. Overall, a trend can be observed; as the ligand density increases the D_{ax} value decreases.

3.2.3 Linear gradient elution experiments

The influence on the variation of ligand density, as well as the pH and counter-ion concentration on the performance of cation exchange resins, will be investigated in this work. A mathematical model developed by Yamamoto et al., describing protein elution in linear salt gradients (S. Yamamoto et al., 1983) and later applied to pH gradients (Klutets et al., 2016) was implemented to answer this question.

3.2.3.1 Salt gradient elution of mAb04 charge variants

The influence of ligand density variation on the elution behavior of mAb04 charge variants was investigated by the application of linear salt gradients at different pH values on five prototype resins. The symbols in **Figure 17** depict the experimentally determined eluting sodium concentrations for the model proteins, where circles represent the mAb04 acidic variant, the neutral variant is represented with squares and the basic variant with triangles. This series of experiments were performed at pH

values of 7.0, 7.5, and 8.0 for the acidic and basic variants. For the neutral variant, the experiments were performed at pH values of 7.5 and 8.0. While the change in pH is represented in the figure with a shade of gray. By increasing the pH value in the mobile phase, the counter-ion elution concentration of all proteins decreases. In this figure, it can be observed the disparity in the elution behavior of the proteins on the Fractogel® EMD SO₃⁻ (M) prototypes from the lowest to the highest ligand density (top to bottom). Noticeably, the eluting salt (sodium ion) concentration of all proteins is shifted to higher counter-ion concentrations when the ligand density is increased. It is important to mention that all salt LGE experiments were obtained in the linear range of the adsorption isotherm.

3.2.3.2 pH gradient elution of mAb04 charge variants

The application of linear pH gradients at different Na⁺ concentrations on five prototype resins was used to investigate the influence of ligand density variation on mAb04 charge variants' elution behavior. The symbols in **Figure 18**, **Figure 19**, and **Figure 20** depict the experimentally determined eluting pH values for the mAb04 acidic, neutral, and basic variants, respectively. This series of experiments were performed at sodium concentrations of 0.10, 0.125, 0.15, 0.175 and 0.20 mol/L. By increasing the counter-ion concentration in the mobile phase, the pH elution values of all model proteins decrease. In these figures, it can be observed the disparity in the elution behavior of the proteins on the Fractogel® EMD SO₃⁻ (M) prototypes from the lowest to the highest ligand density (top to bottom). Remarkably, the eluting pH values of all proteins is shifted to higher pH values when the ligand density is increased. It is important to point out that all pH LGE experiments were obtained in the linear range of the adsorption isotherm.

3.2.3.3 Stoichiometric displacement model

The implementation of the SD model was done to have a better understanding of the effect of the ligand density variation in cation exchange chromatography. This was accomplished by the use of the experimental salt gradient elution data from all three charge variants. The correlation of the experimental gradient elution data at different pH values, according to Eq. (5) and (6), is displayed in **Figure 17**. The predicted curves, represented by the straight lines in the figure, are described by the model parameters; $\Delta\hat{G}_i^0/RT$, $\Delta\hat{G}_s^0/RT$ and the number of binding sites (ν_i). **Table 19** shows a summary of the fitted parameters for the five ligand density prototype resins and the

mAb04 charge variants. The graphic representation of the $\Delta\hat{G}_i^0/RT$ and $\Delta\hat{G}_s^0/RT$ model parameters can be found in **Figure 21**.

Table 19: Fitted model parameters $\Delta\hat{G}_i^0/RT$, $\Delta\hat{G}_s^0/RT$, and v_i when using the SD model for the acidic, neutral, and basic variant of mAb04 on five strong cation exchange prototype resins.

mAb04 acidic variant						
		RES 1	RES 2	RES 3	RES 4	RES 5
	$\Delta\hat{G}_i^0/RT$	15.62	15.41	15.21	14.93	14.55
	$\Delta\hat{G}_s^0/RT$	2.63	2.52	2.43	2.30	2.14
pH 7.00	v_i	6.47	6.55	6.53	6.47	6.51
pH 7.50	v_i	5.93	5.96	5.95	5.89	5.92
pH 8.00	v_i	5.15	5.20	5.20	5.12	5.15
mAb04 neutral variant						
		RES 1	RES 2	RES 3	RES 4	RES 5
	$\Delta\hat{G}_i^0/RT$	18.28	18.01	17.87	17.73	17.43
	$\Delta\hat{G}_s^0/RT$	3.36	3.13	3.01	2.92	2.74
pH 7.50	v_i	6.23	6.29	6.34	6.31	6.40
pH 8.00	v_i	5.69	5.73	5.76	5.75	5.80
mAb04 basic variant						
		RES 1	RES 2	RES 3	RES 4	RES 5
	$\Delta\hat{G}_i^0/RT$	17.40	17.01	16.18	16.61	16.30
	$\Delta\hat{G}_s^0/RT$	2.84	2.62	2.52	2.40	2.25
pH 7.00	v_i	7.32	7.34	7.14	7.28	7.35
pH 7.50	v_i	6.92	6.96	6.75	6.92	6.95
pH 8.00	v_i	6.49	6.51	6.32	6.48	6.50

The model parameters determined with the SD model showed that independent of the charge variant, a decrease in the $\Delta\hat{G}_s^0/RT$ is observed when the ligand density is increased. A small difference between the charge variants is detected when focusing on the individual $\Delta\hat{G}_s^0/RT$ values. The largest variation is observed in the prototype resin 1 with 0.21 units difference between the acidic and basic variants. The difference of the charge variants on all other resins is 0.1 or less. Additionally, the $\Delta\hat{G}_i^0/RT$

parameter exhibits divergence in the values for the acidic, neutral and basic variant, showing that this parameter is protein-dependent. And when focusing on the individual $\Delta\hat{G}_i^0/RT$ values a slight increase in the model parameter is detected once the ligand density is increased.

The number of binding sites (ν_i) decreases with increasing pH for the acidic, neutral, and basic variants of mAb04. On the other hand, at a fixed pH, the number of binding sites remains almost unaffected by the increase in ligand density. It is worth noting that the basic variant's characteristic charge is greater than the characteristic charge of the acidic and neutral variant under all investigated conditions. Furthermore, the neutral variant's characteristic charge is greater than the characteristic charge of the acidic variant under all investigated conditions.

Overall, the curve fitting results (**Figure 17**) showed that the predicted normalized gradient slope data is in good agreement with the experimental data when applying the SD model.

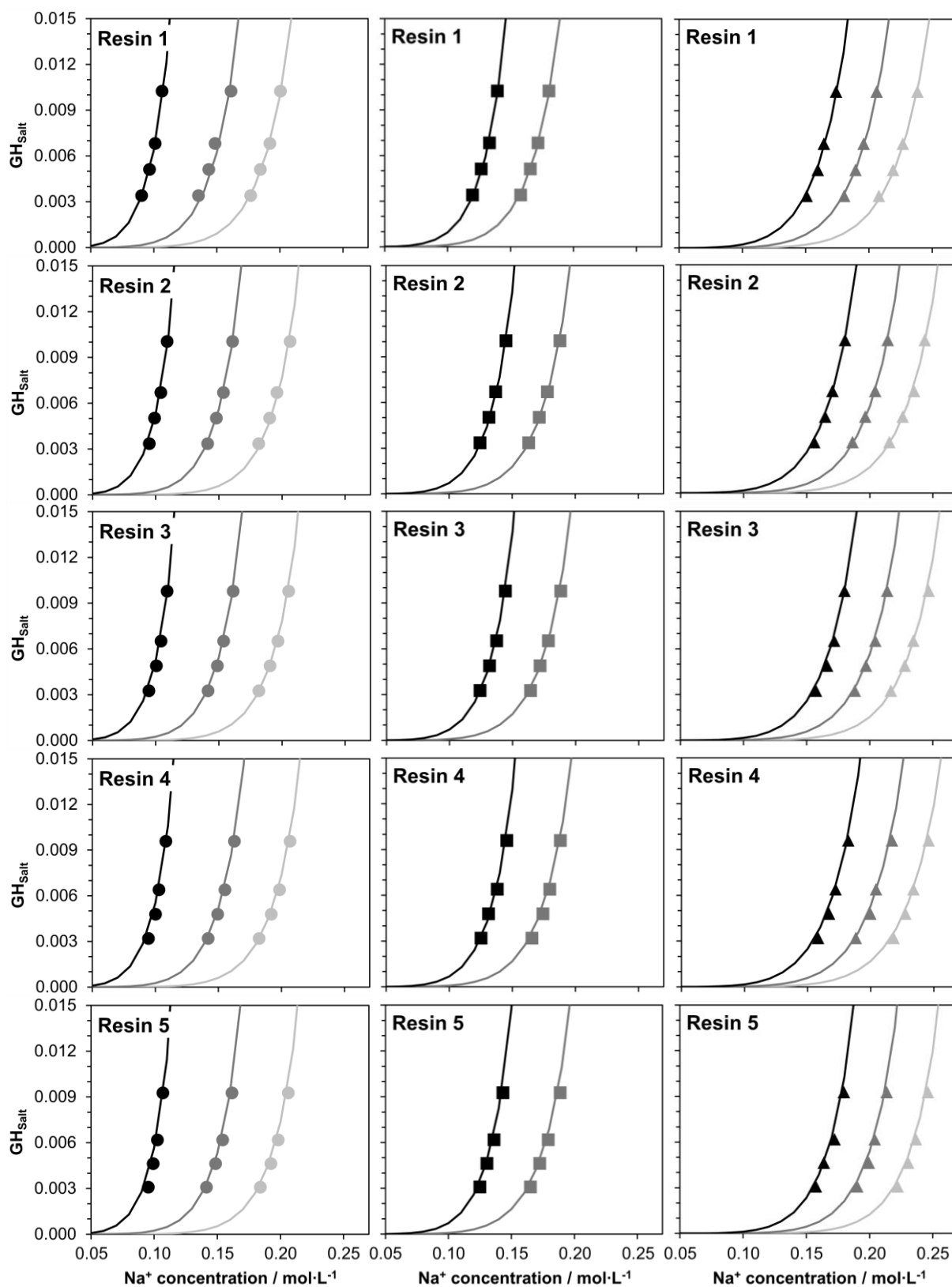


Figure 17. Eluting Na^+ concentrations of the acidic (circles and lines), neutral (squares and lines), and basic variant (triangles and lines) of mAb04 as a function of the normalized salt gradient slope (GH_{salt}) on resin 1, 2, 3, 4, and 5. The experiments were performed at pH values of 7.0 ($\bullet \blacktriangle$), 7.5 ($\bullet \blacksquare \blacktriangle$), and 8.0 ($\bullet \blacksquare \blacktriangle$). Straight lines depict the fitting result with the SD model, whereas the symbols represent the experimental data obtained from the LGE runs.

3.2.3.4 Ligand density model based on a stoichiometric displacement

The transferability of the proposed thermodynamic model developed from the anion exchange resins was investigated using the LGE experiments of the mAb04 charge variants on the cation exchange prototype resins.

The ligand density SD model parameters obtained for each charge variant are summarized in **Table 20**. According to Eq. (23) and (29), the correlation of the experimental gradient elution data is illustrated in **Figure 18** for the acidic variant, **Figure 19** for the neutral variant, and **Figure 20** for the basic variant. The characteristic charge description was modeled using a protein net charge model (29), and it was implemented with three ionizable groups to cover the wide range of pH values in the dataset. It is important to mention that the $pK_{a_{AA}}$ values for the different amino acids were not fixed, but rather included in the fitting parameters.

Table 20: Fitted model parameters for the acidic, neutral, and basic variant of mAb04, when applying the ligand density SD model and the proposed description of the characteristic charge.

Parameter	Acidic variant	Neutral variant	Basic variant
$\Delta G_i^0/RT$	11.04	10.82	12.39
$\Delta G_s^0/RT$	-2.87	-2.79	-2.76
$A_{1/2}$	9.37	0.04	12.65
$A_{2/1}$	2.85	5.47	1.50
$pK_{a_{carb}}$	4.37	4.54	4.80
$pK_{a_{amine}}$	9.01	9.51	10.87
$pK_{a_{n-term}}$	6.82	7.15	7.86
N_{carb}	2.48	3.18	8.91
N_{amine}	8.42	9.10	14.75
N_{n-term}	1.44	1.46	1.56

The obtained model parameters for the developed isotherm model show an excellent correlation with the experimental data throughout the whole range of pH and ligand density variation investigated in this work. When using the description of the adsorption isotherm that takes into account the activity coefficient of the protein in the adsorbate state, it is possible to describe the ligand density dependency on both thermodynamic

parameters $\Delta\hat{G}_i^0/RT$, and, $\Delta\hat{G}_s^0/RT$. This is represented in **Figure 21**; the dash lines depict the prediction using the ligand density SD adsorption isotherm for each model protein.

According to the results in **Table 20**, the standard Gibbs energy for binding of the counter-ion, the thermodynamic $\Delta G_s^0/RT$ parameter is protein and ligand density-independent. The acidic, neutral and basic variant $\Delta G_s^0/RT$ values lie in the same range, showing a small difference between the proteins of 0.1 or less. While the standard Gibbs energy changes of the protein, the thermodynamic $\Delta G_p^0/RT$ parameter displays protein dependent values, but ligand density independency.

The values for the activity coefficients representing the molecular interaction parameters between the species present in a binary mixture show no visible trend between the charge variants of mAb04. The $A_{1/2}$ parameter displays the lowest value for the neutral variant, followed by the acidic variant, and the highest value is reached by the basic variant. And the opposite tendency is observed by the $A_{2/1}$ parameter, where the highest value is displayed by the neutral variant, and the lowest value is attained by the basic variant. The extremely low value in the $A_{1/2}$ parameter for the neutral variant is responsible for the slight slope difference observed in **Figure 21** when comparing to the acidic and basic variants.

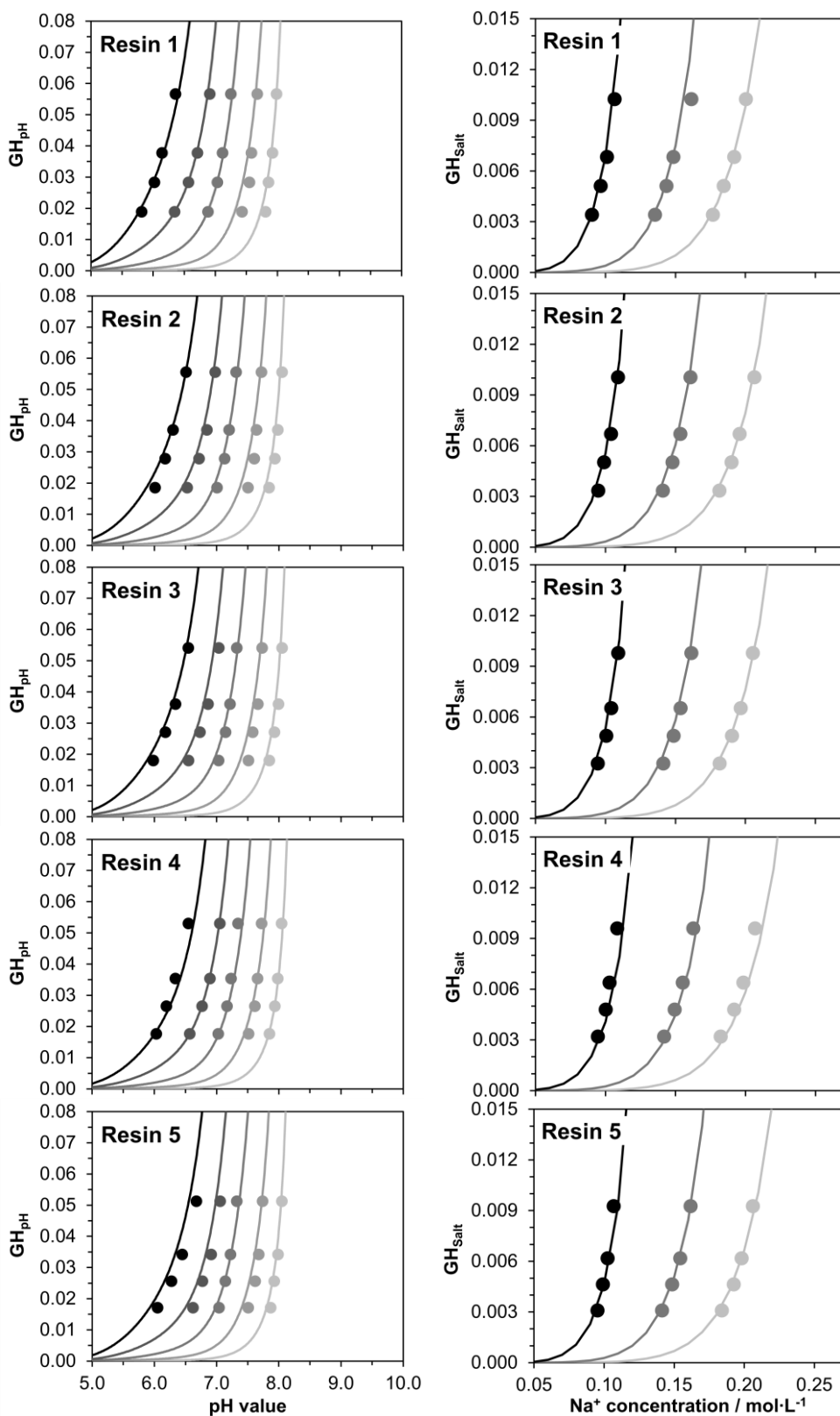


Figure 18. Eluting pH and Na^+ concentrations of the acidic variant (circles and lines) of mAb04 as a function of the normalized gradient slope ($GH_{pH/salt}$) on resin 1, 2, 3, 4 and 5. The pH LGE experiments were performed at Na^+ concentrations of 0.10 (●), 0.125 (●), 0.15 (●), 0.175 (●), and 0.20 (●) mol/L. The salt LGE experiments were performed at pH values of 7.0 (●), 7.5 (●) and 8.0 (●). Straight lines depict the fitting result with the ligand density SD model, whereas the symbols represent the experimental data obtained from the LGE runs.

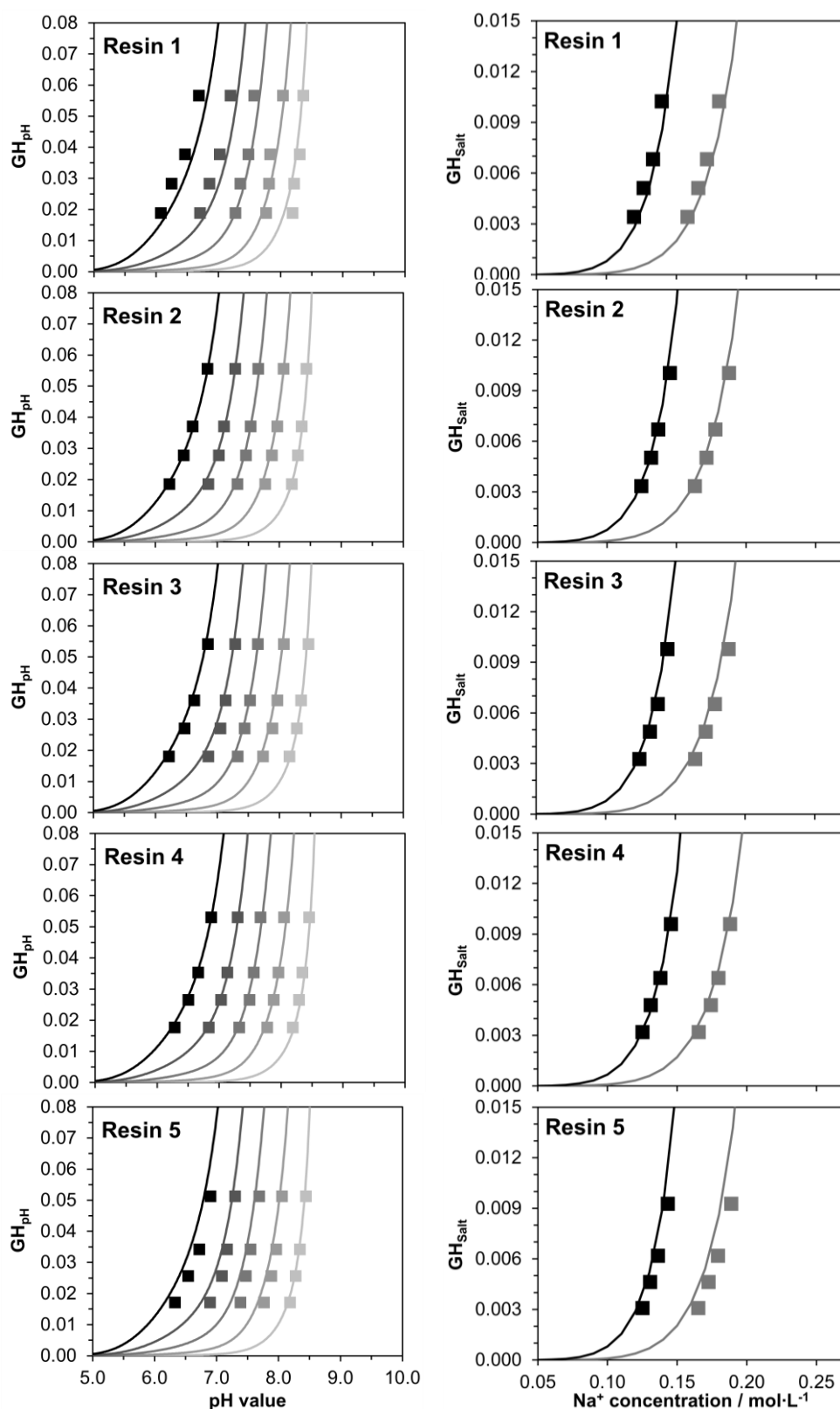


Figure 19. Eluting pH and Na^+ concentrations of the neutral variant (squares and lines) of mAb04 as a function of the normalized gradient slope ($GH_{pH/salt}$) on resin 1, 2, 3, 4 and 5. The pH LGE experiments were performed at Na^+ concentrations of 0.10 (■), 0.125 (■), 0.15 (■), 0.175 (■), and 0.20 (■) mol/L. The salt LGE experiments were performed at pH values of 7.5 (■) and 8.0 (■). Straight lines depict the fitting result with the ligand density SD model, whereas the symbols represent the experimental data obtained from the LGE runs.

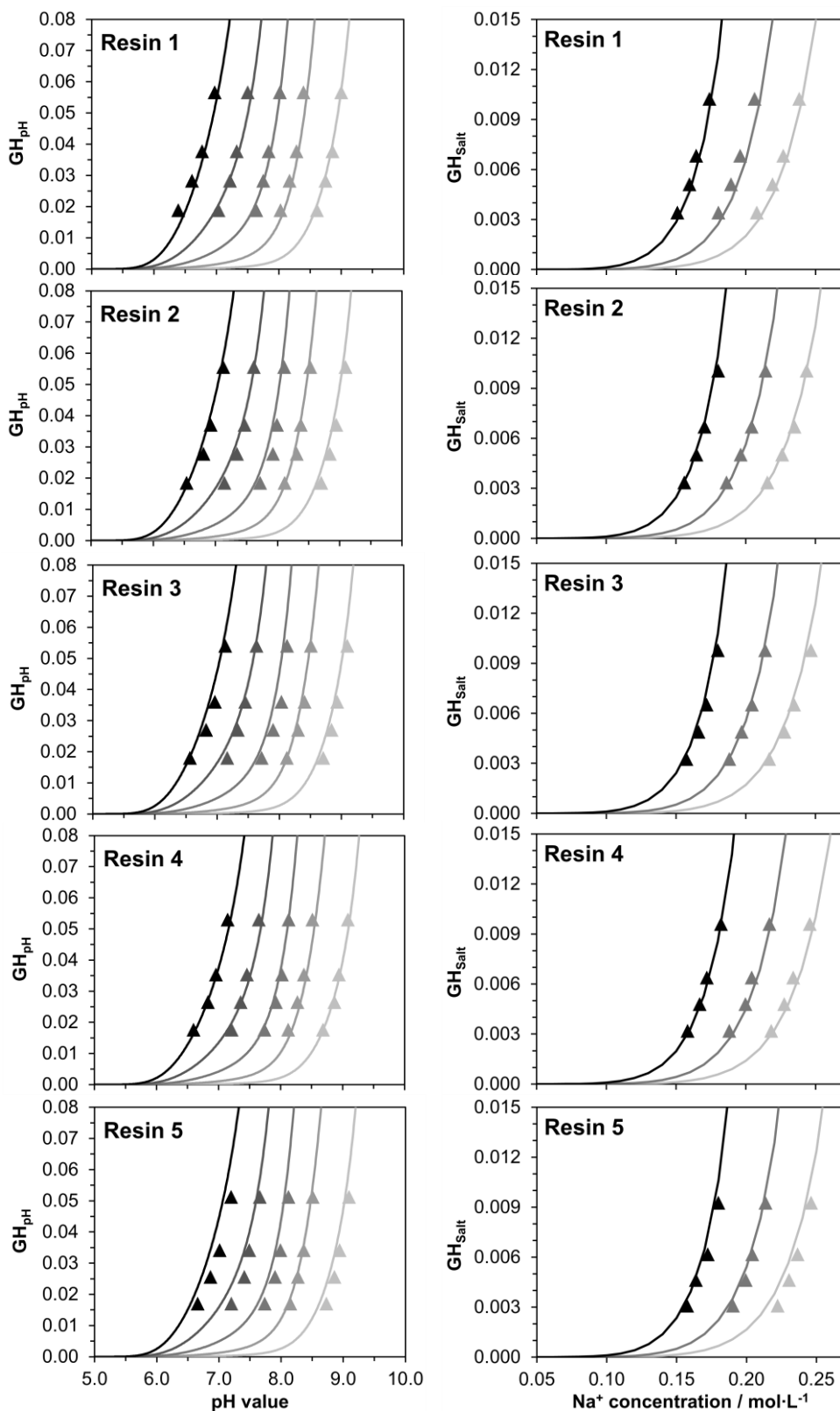


Figure 20. Eluting pH and Na^+ concentrations of the basic variant (triangles and lines) of mAb04 as a function of the normalized gradient slope ($GH_{pH/salt}$) on resin 1, 2, 3, 4 and 5. The pH LGE experiments were performed at Na^+ concentrations of 0.10 (\blacktriangle), 0.125 (\blacktriangle), 0.15 (\blacktriangle), 0.175 (\blacktriangle), and 0.20 (\blacktriangle) mol/L. The salt LGE experiments were performed at pH values of 7.0 (\blacktriangle), 7.5 (\blacktriangle) and 8.0 (\blacktriangle). Straight lines depict the fitting result with the ligand density SD model, whereas the symbols represent the experimental data obtained from the LGE runs.

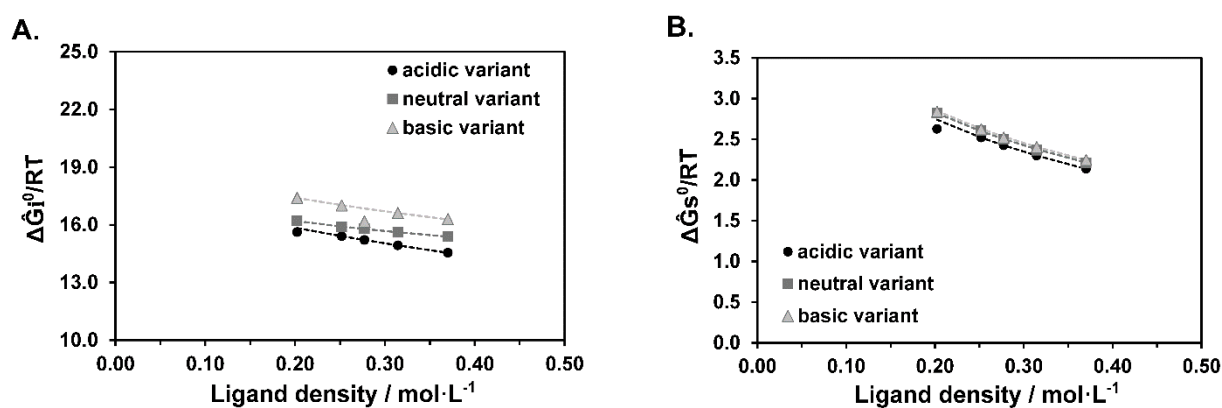


Figure 21. Dependency of the SD model parameters $\Delta\hat{G}_i^0/RT$ (A) and $\Delta\hat{G}_s^0/RT$ (B) of the acidic (●), neutral (■) and basic (▲) variant on the ligand density. The prediction curves using the ligand density SD model parameters (**Table 20**) are represented by the dashed lines.

The number of amino acids involved in binding allows the calculation of the characteristic protein charge (ν_i) as a function of pH according to Eq. (29). The characteristic charge of the acidic, neutral, and basic variant of mAb04 as a pH function is given in **Figure 22**. The values calculated according to Eq. (29) showed the necessity of three different ionizable groups. The dissociation constants (pK_{a_i}) of this three groups are also fitted and they refer to the carboxylic acid ($pK_{a_{carb}}$), amine groups ($pK_{a_{amine}}$) and N terminus ($pK_{a_{n-term}}$) of the protein. While N_{carb} , N_{amine} and N_{n-term} refer to the number of amino acids that are involved in the binding of a specific protein. For the data presented in this work, the acidic variant of mAb04 showed the lowest values of all dissociation constants and number of binding sites, followed by the neutral variant. The highest values of all dissociation constants and number of binding sites were observed for the basic variant of mAb04. The characteristic charge of the acidic, neutral, and basic variants decrease with increasing pH. The ν_i values of the basic variant are larger than the values for the neutral and acidic variant at all investigated conditions. And the ν_i values of the neutral variant are larger than the values of the acidic variant at all investigated conditions. Overall, the values calculated according to Eq. (29) based on the GH_{pH} correlations are in good agreement with the ν_i values obtained from the linear salt gradient elution experiments at fixed pH values (see **Table 19**). For reasons of clarity, no overlay was possible in **Figure 22** since the ν_i values of the five different prototypes are extremely close together and no real distinction is observed.

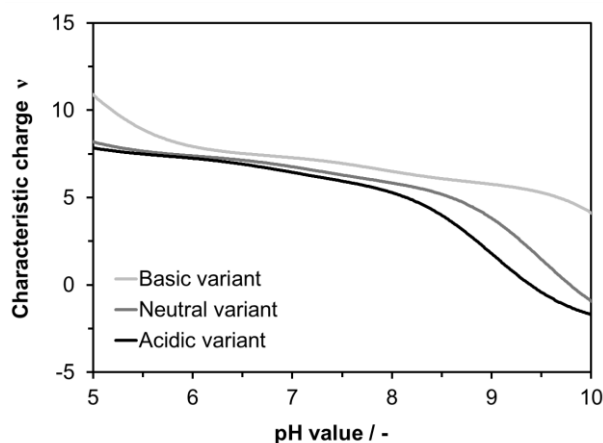


Figure 22. Characteristic binding charge for the acidic (—), neutral (—), and basic (—) variant of mAb04 on the Fractoge[®] EMD SO₃⁻ (M) prototypes as a function of pH. The v_i description is calculated with Eq.(29) and the model parameters displayed in **Table 20**.

3.2.3.5 *In silico* validation – Chromatogram simulation of CEX resins

In order to validate the proposed thermodynamic model, the experimental runs were compared to the predicted *in silico* chromatograms. The lumped rate model in conjunction with the model parameters (**Table 20**) was applied to obtain the *in silico* chromatograms.

Representative sets of linear salt gradient experiments and corresponding model simulations on the strong cation exchange with the lowest, middle, and highest ligand density are depicted in **Figure 23**. For reasons of clarity, **Figure 23** only shows the *in silico* chromatograms at a gradient volume of 40 CV. The verification of the model at 60, 80, and 120 CV for all three charge variants demonstrated a good correlation to the experimentally determined salt LGE experiments (data not shown).

The results in **Figure 23** show a good correlation between the experimental data and the *in silico* chromatograms. Small deviations are observed for the acidic variant at the base of the peak at pH 7.00 and 7.50 under all prototype resins investigated (**Figure 23.A-C**). While for the neutral variant, slight fronting at pH 7.50 and 8.00 is detected under all prototype resins investigated (**Figure 23.D-F**). On the other hand, the basic variant shows only minor fronting at pH 8.00 in all prototype resins investigated (**Figure 23.G-I**).

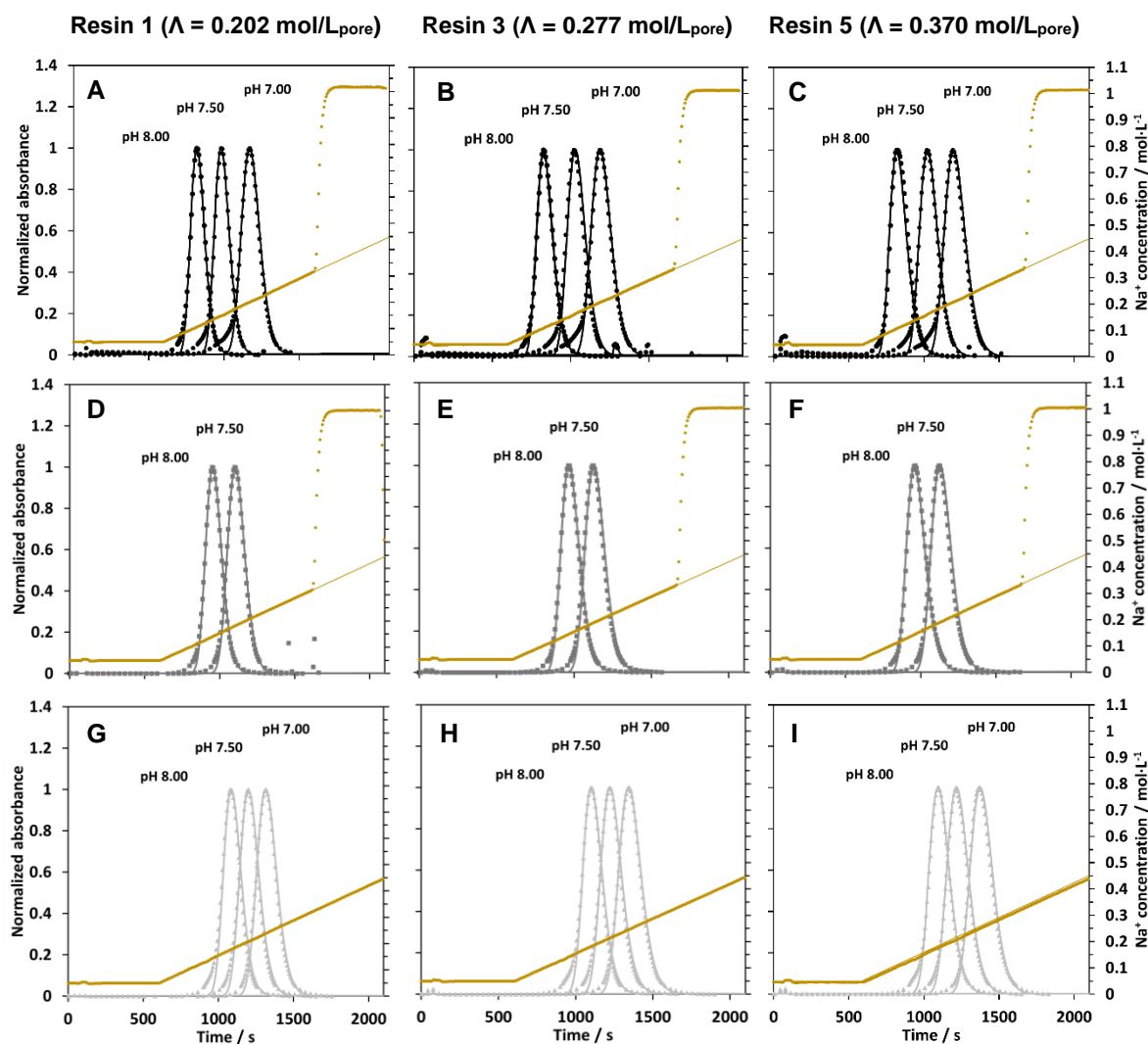


Figure 23. *In silico* chromatograms of salt gradients at different pH values for resin 1 (A, D and G), resin 3 (B, E and H), and resin 5 (C, F and I). Linear salt gradient elution from 0.05 mol/L to 1 mol/L Na⁺ concentration in 40 CV. The gradient experiments were performed with the acidic (●), neutral (■), and basic (▲) variant of mAb04. Experimental data (symbols) at different pH values are superimposed onto column simulations (acidic-black, neutral-grey, and basic-light grey solid lines). Flow rate = 1.67 mL/min. The determined values of D_{ax} per prototype resin were applied, as shown in **Figure 16**. The estimated k_{eff} values from **Table 21** were used for the *in silico* simulations.

The mass transfer coefficients were obtained by the reverse fitting of the chromatograms. The results for each salt gradient in **Figure 23** are shown in **Table 21**. The results for the acidic variant display a minimal increase of the k_{eff} values, independent of the ligand density, when the pH is increased. While the increase of the ligand density at a fix pH value showed a decrease of the k_{eff} values. The neutral variant on the other hand, exhibited no change on the k_{eff} values when the pH was increased in all ligand density resins tested. But the increase of the ligand density at a fixed pH value demonstrated a similar trend to the acidic variant by a decrease in the

k_{eff} values of the neutral variant. The basic variant demonstrated no change on the k_{eff} values on the lowest ligand density when the pH was increased. But a decrease in the k_{eff} values was evident for the middle and highest ligand density when the pH was increased. Here, as well a decrease of the k_{eff} values is observed when the ligand density is increasing at a fixed pH value.

Table 21: Estimated effective mass transfer coefficients (k_{eff}) on linear salt gradient elution experiments for the acidic, neutral, and basic variant of mAb04 at low (Res 1), middle (Res 3), and high (Res 5) ligand density.

Acidic variant			
	k_{eff} (cm ² ·s ⁻¹)		
pH value	RES 1	RES 3	Res 5
7.00	3.3 x 10 ⁻⁵	2.9 x 10 ⁻⁵	2.5 x 10 ⁻⁵
7.50	4.1 x 10 ⁻⁵	3.2 x 10 ⁻⁵	2.8 x 10 ⁻⁵
8.00	3.9 x 10 ⁻⁵	3.1 x 10 ⁻⁵	2.5 x 10 ⁻⁵
Neutral variant			
	k_{eff} (cm ² ·s ⁻¹)		
pH value	RES 1	RES 3	Res 5
7.50	3.7 x 10 ⁻⁵	2.8 x 10 ⁻⁵	2.5 x 10 ⁻⁵
8.00	3.7 x 10 ⁻⁵	2.8 x 10 ⁻⁵	2.4 x 10 ⁻⁵
Basic variant			
	k_{eff} (cm ² ·s ⁻¹)		
pH value	RES 1	RES 3	Res 5
7.00	3.1 x 10 ⁻⁵	2.5 x 10 ⁻⁵	2.4 x 10 ⁻⁵
7.50	3.1 x 10 ⁻⁵	2.6 x 10 ⁻⁵	2.3 x 10 ⁻⁵
8.00	3.2 x 10 ⁻⁵	2.7 x 10 ⁻⁵	2.5 x 10 ⁻⁵

Representative sets of linear pH gradient experiments and corresponding model simulations on the strong cation exchange with the lowest, middle, and highest ligand density are depicted in **Figure 24**. Once again, for reasons of clarity, **Figure 24** only shows the *in silico* chromatograms at a gradient volume of 40 CV. The verification of the model at 60, 80, and 120 CV for all three charge variants demonstrated a good correlation to the experimentally determined pH LGE experiments (data not shown).

The results in **Figure 24** show a good correlation between the experimental data and the *in silico* chromatograms. For the prototype resin 1 (**Figure 24.A**), small deviations in the base of the peak are observed at the acidic and basic variants, where the acidic

species show a slight fronting, while the basic species exhibit a more pronounced separation of the isoforms, which is indicated as a shoulder in front of the basic monomer in the chromatogram. The middle ligand density resin (**Figure 24.B**) showed a slight fronting of the elution peak for the acidic, neutral and basic variant, being the acidic variant with the more pronounced separation. For the prototype resin 5 (**Figure 24.C**) the separation of the acidic isoforms is clearly shown as a shoulder in front of the acidic monomer in the chromatogram.

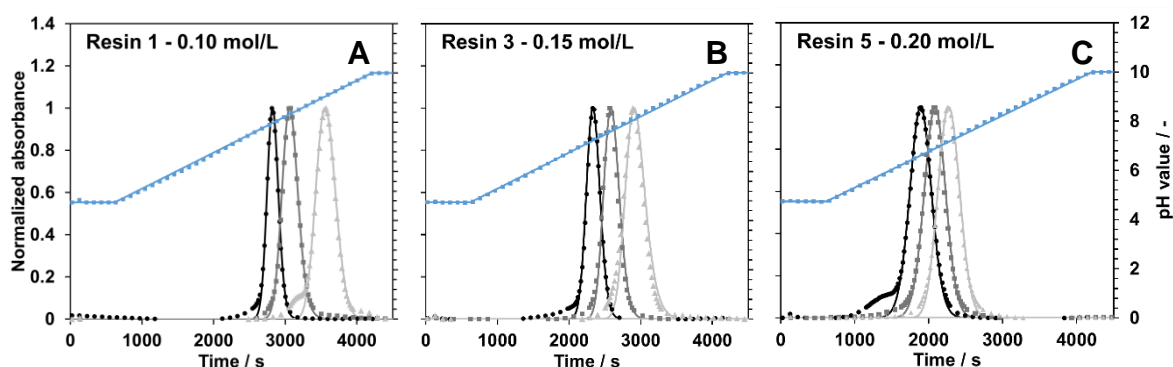


Figure 24. *In silico* chromatograms of linear pH gradients in the presence of 0.10 mol/L (A), 0.15 mol/L (B), and 0.20 mol/L (C) of Na⁺ ions for the acidic (●), neutral (■), and basic (▲) variant of mAb04 in resin 1 (A), resin 3 (B) and resin 5 (C). Linear pH gradient elution from pH 4.75 to pH 10 in 40 CV. Experimental data (symbols) of the charge variants of mab04 are superimposed onto column simulations (solid lines) of UV signal (acidic-black, neutral-grey, and basic-light grey), and pH (blue). Flow rate = 1.67 mL/min. The determined values of D_{ax} per prototype resin were applied, as shown in Figure 16. The estimated k_{eff} values from Table 22 were used for the *in silico* simulations.

Once again, the mass transfer coefficients were obtained by the reverse fitting of the chromatograms. The k_{eff} values for each pH gradient in **Figure 24** are shown in **Table 22**. The increase of Na⁺ ions in linear pH gradients do not show a clear trend on the k_{eff} values. Neither does the increase of ligand density reflect a correlation to the k_{eff} values, under the investigated conditions in this work.

Table 22: Estimated effective mass transfer coefficients (k_{eff}) on linear pH gradient elution experiments for the acidic, neutral, and basic variant of mAb04 at low (Res 1), middle (Res 3), and high (Res 5) ligand density.

Na ⁺ conc. (mol·L ⁻¹)	k_{eff} (cm ² ·s ⁻¹)			
	0.10	0.15	0.20	0.10
Variant ID	RES 1	RES 3	Res 5	RES 5
acidic	2.5×10^{-5}	3.0×10^{-5}	1.8×10^{-5}	1.8×10^{-5}
neutral	1.5×10^{-5}	2.2×10^{-5}	2.0×10^{-5}	1.1×10^{-5}
basic	1.8×10^{-5}	1.2×10^{-5}	2.6×10^{-5}	9.7×10^{-6}

The comparison of the elution behavior of the acidic, neutral, and basic variants at the lowest and highest ligand density of the strong cation exchange prototypes on a linear pH gradient is shown in **Figure 25**. Here, a clear separation of the basic variant is observed as a shoulder before the main peak at low and high ligand density. Overall, a good correlation between the simulation and experimental data is observed, and the difference in elution of the charge variants of mAb04 with respect to the ligand density variation is achieved. Elution that is properly described by the proposed thermodynamic model presented in this work.

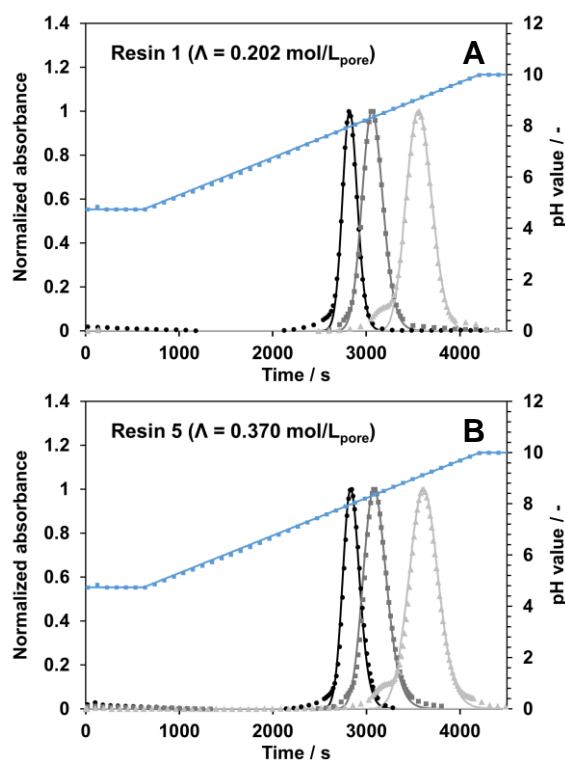


Figure 25. *In silico* chromatograms of linear pH gradients in the presence of 0.10 mol/L Na^+ ions for the acidic (\bullet), neutral (\blacksquare), and basic (\blacktriangle) variant of mAb04 in resin 1 (A), and resin 5 (B). Linear pH gradient elution from pH 4.75 to pH 10 in 40 CV. Experimental data (symbols) of the charge variants of mAb04 are superimposed onto column simulations (solid lines) of UV signal (acidic-black, neutral-grey, and basic-light grey), and pH (blue). Flow rate = 1.67 mL/min. The determined values of D_{ax} per prototype resin were applied, as shown in **Figure 16**. The estimated k_{eff} values from **Table 22** were used for the *in silico* simulations.

4 DISCUSSION

4.1 Modeling of anion exchange resins

4.1.1 Linear salt gradient elution experiments

An ion exchange process performance depends on a complex interrelationship between several parameters, such as protein properties, mobile phase conditions, and chromatographic resin characteristics. Therefore, the influence of ligand density variation on the performance of AEX was investigated in this work using linear salt gradient elution experiments with thirteen prototype resins. BSA and a monoclonal antibody (mAb03) were chosen as model proteins for proof of concept because of the significant difference in isoelectric point and molecular weight. The elution of these proteins was investigated with the application of linear salt gradients with varying gradient slopes at different pH values in the mobile phase. This approach allows the investigation of salt and ligand density influence on the IEC adsorption isotherm's linear range.

The increase in the pH of the mobile phase in AEX showed an increase in the eluting salt concentrations in the linear salt gradients. This was observed for all proteins in this study at all investigated pH values. This change in the retention of the proteins in the chromatographic resins reflects the change on the surface charge of the proteins. The further away the mobile phase pH is from the isoelectric point of the protein, the more pronounced the change in the protein charge. In this case, as the environment becomes more basic, the carboxyl groups of the protein are ionized, while the amino groups are neutral and the proteins become more negatively charged. Therefore, the electrostatic interactions between the ligands and the proteins become stronger. Here BSA and mAb03 displayed a typical behavior for AEX resins.

Additionally, the ligand density increase exposed an increase in the eluting counter-ion concentrations (i.e., higher protein retention). This was observed for the model proteins used in this study at all investigated pH values. Similar elution behaviors have been experimentally obtained in literature when using silica resins and strong anion exchange ligands, where the ionic capacity increase showcased stronger retention of the protein (Wu & Walters, 1992). Moreover, the increase in the ligand density exhibit an increase in the retention of two different monoclonal antibodies when AEX-MMC

prototype resins were evaluated for the ionic interaction half of the U-shape retention curve (Y. F. Lee et al., 2016). Furthermore, the increase on alkyl chain length and ligand density in HIC resins resulted in an increase in protein retention (Fausnaugh et al., 1984). It was demonstrated that large proteins with greater contact surface exhibit a continuous decrease in protein retention with decreasing ligand density. In general, several research groups have shown that independent of the chromatographic resin, the ionic interactions between the protein and the matrix are highly influenced by the ligand density of the stationary phase in liquid chromatography.

4.1.1.1 Ligand density dependency in the stoichiometric displacement model

It is well known that the elution of a protein in the linear range of the IEC adsorption isotherm is directly correlated to the gradient slope and the modifier (e.g., counter-ion concentration or pH) used to modulate the elution; as described by Yamamoto et al. with Equation (27) in section 2.6.3 (S. Yamamoto et al., 1983). This technique has become very popular over the past decades because it proposes a simple methodology to estimate equilibrium parameters from a set of pulse injections eluted at different gradient slopes. But this technique has several shortcomings, such as the disregard on the size exclusion effect of the modifier and the protein, as well as the simplification of the initial conditions ($c_{s,initial} = 0 \text{ mM}$). Here, a linearization by logarithmic transformation is common, and the parameters of the equilibrium constant (\widehat{K}_E) and the number of binding sites (ν_i) can be estimated from the slope and the intercept. Several publications have shown the practicality of the model for various proteins, including monoclonal antibodies and Fc fusion proteins on different CEX and AEX resins (Ishihara et al., 2007; Ishihara & Yamamoto, 2005; Rüdts et al., 2015; Shuichi Yamamoto & Ishihara, 1999; Shuichi Yamamoto, Nakanishi, Matsuno, & Kamijubo, 1983; S. Yamamoto et al., 1983). However, the inclusion of the size exclusion effects and standard thermodynamics had shown better adequacy to estimate the model parameters (Gerstner et al., 1994; Kluters et al., 2016; Mollerup, 2008; L. Pedersen et al., 2003; Schmidt et al., 2014; Urmann, Graalfs, Joehnck, Jacob, & Frech, 2010).

Additionally, it is important to mention that the estimation of \widehat{K}_E and ν_i in this project was done by the integration of the full model (also called the Inverse Method (IM)) as shown in Equation (24). The decision to use the full integration instead of a model

approximation, such as Yamamoto's equation or the 1st order solution, was based on the results presented by Pfister's study. (Pfister et al., 2015). Were the research group compared the optimal or "true" values obtained from the IM against the various model approximations and demonstrated a difference of \hat{K}_E and ν_i of 10% and 0.3%, respectively beside the 1st order approximated solution. While for the same conditions, the estimates from the 0th order (Yamamoto's equation) compared to the IM estimates showed a difference of more than 600% for \hat{K}_E and 12% for ν_i (Pfister et al., 2015). Therefore, the IM approach was the primary method of estimation in this investigation to obtain the model parameters, using the other approximation models only as a guide for validation on the range used to determine the equilibrium parameters.

In this work, the inclusion of the thermodynamic parameters such as the standard Gibbs energy change of association of the protein ($\Delta\hat{G}_i^0/RT$) and the counter-ion ($\Delta\hat{G}_s^0/RT$) were fundamental for the estimation of the equilibrium constant model parameter. Since the approach used in other publications (Osberghaus et al., 2012; Pfister et al., 2015; Rischawy et al., 2019) by directly fitting the equilibrium constant (\hat{K}_E) and the number of binding sites (ν_i) with the experimental data exhibited strong deviations; it was neglected (data not shown). This decision was made on the grounds that the obtained model parameters with this approach showed unreasonable parameter values and did not fulfill the thermodynamic conditions of Equation (5) as described by Mollerup's framework (Mollerup, 2008). According to Equation (5), $\ln \hat{K}_E$ is a linear function of the characteristic charge, which depends on pH.

Conclusively, the results in this investigation showed that the strategy, as described previously, was optimal to obtain the SD model parameters. The linear salt gradient experiments of both proteins at all pH values were described by the modeling data with good agreement, as seen in **Figure 1- 4**. The SD model was able to describe the elution behavior of both proteins but does not account for the ligand density variation of the resin, and three SD parameters ($\Delta\hat{G}_i^0/RT$, $\Delta\hat{G}_s^0/RT$ and ν_i) per resin are necessary. In total, 39 parameters are necessary to describe the retention of one protein over the whole range of ligand densities used in this investigation.

4.1.1.2 Ligand density dependency of the characteristic charge

The SD model presented by Kopaciewicz et al. does not account for the pH dependency of the characteristic charge (Kopaciewicz et al., 1983). Therefore, the SD model results in a single value of ν_i per resin on the evaluated pH. Several attempts to

include pH-dependent descriptors to predict protein chromatographic behavior at any pH can be found in the literature. For instance, Yang et al. incorporate it by describing the protein surface with charge and electrostatic potential properties, but protein crystal structures and sequence information of the protein is needed, which are not always available, especially at the early stages of the development process (Yang, Sundling, Freed, Breneman, & Cramer, 2007). Stahlberg and Jonsson described the electrostatic interaction of the protein and the surface of an ion exchange resin as two parallel oppositely charged slabs in contact with a buffered salt solution in a non-stoichiometric model (Ståhlberg & Jönsson, 1996). It is important to mention that the data in their investigation was analyzed according to the slab model with a fixed charged density. While, Guelat et al. used an extended Stahlberg model, which include the determination of the charge densities by considering the dissociation equilibria of the acid and basic groups on both surfaces, as well as the binding of counter-ions to the charged groups (Guélat, Ströhlein, Lattuada, & Morbidelli, 2010). Other models, such as the one presented by Bosma and Wesselingh, calculated the SMA isotherm's adsorption equilibrium constant from the protein net charge by using Coulomb's law (Bosma & Wesselingh, 1998). To add more detail into the model, Lenhoff and coworkers used a pseudo-colloidal model to account for the effect of electrostatic and van der Waals interactions on protein adsorption, which was accounted for with the protein molecular structure and surface properties (Roth & Lenhoff, 1993, 1995; Yoon & Lenhoff, 1992). Additionally, another number of researchers have used linear salt gradient (Kaltenbrunner et al., 2007) and isocratic elution data (Mollerup, 2008) at different mobile phase pH values to empirically correlate the dependency of the characteristic charge and the equilibrium constant. The different models presented above are just a small sample of literature showcasing a wide range of approaches to include the pH dependency on the adsorption isotherm in ion exchange chromatography. And highlights not only the importance and necessity of the pH description but additionally demonstrates the divergent pathways one can follow to describe the interactions required for mechanistic modeling and simulation of chromatography.

In this work, a compromise between practicality and functionality was made. Since a large number of the models presented above require a priori information on the proteins and impurities as well as molecular descriptions of the matrix, in addition to the determination of a large number of parameters, which results in prolonged

computational time, a simplified protein charge model was used. The proposed model to describe the characteristic charge is simple enough for routine use in data fitting and chromatographic process design and optimization, but which nevertheless describes the phenomena involved with reasonable accuracy.

The results of the characteristic charge from the SD model demonstrated that the number of binding sites are not only dependent on the pH of the mobile phase but also on the ligand density variation of the chromatographic resin. And although several researchers have addressed the ligand density as an important parameter influencing the separation performance in IEC, no mathematical model describing the variation of this parameter has been published (Aono et al., 2013; Deitcher et al., 2010; GE-Healthcare, 2019; Mollerup et al., 2010; D. Wu & Walters, 1992; Shuichi Yamamoto et al., 1999). According to the experimental data obtained from the SD model of the characteristic charge, the pH and ligand density dependency can be modeled using a correlation based on a modified protein net charge model (Equation (28)) where pKa_i is the dissociation constant of the ionizable group, and ν_0 describes the charge of the protein at pH values that are well below the pKa_i . A distinction between the number of amino acids involved on the protein-ligand binding which are affected by the ligand density variation (N_2) and those who are not (N_1) was made. A simple linear empirical relation for N_2 and the ligand density is assumed. N_1 and N_2 relate to the same amino acid with identical pKa_i values. Within the investigated ligand density range, the model states that additional binding sites (N_2) become available for the protein proportional to the ligand density. However, doubling the ligand density does not double the ν_i value but only the N_2 proportion (Bruch, Graalfs, Jacob, & Frech, 2009). These differences in the interaction of the protein with ligand density might suggest the importance of a specific interaction of certain binding sites on the protein surface at high ligand densities, as it has been shown in literature for smaller proteins (i.e., lysozyme) and other ion exchange resins (Dimer & Hubbuch, 2010). Whereas, at low ligand densities, the protein's net charge plays a more significant role than the actual surface charge distribution. The most probable explanation for this is that the increase in ligand density generates a change in the binding orientation of the protein or a change in the protein conformation, which causes a rise in the number of charged amino acids which become accessible for interaction with the charged ligand on the surface of the stationary phase. Once again, the importance of the surface charge and orientation of the protein in ion exchange chromatography has been proven extensively in literature,

but no further research on the juxtaposition with the ligand density variation in IEC resins, to the best of the author's knowledge, has been performed (Biesheuvel & Wittemann, 2005; Pérez & Frey, 2005; Roth & Lenhoff, 1993, 1995; Shen & Frey, 2004; Ståhlberg, 1999; Ståhlberg & Jönsson, 1996; Yoon & Lenhoff, 1992).

Lastly, it is noteworthy to highlight that the simplifications mentioned above were done on the basis that linear relationships had been proven to be effective in the modeling and simulation of preparative chromatography. Where not only a simplification of the protein charge using the Henderson-Haselbalch equation was successful (Westerberg, Broberg Hansen, Degerman, Budde Hansen, & Nilsson, 2012), but were the implementation of a linear dependency of pH on the characteristic charge has been proven to be enough to describe a narrow pH range (Kaltenbrunner et al., 2007; Kumar, Leweke, von Lieres, & Rathore, 2015; Rischawy et al., 2019; Stephen Hunt, 2017).

4.1.1.3 Ligand density dependency of $\Delta\hat{G}_i^0/RT$ and $\Delta\hat{G}_s^0/RT$

As previously discussed (sections 4.1.1, 4.1.1.1, and 4.1.1.2), the retention curves of mAb and BSA are strongly influenced by pH, salt concentration, protein, and ligand density. These influences can be explained with the thermodynamic parameters obtained with the ligand density SD model presented in this work. The dependency on the retention of the proteins with the change in the ionic capacity of the prototype resins was confirmed with the linear salt gradient elution experiments.

To comprehend the changes in the Gibbs energy change of association of the protein and the counter-ion first is important to understand the simplifications made on the development of the SD model. It is noteworthy to point out that the adsorption models are derived from fundamental thermodynamic principles, and the complexity depends on the activity coefficients. In the SD model, it is assumed that all activity coefficients are unity or constant. And therefore, it is possible to use Equation (5) to calculate the practical equilibrium constant \hat{K}_E . As a result, what is observed on the model parameters obtained from the SD model is an apparent increase in the practical equilibrium constant \hat{K}_E since the activity coefficients are neglected. Mollerup et al. demonstrated that the equilibrium excess functions account for the deviations from the ideal solution behavior (Mollerup et al., 2010). If it is assumed that any impact of the ligand density on the activity coefficients of the species (i.e., protein and counter-ion) in solution and the activity coefficients of the counter-ion in the adsorbate state on the

definition of the equilibrium constant in Equation (4) are neglectable. In that case, the apparent increase of the practical equilibrium constant is due to an increase on the asymmetric activity coefficient of the protein in the adsorbate state. Assumptions that are derived and explained in section 2.6.2 demonstrated to be true for the calculation of the practical equilibrium constant. The proposed thermodynamic model called hereinafter ligand density SD model shows how the equilibrium distribution is affected by changes in the total resin capacity (Equation (23)). The results indicate that it is possible to calculate the initial slope of the adsorption isotherm with the description proposed in section 3.1.2.2 for the number of binding sites and the model parameters from the ligand density SD model ($\Delta G_s^0/RT$, $\Delta G_i^0/RT$, $A_{1/2}$ and $A_{2/1}$). Results that are in agreement with the definition of the Gibbs energy change of association of the counter-ion ($\Delta G_s^0/RT$), where the parameter is specific to the salt-adsorbent pair, and is independent of pH for strong electrolytes (Mollerup, Hansen, Kidal, & Staby, 2008). As well as the definition of the Gibbs energy change of association of the protein ($\Delta G_i^0/RT$), where the parameter is specific to the protein adsorbent pair, and it is independent of the concentration of solvents as well as of the pH (Mollerup et al., 2010). By applying these definitions, it is observed that the model parameters in **Table 14** are in good agreement. For instance, if retention data are measured for several proteins using the same salt absorber pair, $\Delta G_s^0/RT$ should be a common parameter. In this investigation, a difference of ~ 0.3 units on the $\Delta G_s^0/RT$ values of mAb and BSA is observed. While the difference in the practical Gibbs energy change of association of the counter-ion ($\Delta \hat{G}_s^0/RT$), between mAb and BSA never exceeds a difference of 0.4 units. The small deviation of the $\Delta G_s^0/RT$ values might be the result of the salt activity coefficient simplification used during model derivation. Additionally, it is reasonable to assume that the system has experimental uncertainty, and for this reason the values are considered to lie in the same range. Therefore, concluding that $\Delta G_s^0/RT$ is protein and ligand density independent. Furthermore, Lee and coworkers (Y. F. Lee et al., 2016) studied the retention of two monoclonal antibodies in mix-mode chromatography (AEX-MMC) resins and evidenced a negative correlation of the model parameter $\Delta \hat{G}_s^0/RT$ when the ionic capacity increased. These results indicate that the description of the ligand density SD model presented in this study, might be transferable to different absorber materials when the same counter-ion is applied. Moreover, Pederson et al. has reported similar trends for AEX resins, showing even negative values of $\Delta \hat{G}_s^0/RT$ for very high ligand density (L. Pedersen et al., 2003). One can explain the negative

correlation of $\Delta\hat{G}_s^0/RT$ by reflecting on how the low ligand density has less charge density, and thus a more hydrophobic environment that lead to higher $\Delta\hat{G}_s^0/RT$ values and vice versa for high ligand density.

Meanwhile, the results of the ligand density SD model shows the standard Gibbs energy changes of the protein ($\Delta G_i^0/RT$) as a negative value for BSA and a positive value for mAb03. These differences might reflect the variation in protein characteristics, such as hydrophobicity (L. Pedersen et al., 2003). Moreover, the practical standard Gibbs energy changes of the protein ($\Delta\hat{G}_i^0/RT$) reflects a dependency on the protein and ligand density, contrary to the $\Delta G_i^0/RT$ parameter that is independent of the ionic capacity. To describe the observed dependencies on the practical standard Gibbs energy changes of the protein, the implementation of the Wilson model was employed (Binh Son Vo & David C. Shallcross, 2005; Wilson, 1964). The parameters representing the molecular interactions between the protein and the counter-ion at low protein concentrations proved to be necessary to describe the ligand density dependency. In this case, the interaction coefficients could be correlated using one value for $A_{1/2}$ and $A_{2/1}$ for each protein independent of the ligand density and the pH in solution. It has been reported that the interaction parameter $A_{1/2}$ is protein size dependent (Klutters, 2016). In this work, the IgG antibody employed has a molecular weight of ~150 kDa, while BSA has a molecular weight of 66 kDa. Therefore, the results obtained with the ligand density SD model are in good agreement, showing a higher value for the $A_{1/2}$ parameter of mab03, compared to the $A_{1/2}$ value of BSA.

Lastly, the equilibrium constant obtained with the SD model parameters ($\Delta\hat{G}_s^0/RT$, $\Delta\hat{G}_i^0/RT$ and ν_i) is compared to the calculated equilibrium constant achieved with the ligand density SD model. As seen in **Figure 7**, the addition of the characteristic charge description in conjunction with the mathematical descriptions of the thermodynamic parameters accurately describes the elution of both model proteins in the whole range of pH and ligand density variation investigated in this work. Slight deviations on the equilibrium constant for both proteins can be observed at high pH values. This is due to the fact that at low salt concentration and high pH values, the Donnan effect is exacerbated (Wittkopp et al., 2018). This phenomenon is not included in the model used in this investigation, and in section 4.1.1.5, the importance of the environmental conditions the protein is exposed will be discussed. Overall, the model accurately describes the observed equilibrium constant of both model proteins, and it confirms

that when using a proper description of the equilibrium constant, the variation on the ligand density can be characterized.

4.1.1.4 *In silico* validation – Chromatogram simulation of AEX resins

To investigate the consistency of the proposed model, a lumped rate model and the obtained model parameters ($\Delta G_s^0/RT$, $\Delta G_i^0/RT$, $A_{1/2}$ and $A_{2/1}$) were used to perform *in silico* chromatogram simulations. First, the calibration runs of the modeling experiments for mAb03 and BSA with the thirteen prototype resins were investigated. To be able to model the peak shape of the elution peak in chromatography, it is necessary to account for several effects in the column such as convection, dispersion, diffusion, and overall mass transfer resistances. Because a lumped rate model is applied, several effects are lumped, and the estimated effective mass transfer coefficient (k_{eff}) and the axial dispersion coefficient (D_{ax}) are assumed to be responsible for the broadening of the chromatograms. Therefore, to corroborate the model approach, the effective mass transfer coefficient is needed to be estimated from the protein elution profile according to the inverse estimation method, as described in Section 2.6.6.1. Since the experiments presented in this investigation were performed in the isotherm linear range, the mass transfer coefficient is assumed to be independent of protein concentration (Schmidt-Traub et al., 2012). The ability to lump certain effects into one parameter to describe the mass transfer resistance has been demonstrated in the literature, showing almost no difference between this model and more detailed models (G. Guiochon, 2006; Golshan-Shirazi & Guiochon, 1992; Seidel-Morgenstern, 1995). The results in **Table 15** shows the application of the parameter k_{eff} to describe the rate limitations in the column. The influence of the variation on the ligand density correlates to a significant extent to the mass transfer coefficient. Although no detailed investigations of the influence of ligand density on a lumped mass transfer coefficient was found in literature, this effect can be explainable by a decrease on the mass transfer coefficient. Since the resistance is the reciprocal of the mass transfer coefficient (Hansen & Mollerup, 2004), a small value of k_{eff} represents a higher mass transfer resistance. This means that the bigger the value of the mass transfer coefficient, the faster the equilibrium is reached between the solid and the mobile phase and a sharper peak will be observed in the elution. Therefore, these results shows that the increase in ligand density decreases the driving force to reach the equilibrium. One can imagine how the introduction of more ligands will affect the

movement of the protein inside the pores, and therefore the transport of the protein between the liquid phase and the pore phase will be different. On the other hand, the influence observed with the change on the modulator (i.e., pH and ionic strength) on the mass transfer coefficient is in good agreement with the results encountered in literature (Hedrich, Wittkopp, & Frech, 2020; Pfister & Morbidelli, 2015). Remarkably good agreement was observed on the simulations of the salt gradients thus confirming the validity of the proposed approach.

Additionally, dual gradient experiments were simulated and experimentally verified. Since these separation runs were not used for model calibration, the results demonstrate the applicability of the extended model for linear salt and dual pH/salt gradients. A good correlation between all *in silico* simulations and the experimentally obtained UV curves was observed. As a whole, the results presented in section 3.1.2.4 demonstrates that the parameters obtained from the ligand density SD model can be used for simulation of retention times and chromatograms at any desired pH values and salt concentrations using a lumped rate model. Definitely, individual verification is recommended when working outside the calibration range of the model. Nevertheless, it can be seen in **Figure 9** that the model is able to predict the retention of the proteins even outside the calibration area. Overall, the simulations show that a good agreement between experimental chromatographic runs and simulations can be obtained.

4.1.1.5 Ligand density dependency of the characteristic charge (v_i) – a Donnan equilibrium in ion exchange chromatography

As shown in section 3.1.2.2, the consideration of the influence of the ligand density on the v_i values in the modeling, was achieved by introducing an empirical model (Eq. (28)). And although this description proved to be sufficient to describe the pH and ligand density dependency, as well as the prediction of the characteristic charge of the proteins, this description does not give any physico-chemical explanation for the observed effects. For this reason, a more detailed model was needed to fully explain and understand the effects on the binding of the protein.

It is well known that in IEC with porous materials, a significant amount of the active sites are inside the resin phase, and thus intraparticle conditions play a key role in the process. Therefore, the uptake of ions should not be neglected since it has a significant influence on the intraparticle pH. The strict calculation of intraparticle conditions is important because this will affect not only the protein interactions, but other zwitterionic

species, as well as the extent of dissociation of weak electrolytes and buffer species (Jansen et al., 1996).

In literature, the use of an ideal Donnan approach has been reported by Hardin and Ivory, where experimental evidence was presented on a pH shift on the resin phase when compared to the mobile phase pH on an anion exchange material (Hardin & Ivory, 2006). The reported model was able to describe the effect and showed that depending on the mobile phase salt concentration, the resin phase pH is found to be more than one pH unit higher than that of the buffer phase. Additionally, similar effects have been predicted for cation exchange materials with a decreased pH value in the resin phase (Wittkopp et al., 2018; J. Wu, Jiao, Zhuang, Zhou, & Ying, 2016). Based on these investigations, the ion exchange model is reassessed to cover a Donnan equilibrium. This was done by following Jansen's framework (Jansen et al., 1996). The introduction of the Donnan ratio (r_D) (Eq. (30)) allows the estimation of the counter-ion concentration in both phases, as well as the calculation of the intraparticle pH (Eq. (31)). It is important to mention that the protein net charge, as well as the binding charge, are pH-dependent, and the intraparticle conditions strongly influence these parameters, therefore the importance of accounting for the ion exchange between the resin and the mobile phase. Whereas, the simplifying assumptions of the stoichiometric displacement model (e.g., co-ions are totally excluded from the adsorbate phase, resin and mobile phase pH are equal, and the amount of counter-ions in the resin phase is equal to the resin capacity (Kopaciewicz et al., 1983)) completely neglect these effects.

The addition of the Donnan ratio to describe the characteristic charge (Eq. (44)) shows how it is not necessary to include the ligand density in the calculation, but instead is more important to account for the environmental conditions at which the protein is exposed in the resin phase. By extending the protein net charge model of ν_i to include two ionizable groups and the pH in the resin phase (pH_R), the dependency of the characteristic charge can be described. To be able to describe both protein's datasets, a slight modification on Eq. (31), by means of a θ_i factor was required. The outcome in **Figure 10** prove the reliability of the model when applying the fitting results in **Table 16**. It is interesting to see that when using the pH_{resin}^θ , equation 34 takes a form which is used to describe charge regulation of proteins when interacting with charged surfaces in non-stoichiometric ion exchange models (Hartvig, van de Weert, Østergaard, Jorgensen, & Jensen, 2011; Salis et al., 2011). Thereby demonstrating the relevance of the proposed model.

The fitting results of v_i for mAb03 reveal two amino acids having a dissociation constant of 8.3 and 11.0 ($pK_{a_{D,1}}$ and $pK_{a_{D,2}}$, respectively). Because the applied model is a simplified version of a protein net charge model, only two ionizable groups are assumed to be the main contributors to the binding of the protein. This can be done due to the narrow operational pH range at which the experiments in this work were performed. In this case, the fitting results can be directly correlated to the side chain residues of the N-terminus and Tyrosine, respectively, on folded proteins (Grimsley, Scholtz, & Pace, 2009; Guélat, Delegrange, Valax, & Morbidelli, 2013). While the fitting results of v_i for BSA reveal two amino acids having dissociation constants of 7.2 and 9.2 ($pK_{a_{D,1}}$ and $pK_{a_{D,2}}$, respectively). These values can then be correlated to the side chain residues of Histidine and Cysteine, respectively, on folded proteins (Grimsley et al., 2009; Guélat et al., 2013).

The two ionizable groups prove to be relevant for the description of the dependency of the pH values, while the θ_i factors were needed to describe both proteins with the Donnan ratio. The fitting value of the θ_i factor for mAb03 was close to 1, whereas the value for BSA was above 1. Looking closely at Equation (31), it can be observed that when the $\theta_i = 1$, the description of the pH_{resin} of the Donnan model does not change. But if the θ_i is different than 1, then the $pH_{resin}^{\theta} = pH_B + \theta_i \cdot \log(r_D)$. For BSA the observed deviation ($\theta_i > 1$) might be due to the fact that the experiments were performed at a pH range where BSA changes conformation reversibly (Rosenoer, Oratz, & Rothschild, 2015). The transition from the Neutral conformation (N) to the Basic conformation (B) is reported to occur between pH 7.0 and pH 9.0 (Foster, 1977; X. Wang, Guo, & Ma, 2009). Zurawski and Foster demonstrated that the latter transition midpoint happens at pH 8.17, while the decrease in the N fraction starts as early as pH 7.10, conditions that are fulfilled in all the experiments of BSA (**Figure 9**) presented in this research (Zurawski & Foster, 1974). In addition, it has been reported that this transition is significantly different from a simple two-state process indicating that more than two isoforms are present during this conformational change (Giancola, De Sena, Fessas, Graziano, & Barone, 1997).

Further emphasis on the conformational changes of BSA can be observed in **Figure 9** ($\theta_{BSA} = 1$), where an additional effect showed by the partition of the data points with a ligand density above 200 mmol/L_{pore} is observed. The partition showing a higher number of binding sites indicates the elution of the protein above 0.30 mol/L Cl⁻ concentration. The salt dependency on BSA's protein conformation has been

previously reported by Zhang and coworkers (F. Zhang et al., 2007). With the use of small-angle X-ray scattering (SAXS), the authors showed that three different protein forms are needed to describe the range at low ionic strength ($I < 0.3$ mol/L), moderate ionic strength ($I = 0.3$ mol/L and 0.5 mol/L) and high ionic strength ($I > 0.5$ mol/L), results that are in agreement with the observation presented in this work. Here, the use of the θ_i factor functions as a protein dependent parameter, and accounts for different conformations of BSA, which depends strongly, not only on pH but as well on the salt concentration. The addition of protein conformation dependencies would help to describe the change in the characteristic charge of BSA at extended ranges of NaCl and pH; however, such explorations are beyond the scope of this investigation.

Overall, the description of the characteristic charge introduced in this section resulted in a good agreement with the number of binding sites obtained from the SD model. Therefore, the influence of ligand density on the retention of the protein can be explained by the intraparticle conditions at which the protein is exposed in the pore volume of the matrix. As shown in this investigation, the Donnan equilibrium model can be a great tool to gain a deeper understanding of key variables in the ion exchange chromatography process.

4.2 Modeling of cation exchange resins

4.2.1 CEX column parameters

The determination of the porosities in mechanistic modeling and simulation of chromatography is of great importance since it is considered a limiting factor for the transport of the species in the column. Originally, the porosities of the matrix were neglected in the ideal or basic model of chromatography (G. Guiochon, 2006), but to be able to understand other effects in the separation (e.g., mass transfer resistances, axial dispersion, etc.), the simplification of homogeneous particles is not possible anymore. Therefore, the introduction of the lumped rate model has become very popular in recent years since these effects can be explained with the molecular mechanisms in the porous frame of the stationary phase. Although the advantages of having a more detail model to describe the ion exchange process are clear, the practical determination of the porosities is not a trivial task; several authors have reported the difficulties of the measurement (L. Pedersen et al., 2003; Schmidt-Traub et al., 2012; Thomas et al., 2013). It is not only important to find a suitable tracer for

injection, which is non-interacting and non-pore-penetrating, but it has been reported that tentacle materials collapse due to increased salt concentration (DePhillips & Lenhoff, 2000). Thus, conditions for the measurement of porosities were investigated in this research since the pore area of the stationary phase can be directly correlated to a change in the ligand density. First, the influence of the pH in the mobile phase at a fixed salt concentration (50 mM NaCl) was tested. These results showed no influence on the retention of Dextran at the investigated pH values (i.e., the molecule is not retained). The polar character of the blue dextran proved to be a suitable tracer to determine porosities in CEX resins. While the different conditions in salt concentration at a fixed pH resulted in slightly different retention of the molecule and different peak shape. Results that are in agreement with the literature and the proven theory of conformational changes of the tentacles when the salt concentration is increased in the mobile phase (Bhambure et al., 2017; Bhambure et al., 2016; DePhillips & Lenhoff, 2000, 2001; Schmidt-Traub et al., 2012; Thomas et al., 2013). This observation may be explained by the charge repulsion and hydrophilic behavior of the tentacles at a low salt concentration that leads to an extension of the tentacles in the pore space since the charges in the tentacles are repulsed by each other. On the other hand, at high salt concentrations, the ionic groups on the tentacles surface are neutralized, and the hydrophobicity of the long polymer chains increases and the charge repulsion decreases (Thomas et al., 2013). This will result in an expansion of the pore region at low salt concentrations and a shrinkage of the tentacle region at high salt concentrations. To obtain an accurate representation of the tentacles at binding conditions, the porosity measurements were determined at a low salt concentration (50 mM NaCl) and pH 6.00. The results of these measurements are displayed in **Table 17** and show the void fraction of the column (ε), the porosity of the solid phase (ε_p), and the total porosity (ε_t) of the prototype CEX resins. According to the definition of the interstitial porosity, this value should be independent of the change in ligand density, since the space of the void fraction (i.e., the volume between and around the particles) is not influenced by the changes in the porous frame. Definition that is consistent with the measurements of ε obtained in this work, which shows almost an unaffected value of ε when the ligand density is increased. On the other hand, the total porosity (ε_t) and the intraparticle porosity (ε_p) showed a variability in the values of 4.2% and 6.3%, respectively, when comparing the lowest and highest ligand density. As discussed for the AEX resins, the consideration of the standard deviation and other uncertainties of

the actual measurement must be taken into account. And once again, it is difficult to determine if the variability is coming from the practical determination or the measurement is really showing the influence of the ligand density on the parameters. Additionally, Thomas et al. has demonstrated that the use of a medium-size dextran (~2, 000 kDa), like the one used in this investigation, possesses certain polydispersity, thereby producing an overestimation of the calculated porosity (Thomas et al., 2013). Thomas and coworkers' results exhibited a difference in porosities of up to 12% in relation to the polydispersity of the tracer (Thomas et al., 2013). As a result of this variability, a simplification of the porosities was made. The interstitial porosity ε and the total porosity ε_t were estimated as an average value from the obtained measurements as; 0.35 and 0.76, respectively. The intraparticle porosity ε_p was calculated from the total porosity and the interstitial porosity by implementing Eq. (38). This assumption was made since previous publications had shown that the correlation of the data, is not sensible to the choice of the porosity, when reasonable values of ε are used (L. Pedersen et al., 2003). Consequently, the estimated porosities ($\varepsilon = 0.35$ and $\varepsilon_t = 0.76$) were used to calculate the ligand density in the pore volume with equation (42).

The next parameter to characterize the CEX prototypes is an exclusion factor that is dependent on the stationary phase and a given solute species. The exclusion factor ($k_{d,i}$) represents the extent of permeation of the molecule of interest into the pore volume of the stationary phase material in a packed column. This parameter is independent of the column volume and the particle size of the adsorbent (DePhillips & Lenhoff, 2000). Per definition $k_{d,i}$ has a value between unity and zero, where the value of one is given to compounds able to permeate and access the total pore volume (e.g., common ions) and less than one for larger molecules (e.g., proteins) (Mollerup, 2008). As a result, a $k_{d,i}$ value equal to 0 represents a totally excluded compound.

The determination on the exclusion factor of the acidic, neutral and basic variant of mab04 under non-binding conditions in the five strong cation exchange prototype resins revealed that the $k_{d,i}$ values at a fixed ligand density remain almost unaffected with the different charge variants. However, the measurements at different ligand densities showed a decrease in the $k_{d,i}$ values of the acidic (V1), neutral (V2), and basic (V3) variant of mab04 when the ionic capacity was increased. The first observation can be explained by the fact that the different charge variants have a very similar overall structure with only minor variations in the amino acid sequence (i.e., the

charge variants have very similar molecular weight). This means that the permeation of the proteins through the same pore space will yield equivalent $k_{d,i}$ values. While the second observation can be explained due to the fact that modifications on the pore space will affect the ability of the protein to penetrate different pore spaces. For example, an increase in the ligand density will decrease the pore volume by having a more crowded pore space. Additionally, the variability detected between the charge variants at a fixed prototype resin is under the uncertainties of the experimental determination, and therefore it was reasonable to assume a charge variant independent $k_{d,i}$ value as a useful simplification. Assumption that has been proven to be pertinent in previous publications (Y. Lee, Jöhnck, & Frech, 2017).

Given the bed porosity values (ε , ε_t and ε_p) and the exclusion factor ($k_{d,i}$), the last parameter missing to be able to fully characterize the columns is the axial dispersion coefficient (D_{ax}). According to the lumped rate model that is incorporated in this work, the dispersion coefficient is assumed to depend only on the packing properties and flow conditions (Schmidt-Traub et al., 2012). Therefore, the axial dispersion coefficient was measured at different flow rates on the five strong cation exchange prototype resins. The determined D_{ax} values for all ligand densities evaluated in this investigation showed similar behavior; an increase in the axial dispersion coefficient when the flow rate increases. For typical chromatographic conditions, the axial dispersion coefficient becomes proportional to the velocity (Hansen & Mollerup, 2004; Schmidt-Traub et al., 2012; van Deemter, Zuiderweg, & Klinkenberg, 1995). And although at first sight, the results in **Figure 16** does not show a linear relationship, the results at low to moderate flow rates can be approximated to a linear behavior. Here, it is important to mention that the highest flow rate tested was the maximum linear flow rate allowed by the pressure limit and the recommended by the manufacturer. Therefore, under these conditions, the description of the D_{ax} value solely by the eddy diffusion is not enough and other effects such as the molecular diffusion must be considered (van Deemter et al., 1995).

Another remark on the determined D_{ax} values are shown by the fact that all ligand densities with the exception of the lowest ligand density (Resin 1), displayed very similar values. As seen in **Figure 16**, Resin 1 has a significantly higher measurement of D_{ax} values when compared to the rest of the prototype resins. However, this cannot be explained by the asymmetry factor determined for the CEX prototypes. The column performance was measured after the packing of the columns by injecting acetone and

measuring the peak asymmetry (A_s), under the exact same conditions. The A_s values obtained for Resin 1 to Resin 5 are 1.04, 1.06, 1.00, 1.01, and 0.97, respectively. Therefore showing that all prototype resins have similar packing efficiencies.

Despite the fact that a fixed value per resin prototype of D_{ax} was used on further simulations (i.e., all the experiments were performed at a single velocity), it was important to understand and characterize the different resins with varying ligand density. Altogether, the results on the column's characterization are in agreement with the fact that an increase on the ligand density is occurring when going from the lowest ionic capacity in Resin 1 to the highest ionic capacity in Resin 5. And although the ionic capacity of the gravity settled resin ($\Lambda_{\text{Dry gel}}$) given by the manufacturer already showed this tendency, the measurements presented in this work confirm this statement.

4.2.2 Linear gradient elution experiments

The influence of ligand density on the performance of CEX resins was investigated in this work using linear salt and pH gradient elution experiments with five prototype resins. The elution behavior of the purified mAb04 charge variants was investigated with the application of linear salt gradients at different pH values with varying gradient slopes. Similar to the linear salt gradient elution experiments at fixed mobile pH, linear pH gradient elution experiments at fixed salt counter-ion concentrations were performed. The combination of both approaches enables the investigation of both salt and pH influence on the IEC adsorption equilibrium, in addition to the ligand density influence as explained before. These experiments were carried out individually with the isolated mAb04 charge variant samples. As explained in section 1.1, often the final product of a biopharmaceutical typically displays heterogeneity induced by post-translational modifications that are known to impact the biological activity of the product (Liu, 2015; Monnet et al., 2014; Wada, Matsui, & Kawasaki, 2019). Hence, the interest in the IgG charge variants' purification to ensure proper safety and efficacy profiles.

As expected, the outcome of the linear salt gradients showed that an increase on the pH of the mobile phase in CEX resins results on a decrease on the eluting salt concentrations. This was observed for the acidic, neutral, and basic variant of mAb04 in this study at all investigated pH values. This change in the retention of the proteins in the chromatographic resins reflects the change in the surface charge of the proteins. The closer the mobile phase pH is from the isoelectric point of the protein, the lower the charge will be until a neutral charge is reached at the pI. Here, the electrostatic

interactions between the ligands and the proteins become weaker as the pH increases, displaying a typical behavior for CEX resins. Additionally, the increase on the ligand density exposed an increase on the eluting counter-ion concentrations (i.e., higher protein retention). This was observed for the model proteins used in this study at all investigated pH values. As mentioned in section 4.1.1, this behavior has been previously observed on several chromatographic resins, showing that the ionic interactions between the protein and the matrix are highly influenced by the ligand density of the stationary phase in liquid chromatography (Deitcher et al., 2010; Fausnaugh et al., 1984; Fogle et al., 2012; Y. F. Lee et al., 2016; Lu, Lin, Gao, & Yao, 2013; D. Wu & Walters, 1992).

The impact of the pH as a mobile phase modifier on IEC's performance was also investigated by linear pH gradient elution experiments as an alternative to the salt gradients. To obtain controllable, linear pH gradients over a broad pH range, Kröner and Hubbuch's methodology plus Urbansky and Schock's calculations were implemented (Kröner & Hubbuch, 2013; Urbansky & Schock, 2000). The pH gradient was generated externally with a discontinuous buffer system containing only anionic or zwitterionic substances to avoid interactions of the buffering compounds with the functional groups of the CEX resin (Kröner & Hubbuch, 2013).

The first column in **Figure 18**, **Figure 19**, and **Figure 20** show the dependency between the normalized pH gradient slope and the eluting pH values of the chromatographed proteins. As expected, the eluting pH values are shifted to lower eluting pH values with increasing counter-ion concentrations in the mobile phase. This behavior was observed for all charge variants in this study at all investigated conditions. This is caused by the change in the binding strength of the protein; as the ionic strength increases the salt ions compete with the bound proteins for charges on the surface of the stationary phase. Therefore, the higher the counter-ion concentration on the mobile phase, the lower the protein's binding strength, and the faster the proteins will elute. Additionally, the pH gradients revealed that for all investigated proteins, the GH_{pH} plots are shifted to higher eluting pH values (i.e., higher protein retention) when the ligand density is increased. The determined eluting pH values on the lowest ligand density for the acidic, neutral and basic variants are in the range between 5.81 and 7.99, 6.07 and 8.37, and 6.37 and 9.01, respectively. While the eluting pH values at the lowest ligand density for the acidic, neutral and basic variants are in the range between 6.05 and 8.05, 6.33 and 8.44, and 6.66 and 9.09,

respectively. Confirming once again that the ionic interactions between the protein and the matrix are highly influenced by the ligand density of the stationary phase in IEC (Deitcher et al., 2010; Fausnaugh et al., 1984; Fogle et al., 2012; Y. F. Lee et al., 2016; Lu et al., 2013; D. Wu & Walters, 1992).

4.2.2.1 Stoichiometric displacement model

The same approach as described in section 4.1.1.1, was implemented to evaluate the LGE experiments and determine the SD model parameters for the CEX prototype resins. Since the SD model does not account for the pH dependency on the characteristic charge, the pH LGE experiments were not included in this evaluation. The results in this investigation showed that the strategy, as described before, was optimal to obtain the SD model parameters.

The linear salt gradient experiments of the charge variants of mAb04 at all pH values were described by the modeling data with good agreement, as seen in **Figure 17**. Once again, the SD model was able to describe the elution behavior of all proteins but does not account for the ligand density variation of the resin, and three SD parameters ($\Delta\hat{G}_i^0/RT$, $\Delta\hat{G}_s^0/RT$ and ν_i) per resin per protein are necessary. Overall, very similar trends are observed for the thermodynamic parameters, like the ones shown in section 3.1.2.3 for the AEX resins. Comparing the thermodynamic parameters with varying ligand densities, an apparent decrease of $\Delta\hat{G}_s^0/RT$ and $\Delta\hat{G}_i^0/RT$ is observed when the ionic capacity is increased. This trends can be explained by the proposed thermodynamic model called in this work as ligand density SD model and will be explained in more detail in section 4.2.2.2.

The pH dependency on the characteristic binding charge ν_i can be observed in **Table 19**. The respective fitted values of the SD model's characteristic binding charge show remarkably similar values between the acidic, neutral, and basic variants. These values lie in the range of 5.12 and 7.35, while at a fix pH value the ν_i does not change more than 1.29 units between the charge variants. This is in agreement with the fact that the different charge variants have a very similar overall structure with only minor variations in the amino acid sequence (i.e., the charge variants have very similar molecular weight), and the binding is driven only by the small changes in the group residues of the proteins. These results are in good agreement with several publications showing the mechanistic modeling and simulation of charge variants in the literature (Kumar et al., 2015; Y. Lee et al., 2017). Additionally, as expected, the number of

binding sites of the SD model revealed a decrease in the ν_i values when the mobile phase pH is increasing. In CEX, the protein is binding to the stationary phase with a positive net charge, and the further away the mobile phase pH (i.e., more acidic pH values) is from the pI of the protein, the higher the binding charge will stand. By definition, larger ν_i depicts stronger protein-ligand binding, therefore the protein will be retained, and the protein will elute later. This behavior can be correlated to the isoelectric points of the charge variants of mAb04 (see **Appendix**). For example, the acidic variant has a pI of ~8.15, and the SD model parameters show the lowest characteristic charge values among the three charge variants, values that are in agreement with the weaker binding of the protein. While the basic variant has a pI of ~8.40, and the SD model parameters show the highest characteristic charge values among the three charge variants. Whereas the neutral variant shows a middle point between the acidic and basic variant of the characteristic charge values, with a pI of ~8.25. Lastly, the characteristic binding charge of all three charge variants depict almost unaffected values of ν_i , as the ligand density is increased. This shows how the acidic, neutral and basic variants are almost not sensitive to the addition of ligands in the stationary phase, in the investigated range of ionic capacity.

4.2.2.2 Ligand density model based on a Stoichiometric displacement model

It was shown in the previous sections (see sections 4.1.1.2 - 4.1.1.4) that for anion exchange chromatographic resins, the proposed thermodynamic model was able to describe the elution behavior of the model proteins and ligand density variation. Here, the transferability of the ligand density SD model to CEX resins was tested. To extend the design space of this process, in addition to salt gradient elution experiments, linear pH gradient elution experiments were performed. The dependency on the retention of the charge variants with the change in the ionic capacity of the prototype CEX resins was confirmed with both linear gradient elution experiments.

The ligand density SD model proved to be able to describe the elution behavior of the charge variants in the CEX resins (**Figure 18 Figure 20**). The fitting results for the IEC descriptions are displayed in **Table 20**. These results indicate that it is possible to calculate the initial slope of the adsorption isotherm with the description proposed in section 3.2.3.4 for the number of binding sites and the model parameters from the ligand density SD model ($\Delta G_s^0/RT$, $\Delta G_i^0/RT$, $A_{1/2}$ and $A_{2/1}$). The introduction of the

activity coefficient of the protein in the adsorbate state into the adsorption isotherm showed that it is possible to describe the ligand density dependency on both thermodynamic parameters; $\Delta\hat{G}_p^0/RT$ and $\Delta\hat{G}_s^0/RT$ (**Figure 21**). Likewise, these results, confirm the assumption that the thermodynamic parameters are interchangeable between salt and pH-induced elution. Even though the $\Delta\hat{G}_p^0/RT$ and $\Delta\hat{G}_s^0/RT$ parameters were determined only from the salt gradient experiments.

Moreover, the obtained ligand density SD model parameters are in agreement with the definition of the Gibbs energy change of association of the counter-ion ($\Delta G_s^0/RT$), where the parameter is specific to the salt-adsorbent pair and is independent of pH for strong electrolytes (Mollerup et al., 2008). Showing only a small variation of the $\Delta G_s^0/RT$ values of less than 0.1 units between the charge variants. While the definition of the Gibbs energy change of association of the protein ($\Delta G_i^0/RT$), where the parameter is specific to the protein adsorbent pair, and it is independent of the concentration of solvents as well as of the pH was also confirmed (Mollerup et al., 2010). Here, the $\Delta G_i^0/RT$ values for the charge variants are all positive and in the same range. Showing once again, the similarity on the molecular weight and the difference coming only from small variations on the amino acids side chains of the proteins.

The elution behavior of all investigated proteins can be described using the pH dependence according to Eq. (29) (Schmidt et al., 2014). Because of the extensive pH range in the CEX dataset, compared to the AEX experiments, the simplification in Eq. (28) was no longer possible to implement. The protein net charge model used to describe the characteristic binding charge utilize three ionizable groups involved in the binding. The first fitted value for the dissociation constant (pKa_i), shows that the value lies in a range between 4.37 and 4.80 for the charge variants, which can be correlated to the deprotonated carboxylic acids of several amino acids and residues groups such as the aspartic acid, glutamic acid, and C-terminal (Grimsley et al., 2009; Guélat et al., 2013; Kozlowski, 2016; Schmidt et al., 2014). The second fitted dissociation constant (pKa_i), revealed a range between 9.01 and 10.87, which can be correlated to the amine groups of lysine, tyrosine, and arginine (Grimsley et al., 2009; Guélat et al., 2013; Kozlowski, 2016; Schmidt et al., 2014). While the third fitted dissociation constant (pKa_i), displayed a range between 6.82 and 7.86, values that can be correlated to the N-terminus of a protein (Grimsley et al., 2009; Guélat et al., 2013; Kozlowski, 2016; Schmidt et al., 2014). The decision on adding the pKa_i to the fitting parameter list was due to the fact that values in literature either are assumed to be equal to the pKa_i of

free amino acids or they differ depending on the experimental setup in which they were measured (e.g., NMR or indirect techniques). This is important to mention since the pK_{a_i} values of many ionizable groups in folded proteins are strongly influenced by the local environment (Grimsley et al., 2009). The pK_{a_i} measurement will expose different effects on the microenvironment of the individual residues that are found in the protein structure and might not be comparable to the residues of other proteins. Three main factors that will influence the pK_{a_i} of the ionizable groups in folded proteins are charge-charge interactions, charge-dipole interactions (hydrogen bonding), and dehydration (Born effect) (Kozłowski, 2016). Therefore the estimation of the pK_{a_i} values for the current dataset was assumed to be more accurate.

An additional fitting parameter for this model is the number of amino acids that are involved in the binding of a specific protein, in this case, referred as N_{carb} , N_{amine} and N_{n-term} . The results for the acidic variant of N_{carb} , N_{amine} and N_{n-term} , showed the lowest values from all three charge variants. These values will translate to the lowest characteristic charge values, as shown in **Figure 22**. At a pH distant to the isoelectric point of the protein, binding to an IEC stationary phase is generally stronger than at a pH near the pl. As explained before, the acidic variant has the weakest binding to the stationary phase, followed by the neutral variant and lastly, the basic variant with the strongest protein-ligand binding. The estimated parameters are pH-dependent and are in good agreement with the protein net charge model. Additionally, the ligand density SD model parameters, including the characteristic charge calculated as a function of the mobile pH for the acidic, neutral and basic variant, are in good agreement with the data obtained from the linear salt gradient elution experiments. Please note that the over interpretation of the v_i -pH dependence curves (**Figure 22**), especially at low (pH<5) and high (pH>9) pH values, should be avoided, and individual verification is advised when working outside the calibration range of the model.

Lastly, slight deviations of the $GH_{pH/salt}$ curves at the highest ligand density can be observed in **Figure 18** **Figure 20**. These differences might indicate that the differences in between the mobile phase pH and the pH on the resin are exacerbated and could impact the characteristic binding charge of the protein, as described in section 4.1.1.5. If a larger set of ligand density variations would be considered, the implementation of the influence of the pH in the resin phase over the number of binding sites, would be advised. Thereby, the dependency on pH and ligand density can be described. As seen in **Figure 18** **Figure 20**, a more detailed description of the characteristic charge

was not needed in this investigation. Overall, the ligand density SD model accurately describes the observed equilibrium constant (i.e., SD model parameters) of the acidic, neutral and basic variants, and it confirms that when using an accurate description of the equilibrium constant, the variation on the ligand density can be characterized.

4.2.2.3 *In silico* validation – Chromatogram simulation of CEX resins

To prove the consistency of the proposed model, a lumped rate model with the obtained model parameters ($\Delta G_s^0/RT$, $\Delta G_i^0/RT$, $A_{1/2}$ and $A_{2/1}$), and the characteristic charge description (Eq. (29)) was used to perform *in silico* chromatogram simulations. The calibration runs of the modeling experiments for the acidic, neutral, and basic variants with the five prototype resins were investigated.

To perform the simulations, the remaining parameter is the effective mass transfer coefficient (k_{eff}). The model does not contain a description of the modulator dependence on the effective film transfer coefficient. Therefore, this parameter was estimated separately for each elution profile according to the inverse estimation method, as described in section 2.6.6.1. The other parameter affecting the broadening of the chromatograms is the axial dispersion coefficient (D_{ax}), and as mention in section 3.2.2.4, it was determined beforehand for each prototype resin over a range of velocities in individual experiments. The measurement of D_{ax} at the specific flow rate at which the chromatographic run was performed was implemented in the simulations.

The values obtained for the mass transfer coefficients in the linear salt gradient elution experiments demonstrated a correlation to the ligand density variation. The lowest ligand density resin showed a low mass transfer resistance, while the resin with the highest ionic capacity displayed the highest mass transfer resistance. On the other hand, the k_{eff} values on the linear pH gradient elution experiments, as shown in **Table 22**, might be deceiving. At first glance, the trend of a continuing decrease in the k_{eff} values with increasing ligand density are not fulfilled. However, it is important to remember that the conditions for the pH experiments that are displayed in this table are at different sodium concentrations. As reported by Pfister and Morbidelli, the change in the modulator has an influence on the mass transfer coefficient and could explain the small discrepancies between the k_{eff} values (Pfister & Morbidelli, 2015). Nevertheless, the direct comparison of the experiments performed at 0.10 mol/L Na⁺ concentration between the lowest ligand density (Resin 1) and the highest ligand density (Resin 5) reinstate the correlation with the ionic capacity. The results from both

linear gradients elution experiments confirm the observations found with the AEX resins on the k_{eff} values.

A remarkably good agreement was observed on the salt gradients' simulations, thus confirming the validity of the proposed approach. The linear pH gradient experiments' simulations showed minimal deviations at the base of the peak for the charge variants. Under these conditions, a separation of the monoclonal antibody's charge variants is observed and can be corroborated by the fact that the initial samples are only enriched but not completely pure (as seen in section 3.2.1.2). Overall, a good correlation between the simulation and experimental data is observed and the difference in elution of the charge variants of mAb04 in respect to the ligand density variation was achieved. The ligand density SD model proved to be transferable and is able to describe the variation of ligand density in cation exchange chromatography. Nevertheless, it is important to mention that this observation is valid for the specific grafting density and polymerization degree presented in this work, and caution is advised when generalizing to other chromatographic resins.

The thermodynamic model presented in this work proved to describe the elution behavior of charge isoforms of a monoclonal antibody (mAb04), in addition to the influences of the modulators and the ligand density variation of the stationary phase. Consequently, the ligand density SD model has a significant impact not only on the area of modeling and simulation of chromatography but, more importantly, on the process development in the biopharmaceutical industry. The influence of raw material variability is still a blind spot in the manufacturing of biopharmaceuticals (GE-Healthcare, 2019). To the author's knowledge, no ligand density variation has been modeled before over such an extensive range. Therefore, the model presented in this work will not only help to elucidate the influence of raw material variability on the robustness of the process but can also assist in the development of strategies to mitigate these influences in the process.

5 CONCLUSIONS

Significant retention differences on diverse model proteins were observed for anion and cation exchange resins, which have the same support but varying ligand densities. The ligand density's influence on the retention of proteins had been reported previously, and it was confirmed in this study.

The proposed thermodynamic model describes the retention of proteins in the linear range of the IEC isotherm. This model was parameterized using AEX and adsorption isotherm data for a monoclonal antibody, and BSA adsorbed to AEX prototype resins with varying ligand densities. Essentially, all of the data are well-described by a minimum number of parameters, revealing that a compromise between practicality and functionality on certain assumptions is possible without jeopardizing accuracy. Thereafter, the model proved to be transferable to cation exchange resins, and the introduction of pH linear gradients was achieved. This was done by using the description of ν_i and the model parameters ($\Delta G_i^0/RT$, $\Delta G_s^0/RT$, $A_{1/2}$, and $A_{2/1}$), showing that the whole range of ligand density variation can be predicted.

Moreover, the pH dependency was introduced in the equilibrium constant through the description of the characteristic binding charge. This approach demonstrated to be valid and useful to describe the different datasets, but it is worth noting that the complex descriptions used in this work to describe the observed dependencies (pH, ligand density) on ν_i are needed to cover such a wide range of experiments. Nevertheless, the range in the variability of commercially available resins is smaller, and the authors acknowledge that several descriptions might be then even further simplified.

The ligand density SD model has the potential to be used as a predictive tool to narrow the design space for IEC processes, but more work remains to be completed. For example, the research of other groups is in good agreement with the evidence presented in this work, with the behavior of varying ligand densities; nevertheless, extrapolation to other chromatographic resins must be proved. As well as additional research at high protein loadings that can corroborate the accuracy of the proposed model at overloading conditions. These possible additions will help create a fully developed model to better understand the influences of the ligand density variations in the preparative scale of downstream process development.

Lastly, the results of this investigation make it clear that this modeling and simulation approach can be used for faster development of new chromatographic separations, optimization of existing processes, process validation, and scale-up (Kaltenbrunner et al., 2007; Rischawy et al., 2019; Roush et al., 2020). However, the process development and optimization of chromatography is not the only field that will benefit from this approach, but root cause investigations (i.e., troubleshooting) in the manufacturing process in real-time could soon be a reality. For instance, it has been reported in the literature an irreversible reduction in ligand density after an acid treatment on the column, a process that is very typical for cleaning in place (CIP) and is considered a routine step in the biopharmaceutical industry (G. Wang, Briskot, Hahn, Baumann, & Hubbuch, 2017). An issue that can be detected and addressed by implementing the proposed thermodynamic model, as shown in this study.

6 ABSTRACT

The purification of a biopharmaceutical is not a simple task, and to ensure the quality and consistency of a product, a deep understanding of the unit operations must be achieved. Currently, the method of choice to tackle this problem is mainly focused on chromatographic techniques. For instance, ion exchange chromatography (IEC) is often used as a polishing step on the purification train of biopharmaceuticals because it provides effective removal of product-related impurities and contaminants. IEC is a powerful and ubiquitous unit operation in the purification of therapeutic proteins. However, an ion exchange process's performance depends on a complex interrelationship between several parameters, such as protein properties, mobile phase conditions, and chromatographic resin characteristics. Consequently, batch variations of IEC resins play a significant role in the robustness of these downstream processing steps. Ligand density is known to be one of the main lot-to-lot variations, affecting protein adsorption and separation performance. The use of a model-based approach can be an effective tool for comprehending the impact of parameter variations (e.g., ligand density) and their influence on the process.

The objective of this work was to apply mechanistic modeling to gain a deeper understanding of the influence of ligand density variations in ion exchange chromatography. First, the stoichiometric displacement model was applied to describe the retention of mAb and BSA at different ligand densities, but a dependency on the thermodynamic parameters $\Delta\hat{G}_p^0/RT$, $\Delta\hat{G}_s^0/RT$ and ν_i was observed. To overcome this hurdle and be able to describe the observed dependencies on the ligand density variation, some assumptions in the SD model were reconsidered. Such as the introduction of the activity coefficient of the protein in the adsorbate state into the adsorption isotherm. By using the description of ν_i and the model parameters ($\Delta G_i^0/RT$, $\Delta G_s^0/RT$, $A_{1/2}$, and $A_{2/1}$) the whole range of ligand density variation can be predicted. Thereafter, the model proved to be transferable to cation exchange resins, and the prediction of monomer isoforms of monoclonal antibody retention was achieved.

The ligand density SD thermodynamic model that was introduced in this investigation can describe the influence of governing IEC process parameters, such as the salt concentration, the pH of the mobile phase, the variation of ligand density on the stationary phase, and protein variations. Moreover, the use of a modified protein net

charge model proved to describe the dependence of pH and salt concentration in the adsorbate phase on the characteristic charge, showing that the influence of ligand density on the retention of the protein can be explained by the intraparticle conditions at which the protein is exposed in the pore volume of the matrix.

Lastly, it is noteworthy to mention that the ligand density SD model has a significant impact not only on the area of modeling and simulation of chromatography but, more importantly, on the process development in the biopharmaceutical industry. The influence of raw material variability is still a blind spot in the manufacturing of biopharmaceuticals (GE-Healthcare, 2019). Novel molecular formats display a pattern of similar product-related impurities and have become a real challenge to obtain a reliable separation method. These new modalities have not only the intrinsic heterogeneity of the host mAb (i.e., glycosylation, aggregation, etc.) but are also very susceptible to production process modifications and storage conditions, leading to a complex purification process. New high-resolution methods can be applied, but this comes with their limitations, such as high sensitivity (small variations will lead to different attributes in the final product). Therefore, to ensure the quality and consistency of a product, the variability of process parameters and raw material attributes must be addressed. To the extent of the author's knowledge, no ligand density dependency has been modeled before with such an extensive range. Therefore, the model presented in this work will help to elucidate the influence of raw material variability on the robustness of the process and assist in the development of strategies to mitigate these influences in the process.

7 REFERENCES

- Aono, H., Ilescu, I., Cecchini, D., Wood, S., & McCue, J. T. (2013). Mitigation of chromatography adsorbent lot performance variability through control of buffer solution design space. *Journal of Chromatography A*, 1318, 198-206. doi:<https://doi.org/10.1016/j.chroma.2013.10.019>
- Barbier, L., Ebbers, H. C., Declerck, P., Simoens, S., Vulto, A. G., & Huys, I. (2020). The Efficacy, Safety, and Immunogenicity of Switching Between Reference Biopharmaceuticals and Biosimilars: A Systematic Review. *Clinical Pharmacology & Therapeutics*, 108(4), 734-755. doi:<https://doi.org/10.1002/cpt.1836>
- Beck, A., Diemer, H., Ayoub, D., Debaene, F., Wagner-Rousset, E., Carapito, C., . . . Sanglier-Cianféron, S. (2013). Analytical characterization of biosimilar antibodies and Fc-fusion proteins. *TrAC Trends in Analytical Chemistry*, 48, 81-95. doi:<https://doi.org/10.1016/j.trac.2013.02.014>
- Beck, A., & Liu, H. (2019). Macro- and Micro-Heterogeneity of Natural and Recombinant IgG Antibodies. *Antibodies (Basel, Switzerland)*, 8(1), 18. doi:<https://doi.org/10.3390/antib8010018>
- Bhambure, R., Angelo, J. M., Gillespie, C. M., Phillips, M., Graalfs, H., & Lenhoff, A. M. (2017). Ionic strength-dependent changes in tentacular ion exchangers with variable ligand density. II. Functional properties. *Journal of Chromatography A*, 1506, 55-64. doi:<https://doi.org/10.1016/j.chroma.2017.05.021>
- Bhambure, R., Gillespie, C. M., Phillips, M., Graalfs, H., & Lenhoff, A. M. (2016). Ionic strength-dependent changes in tentacular ion exchangers with variable ligand density. I. Structural properties. *Journal of Chromatography A*, 1463, 90-101. doi:<http://dx.doi.org/10.1016/j.chroma.2016.08.010>
- Biesheuvel, P. M., & Wittemann, A. (2005). A Modified Box Model Including Charge Regulation for Protein Adsorption in a Spherical Polyelectrolyte Brush. *The Journal of Physical Chemistry B*, 109(9), 4209-4214. doi:<https://doi.org/10.1021/jp0452812>
- Bosma, J. C., & Wesselingh, J. A. (1998). pH dependence of ion-exchange equilibrium of proteins. *AIChE Journal*, 44(11), 2399-2409. doi:<https://doi.org/10.1002/aic.690441108>
- Boswell, C. A., Tesar, D. B., Mukhyala, K., Theil, F.-P., Fielder, P. J., & Khawli, L. A. (2010). Effects of Charge on Antibody Tissue Distribution and Pharmacokinetics. *Bioconjugate Chemistry*, 21(12), 2153-2163. doi:<https://doi.org/10.1021/bc100261d>
- Bruch, T., Graalfs, H., Jacob, L., & Frech, C. (2009). Influence of surface modification on protein retention in ion-exchange chromatography. *Journal of Chromatography A*, 1216(6), 919-926. doi:<http://dx.doi.org/10.1016/j.chroma.2008.12.008>
- Carta, G., & Jungbauer, A. (2011). *Protein Chromatography: Process Development and Scale-Up*. (First Edition ed. Vol. 34). Weinheim: Wiley-VCH.
- Deitcher, R. W., Rome, J. E., Gildea, P. A., O'Connell, J. P., & Fernandez, E. J. (2010). A new thermodynamic model describes the effects of ligand density and type,

- salt concentration and protein species in hydrophobic interaction chromatography. *Journal of Chromatography A*, 1217(2), 199-208. doi:<https://doi.org/10.1016/j.chroma.2009.07.068>
- Delorme, E., Lorenzini, T., Giffin, J., Martin, F., Jacobsen, F., Boone, T., & Elliott, S. (1992). Role of glycosylation on the secretion and biological activity of erythropoietin. *Biochemistry*, 31(41), 9871-9876. doi:<https://doi.org/10.1021/bi00156a003>
- DePhillips, P., & Lenhoff, A. M. (2000). Pore size distributions of cation-exchange adsorbents determined by inverse size-exclusion chromatography. *Journal of Chromatography A*, 883(1), 39-54. doi:[https://doi.org/10.1016/S0021-9673\(00\)00420-9](https://doi.org/10.1016/S0021-9673(00)00420-9)
- DePhillips, P., & Lenhoff, A. M. (2001). Determinants of protein retention characteristics on cation-exchange adsorbents. *Journal of Chromatography A*, 933(1), 57-72. doi:[https://doi.org/10.1016/S0021-9673\(01\)01275-4](https://doi.org/10.1016/S0021-9673(01)01275-4)
- Dismer, F., & Hubbuch, J. (2010). 3D structure-based protein retention prediction for ion-exchange chromatography. *Journal of Chromatography A*, 1217(8), 1343-1353. doi:<https://doi.org/10.1016/j.chroma.2009.12.061>
- Fausnaugh, J. L., Kennedy, L. A., & Regnier, F. E. (1984). Comparison of hydrophobic-interaction and reversed-phase chromatography of proteins. *Journal of Chromatography A*, 317, 141-155. doi:[https://doi.org/10.1016/S0021-9673\(01\)91654-1](https://doi.org/10.1016/S0021-9673(01)91654-1)
- Fogle, J., Mohan, N., Cheung, E., & Persson, J. (2012). Effects of resin ligand density on yield and impurity clearance in preparative cation exchange chromatography. I. Mechanistic evaluation. *Journal of Chromatography A*, 1225, 62-69. doi:<https://doi.org/10.1016/j.chroma.2011.12.048>
- Fogle, J., & Persson, J. (2012). Effects of resin ligand density on yield and impurity clearance in preparative cation exchange chromatography. II. Process characterization. *Journal of Chromatography A*, 1225, 70-78. doi:<https://doi.org/10.1016/j.chroma.2011.12.049>
- Foster, J. F. (1977). Some Aspects of the Structure and Conformational properties of serum Albumin. In V. M. Rosenoer, M. Oratz, & M. A. Rothschild (Eds.), *Albumin: Structure, Function and Uses* (pp. 53-84): Pergamon.
- Franke, A., Forrer, N., Butte, A., Cvijetic, B., Morbidelli, M., Johnck, M., & Schulte, M. (2010). Role of the ligand density in cation exchange materials for the purification of proteins. *Journal of Chromatography A*, 1217(15), 2216-2225. doi:<https://doi.org/10.1016/j.chroma.2010.02.002>
- G. Guiochon, A. F., D.G. Shirazi, A. Katti. (2006). *Fundamentals of Preparative and Nonlinear Chromatography* (2nd Edition ed.): Academic Press.
- GE-Healthcare. (2019). Quality by design in biotherapeutics purification: understanding and addressing sources of process variability [White paper] [Press release]. Retrieved from <https://landing1.gehealthcare.com/QBD-biotherapeutics-purification.html>
- Gerstner, J. A., Bell, J. A., & Cramer, S. M. (1994). Gibbs free energy of adsorption for biomolecules in ion-exchange systems. *Biophysical Chemistry*, 52(2), 97-106. doi:[https://doi.org/10.1016/0301-4622\(94\)00006-9](https://doi.org/10.1016/0301-4622(94)00006-9)

- Giancola, C., De Sena, C., Fessas, D., Graziano, G., & Barone, G. (1997). DSC studies on bovine serum albumin denaturation Effects of ionic strength and SDS concentration. *International Journal of Biological Macromolecules*, 20(3), 193-204. doi:[https://doi.org/10.1016/S0141-8130\(97\)01159-8](https://doi.org/10.1016/S0141-8130(97)01159-8)
- Giezen, T. J., Mantel-Teeuwisse, A. K., & Leufkens, H. G. M. (2009). Pharmacovigilance of Biopharmaceuticals. *Drug Safety*, 32(10), 811-817. doi:<https://doi.org/10.2165/11316550-000000000-00000>
- Golshan-Shirazi, S., & Guiochon, G. (1992). Comparison of the various kinetic models of non-linear chromatography. *Journal of Chromatography A*, 603(1), 1-11. doi:[https://doi.org/10.1016/0021-9673\(92\)85340-Y](https://doi.org/10.1016/0021-9673(92)85340-Y)
- Grimsley, G. R., Scholtz, J. M., & Pace, C. N. (2009). A summary of the measured pK values of the ionizable groups in folded proteins. *Protein Sci*, 18(1), 247-251. doi:<https://doi.org/10.1002/pro.19>
- Guélat, B., Delegrange, L., Valax, P., & Morbidelli, M. (2013). Model-based prediction of monoclonal antibody retention in ion-exchange chromatography. *Journal of Chromatography A*, 1298(Supplement C), 17-25. doi:<https://doi.org/10.1016/j.chroma.2013.04.048>
- Guélat, B., Ströhlein, G., Lattuada, M., & Morbidelli, M. (2010). Electrostatic model for protein adsorption in ion-exchange chromatography and application to monoclonal antibodies, lysozyme and chymotrypsinogen A. *Journal of Chromatography A*, 1217(35), 5610-5621. doi:<https://doi.org/10.1016/j.chroma.2010.06.064>
- Hanke, A. T., & Ottens, M. (2014). Purifying biopharmaceuticals: knowledge-based chromatographic process development. *Trends in Biotechnology*, 32(4), 210-220. doi:<https://doi.org/10.1016/j.tibtech.2014.02.001>
- Hansen, E., & Mollerup, J. M. (2004). The influence of retention on the plate height in ion-exchange chromatography. *Separation Science and Technology*, 39(9), 2011-2030. doi:<https://doi.org/10.1081/Ss-120037393>
- Hardin, A. M., Harinarayan, C., Malmquist, G., Axen, A., & van Reis, R. (2009). Ion exchange chromatography of monoclonal antibodies: effect of resin ligand density on dynamic binding capacity. *Journal of Chromatography A*, 1216(20), 4366-4371. doi:<https://doi.org/10.1016/j.chroma.2008.08.047>
- Hardin, A. M., & Ivory, C. F. (2006). Buffer salt effect on pH in the interior of an anion exchange resin. *Journal of Colloid and Interface Science*, 302(2), 560-567. doi:<https://doi.org/10.1016/j.jcis.2006.06.055>
- Hartvig, R. A., van de Weert, M., Østergaard, J., Jorgensen, L., & Jensen, H. (2011). Protein adsorption at charged surfaces: the role of electrostatic interactions and interfacial charge regulation. *Langmuir*, 27(6), 2634-2643. doi:<https://doi.org/10.1021/la104720n>
- Hedrich, J., Wittkopp, F., & Frech, C. (2020). *Determining mass transfer coefficients from linear gradient experiments*. Institute of Biochemistry. Manuscript in preparation.
- Hückel, E., & Debye, P. (1923). The theory of electrolytes. *Physikalische Zeitschrift*, 24, 185-206.
- Ishihara, T., Kadoya, T., & Yamamoto, S. (2007). Application of a chromatography model with linear gradient elution experimental data to the rapid scale-up in ion-

- exchange process chromatography of proteins. *Journal of Chromatography A*, 1162(1), 34-40. doi:<http://dx.doi.org/10.1016/j.chroma.2007.03.016>
- Ishihara, T., & Yamamoto, S. (2005). Optimization of monoclonal antibody purification by ion-exchange chromatography. *Journal of Chromatography A*, 1069(1), 99-106. doi:<http://dx.doi.org/10.1016/j.chroma.2004.10.040>
- Jansen, M. L., Straathof, A. J. J., Wielen, L. A. M. v. d., Luyben, K. C. A. M., & Tweel, W. J. J. v. d. (1996). Rigorous model for ion exchange equilibria of strong and weak electrolytes. *AIChE Journal*, 42, 1911-1924. doi:<https://doi.org/10.1002/aic.690420712>
- Kaltenbrunner, O., Giaverini, O., Woehle, D., & Asenjo, J. A. (2007). Application of chromatographic theory for process characterization towards validation of an ion-exchange operation. *Biotechnology and Bioengineering*, 98(1), 201-210. doi:<https://doi.org/10.1002/bit.21358>
- Kawakita, T., & Matsuishi, T. (1991). Elution kinetics of lysine from a strong cation-exchange resin with ammonia water. *Separation Science and Technology*, 26(7), 991-1003. doi: <https://doi.org/10.1080/01496399108050509>
- Khawli, L. A., Goswami, S., Hutchinson, R., Kwong, Z. W., Yang, J., Wang, X., . . . Motchnik, P. (2010). Charge variants in IgG1. *mAbs*, 2(6), 613-624. doi:<https://doi.org/10.4161/mabs.2.6.13333>
- Kluters, S. (2016). *Modeling of pH and solvent modulated chromatography for the purification of biopharmaceuticals*. (Ph.D.), University of Heidelberg, Mannheim
- Kluters, S., Wittkopp, F., Jöhnck, M., & Frech, C. (2016). Application of linear pH gradients for the modeling of ion exchange chromatography: Separation of monoclonal antibody monomer from aggregates. *Journal of Separation Science*, 39(4), 663-675. doi: <https://doi.org/10.1002/jssc.201500994>
- Kopaciewicz, W., Rounds, M. A., Fausnaugh, J., & Regnier, F. E. (1983). Retention model for high-performance ion-exchange chromatography. *Journal of Chromatography A*, 266, 3-21. doi:[https://doi.org/10.1016/S0021-9673\(01\)90875-1](https://doi.org/10.1016/S0021-9673(01)90875-1)
- Kozlowski, L. P. (2016). IPC – Isoelectric Point Calculator. *Biology Direct*, 11(1), 55. doi:<https://doi.org/10.1186/s13062-016-0159-9>
- Kröner, F., & Hubbuch, J. (2013). Systematic generation of buffer systems for pH gradient ion exchange chromatography and their application. *Journal of Chromatography A*, 1285, 78-87. doi:<http://dx.doi.org/10.1016/j.chroma.2013.02.017>
- Kullasakboonsri, R. (2016). *Untersuchung zum Elutionsverhalten verschiedenen Antikörperfragmente auf Kationenaustauscher*. (Bachelor's Degree), Mannheim University of Applied Sciences, Mannheim.
- Kumar, V., Leweke, S., von Lieres, E., & Rathore, A. S. (2015). Mechanistic modeling of ion-exchange process chromatography of charge variants of monoclonal antibody products. *Journal of Chromatography A*, 1426, 140-153. doi:<https://doi.org/10.1016/j.chroma.2015.11.062>
- Langford, J. F., Xu, X., Yao, Y., Maloney, S. F., & Lenhoff, A. M. (2007). Chromatography of proteins on charge-variant ion exchangers and implications for optimizing protein uptake rates. *Journal of Chromatography A*, 1163(1), 190-202. doi:<https://doi.org/10.1016/j.chroma.2007.06.028>

- Lee, Y., Jöhnck, M., & Frech, C. (2017). Evaluation of differences between dual salt-pH gradient elution and mono gradient elution using a thermodynamic model: Simultaneous separation of six monoclonal antibody charge and size variants on preparative-scale ion exchange chromatographic resin. *Biotechnology Progress*, 0(0). doi:<https://doi.org/10.1002/btpr.2626>
- Lee, Y. F., Graalfs, H., & Frech, C. (2016). Thermodynamic modeling of protein retention in mixed-mode chromatography: An extended model for isocratic and dual gradient elution chromatography. *Journal of Chromatography A*, 1464, 87-101. doi:<http://dx.doi.org/10.1016/j.chroma.2016.08.026>
- Liu, L. (2015). Antibody Glycosylation and Its Impact on the Pharmacokinetics and Pharmacodynamics of Monoclonal Antibodies and Fc-Fusion Proteins. *Journal of Pharmaceutical Sciences*, 104(6), 1866-1884. doi:<https://doi.org/10.1002/jps.24444>
- Lu, H.-L., Lin, D.-Q., Gao, D., & Yao, S.-J. (2013). Evaluation of immunoglobulin adsorption on the hydrophobic charge-induction resins with different ligand densities and pore sizes. *Journal of Chromatography A*, 1278, 61-68. doi:<https://doi.org/10.1016/j.chroma.2012.12.054>
- Marichal-Gallardo, P. A., & Álvarez, M. M. (2012). State-of-the-art in downstream processing of monoclonal antibodies: Process trends in design and validation. *Biotechnology Progress*, 28(4), 899-916. doi:<https://doi.org/10.1002/btpr.1567>
- Mollerup, J. M. (2008). A review of the thermodynamics of protein association to ligands, protein adsorption, and adsorption Isotherms. *Chemical Engineering & Technology*, 31(6), 864-874. doi:<https://doi.org/10.1002/ceat.200800082>
- Mollerup, J. M. (2014). Chemical engineering thermodynamics protein adsorption chromatography. *Journal of Chemical & Engineering Data*, 59(4), 991-998. doi:<https://doi.org/10.1021/je400739j>
- Mollerup, J. M., Breil, M. P., Vogelpohl, C., & Sadowski, G. (2011). Simultaneous correlation of hydrophobic interactions in HIC and protein solubility in aqueous salt solutions and mixed solvents. *Fluid Phase Equilibria*, 301(2), 163-170. doi:<https://doi.org/10.1016/j.fluid.2010.11.028>
- Mollerup, J. M., Hansen, T. B., Frederiksen, S. S., & Staby, A. (2010). Thermodynamic modeling of chromatographic separation. *Advances in Chromatography*, 48, 57-97. doi:<https://doi.org/10.1201/9781420084542>
- Mollerup, J. M., Hansen, T. B., Kidal, S., & Staby, A. (2008). Quality by design—Thermodynamic modelling of chromatographic separation of proteins. *Journal of Chromatography A*, 1177(2), 200-206. doi:<https://doi.org/10.1016/j.chroma.2007.08.059>
- Monnet, C., Jorieux, S., Souyris, N., Zaki, O., Jacquet, A., Fournier, N., . . . Fontayne, A. (2014). Combined glyco- and protein-Fc engineering simultaneously enhance cytotoxicity and half-life of a therapeutic antibody. *mAbs*, 6(2), 422-436. doi:<https://doi.org/10.4161/mabs.27854>
- Osberghaus, A., Hepbildikler, S., Nath, S., Haindl, M., von Lieres, E., & Hubbuch, J. (2012). Determination of parameters for the steric mass action model—A comparison between two approaches. *Journal of Chromatography A*, 1233, 54-65. doi:<http://dx.doi.org/10.1016/j.chroma.2012.02.004>

- Pedersen, L. (2003). *Modeling Retention Volumes, Isotherms and Plate Heights for Whey Proteins in Anion-Exchange Chromatography*. (Ph.D.), Technical University of Denmark,
- Pedersen, L., Mollerup, J., Hansen, E., & Jungbauer, A. (2003). Whey proteins as a model system for chromatographic separation of proteins. *Journal of Chromatography B*, 790(1-2), 161-173. doi: [https://doi.org/10.1016/s1570-0232\(03\)00127-2](https://doi.org/10.1016/s1570-0232(03)00127-2)
- Pérez, J. S., & Frey, D. D. (2005). Behavior of the Inadvertent pH Transient Formed by a Salt Gradient in the Ion-Exchange Chromatography of Proteins. *Biotechnology Progress*, 21(3), 902-910. doi:<https://doi.org/10.1021/bp040025s>
- Pfister, D., & Morbidelli, M. (2015). Mass transfer coefficients determination from linear gradient elution experiments. *Journal of Chromatography A*, 1375, 42-48. doi:<https://doi.org/10.1016/j.chroma.2014.11.068>
- Pfister, D., Steinebach, F., & Morbidelli, M. (2015). Linear isotherm determination from linear gradient elution experiments. *Journal of Chromatography A*, 1375, 33-41. doi:<https://doi.org/10.1016/j.chroma.2014.11.067>
- Pitzer, K. S. (1991). *Activity coefficients in electrolyte solution*. Boca Raton: CRC Press.
- Prausnitz, J. M. L., R.N.; Azevedo, E. G. (1999). *Molecular Thermodynamics of Fluid Phase Equilibria* (Third Edition ed.). New Jersey: Prentice-Hall Inc.
- Rathore, A. S., Kumar, D., & Kateja, N. (2018). Recent developments in chromatographic purification of biopharmaceuticals. *Biotechnology Letters*, 40(6), 895-905. doi:<https://doi.org/10.1007/s10529-018-2552-1>
- Rischawy, F., Saleh, D., Hahn, T., Oelmeier, S., Spitz, J., & Kluters, S. (2019). Good modeling practice for industrial chromatography: Mechanistic modeling of ion exchange chromatography of a bispecific antibody. *Computers & Chemical Engineering*, 130, 106532. doi: <https://doi.org/10.1016/j.compchemeng.2019.106532>
- Rosenoer, V. M., Oratz, M., & Rothschild, M. A. (2015). *Albumin: Structure, Function and Uses*. Saint Louis: Elsevier Science.
- Roth, C. M., & Lenhoff, A. M. (1993). Electrostatic and van der Waals contributions to protein adsorption: computation of equilibrium constants. *Langmuir*, 9(4), 962-972. doi:<https://doi.org/10.1021/la00028a015>
- Roth, C. M., & Lenhoff, A. M. (1995). Electrostatic and van der Waals Contributions to Protein Adsorption: Comparison of Theory and Experiment. *Langmuir*, 11(9), 3500-3509. doi:<https://doi.org/10.1021/la00009a036>
- Roush, D., Asthagiri, D., Babi, D. K., Benner, S., Bilodeau, C., Carta, G., . . . Zavalov, O. (2020). Toward in silico CMC: An industrial collaborative approach to model-based process development. *Biotechnology and Bioengineering*, n/a(n/a). doi:<https://doi.org/10.1002/bit.27520>
- Rüdt, M., Gillet, F., Heege, S., Hitzler, J., Kalbfuss, B., & Guélat, B. (2015). Combined Yamamoto approach for simultaneous estimation of adsorption isotherm and kinetic parameters in ion-exchange chromatography. *Journal of Chromatography A*, 1413(Supplement C), 68-76. doi:<https://doi.org/10.1016/j.chroma.2015.08.025>

- Salis, A., Bostrom, M., Medda, L., Cugia, F., Barse, B., Parsons, D. F., . . . Monduzzi, M. (2011). Measurements and theoretical interpretation of points of zero charge/potential of BSA protein. *Langmuir*, 27(18), 11597-11604. doi:<https://doi.org/10.1021/la2024605>
- Schellekens, H. (2005). Factors influencing the immunogenicity of therapeutic proteins. *Nephrology Dialysis Transplantation*, 20(suppl_6), vi3-vi9. doi:<https://doi.org/10.1093/ndt/gfh1092>
- Schmidt-Traub, H., Schulte, M., & Seidel-Morgenstern, A. (2012). *Preparative Chromatography* (H. Schmidt-Traub, Trans. Second Edition ed.). Weinheim: Wiley-VCH.
- Schmidt, M., Hafner, M., & Frech, C. (2014). Modeling of salt and pH gradient elution in ion-exchange chromatography. *Journal of Separation Science*, 37(1-2), 5-13. doi:<https://doi.org/10.1002/jssc.201301007>
- Seidel-Morgenstern, A. (1995). *Mathematische Modellierung der präparativen Flüssigchromatographie*: DUV, Dt. Univ.-Verlag.
- Shen, H., & Frey, D. D. (2004). Charge regulation in protein ion-exchange chromatography: Development and experimental evaluation of a theory based on hydrogen ion Donnan equilibrium. *Journal of Chromatography A*, 1034(1), 55-68. doi:<https://doi.org/10.1016/j.chroma.2004.01.039>
- Shen, H., & Frey, D. D. (2005). Effect of charge regulation on steric mass-action equilibrium for the ion-exchange adsorption of proteins. *Journal of Chromatography A*, 1079(1), 92-104. doi:<https://doi.org/10.1016/j.chroma.2005.02.086>
- Ståhlberg, J. (1999). Retention models for ions in chromatography. *Journal of Chromatography A*, 855(1), 3-55. doi:[https://doi.org/10.1016/S0021-9673\(99\)00176-4](https://doi.org/10.1016/S0021-9673(99)00176-4)
- Ståhlberg, J., & Jönsson, B. (1996). Influence of Charge Regulation in Electrostatic Interaction Chromatography of Proteins. *Analytical Chemistry*, 68(9), 1536-1544. doi:<https://doi.org/10.1021/ac9509972>
- Stephen Hunt, T. L., Robert Todd. (2017). Modeling Preparative Cation Exchange Chromatography of Monoclonal Antibodies. In *Preparative Chromatography for Separation of Proteins* (pp. 399-427).
- Strube, J., Grote, F., Josch, J. P., & Ditz, R. (2011). Process Development and Design of Downstream Processes. *Chemie Ingenieur Technik*, 83(7), 1044-1065. doi:<https://doi.org/10.1002/cite.201100017>
- Thomas, H., Coquebert de Neuville, B., Storti, G., Morbidelli, M., Joehnck, M., & Schulte, M. (2013). Role of tentacles and protein loading on pore accessibility and mass transfer in cation exchange materials for proteins. *Journal of Chromatography A*, 1285(Supplement C), 48-56. doi:<https://doi.org/10.1016/j.chroma.2013.01.104>
- Urbansky, E. T., & Schock, M. R. (2000). Understanding, Deriving, and Computing Buffer Capacity. *Journal of Chemical Education*, 77(12), 1640. doi:<https://doi.org/10.1021/ed077p1640>
- Urmann, M., Graalfs, H., Joehnck, M., Jacob, L. R., & Frech, C. (2010). Cation-exchange chromatography of monoclonal antibodies: Characterization of a

- novel stationary phase designed for production-scale purification. *mAbs*, 2(4), 395-404. doi: <https://doi.org/10.4161/mabs.2.4.12303>
- van Beers, M. M. C., & Bardor, M. (2012). Minimizing immunogenicity of biopharmaceuticals by controlling critical quality attributes of proteins. *Biotechnology Journal*, 7(12), 1473-1484. doi: <https://doi.org/10.1002/biot.201200065>
- van Deemter, J. J., Zuiderweg, F. J., & Klinkenberg, A. (1995). Longitudinal diffusion and resistance to mass transfer as causes of nonideality in chromatography. *Chemical Engineering Science*, 50(24), 3869-3882. doi: [https://doi.org/10.1016/0009-2509\(96\)81813-6](https://doi.org/10.1016/0009-2509(96)81813-6)
- van den Bremer, E. T., Beurskens, F. J., Voorhorst, M., Engelberts, P. J., de Jong, R. N., van der Boom, B. G., . . . Parren, P. W. (2015). Human IgG is produced in a pro-form that requires clipping of C-terminal lysines for maximal complement activation. *mAbs*, 7(4), 672-680. doi: <https://doi.org/10.1080/19420862.2015.1046665>
- Váradi, C., Jakes, C., & Bones, J. (2020). Analysis of cetuximab N-Glycosylation using multiple fractionation methods and capillary electrophoresis mass spectrometry. *Journal of Pharmaceutical and Biomedical Analysis*, 180, 113035. doi: <https://doi.org/10.1016/j.jpba.2019.113035>
- Vo, B. S., & Shallcross, D. C. (2005). Ion exchange equilibria data for systems involving H⁺, Na⁺, K⁺, Mg²⁺, and Ca²⁺ ions. *Journal of Chemical & Engineering Data*, 50(3), 1018-1029. doi: <https://doi.org/10.1021/je0500173>
- Vo, B. S., & Shallcross, D. C. (2005). Modeling Solution Phase Behavior in Multicomponent Ion Exchange Equilibria Involving H⁺, Na⁺, K⁺, Mg²⁺, and Ca²⁺ Ions. *Journal of Chemical & Engineering Data*, 50(6), 1995-2002. doi: <https://doi.org/10.1021/je050232j>
- Wada, R., Matsui, M., & Kawasaki, N. (2019). Influence of N-glycosylation on effector functions and thermal stability of glycoengineered IgG1 monoclonal antibody with homogeneous glycoforms. *mAbs*, 11(2), 350-372. doi: <https://doi.org/10.1080/19420862.2018.1551044>
- Walsh, G. (2010). Post-translational modifications of protein biopharmaceuticals. *Drug Discovery Today*, 15(17), 773-780. doi: <https://doi.org/10.1016/j.drudis.2010.06.009>
- Walsh, G., & Jefferis, R. (2006). Post-translational modifications in the context of therapeutic proteins. *Nature Biotechnology*, 24(10), 1241-1252. doi: <https://doi.org/10.1038/nbt1252>
- Wang, G., Briskot, T., Hahn, T., Baumann, P., & Hubbuch, J. (2017). Root cause investigation of deviations in protein chromatography based on mechanistic models and artificial neural networks. *Journal of Chromatography A*, 1515, 146-153. doi: <https://doi.org/10.1016/j.chroma.2017.07.089>
- Wang, X., Guo, L., & Ma, H. (2009). Analysis of local polarity change around Cys34 in bovine serum albumin during N→B transition by a polarity-sensitive fluorescence probe. *Spectrochimica Acta, Part A: Molecular and Biomolecular Spectroscopy*, 73(5), 875-878. doi: <https://doi.org/10.1016/j.saa.2009.04.008>
- Westerberg, K., Broberg Hansen, E., Degerman, M., Budde Hansen, T., & Nilsson, B. (2012). Model-based process challenge of an industrial ion-exchange

- chromatography step. *Chemical Engineering & Technology*, 35(1), 183-190. doi: <https://doi.org/10.1002/ceat.201000560>
- Whitley, R. D., Wachter, R., Liu, F., & Wang, N. H. L. (1989). Ion-exchange equilibria of lysozyme myoglobin and bovine serum albumin: Effective valence and exchanger capacity. *Journal of Chromatography A*, 465(3), 137-156. doi: [https://doi.org/10.1016/S0021-9673\(01\)92653-6](https://doi.org/10.1016/S0021-9673(01)92653-6)
- Wilson, G. M. (1964). Vapor-liquid equilibrium. XI. A new expression for the excess free energy of mixing. *Journal of the American Chemical Society*, 86(2), 127-130. doi: <https://doi.org/10.1021/ja01056a002>
- Wittkopp, F., Peeck, L., Hafner, M., & Frech, C. (2018). Modeling and simulation of protein elution in linear pH and salt gradients on weak, strong and mixed cation exchange resins applying an extended Donnan ion exchange model. *Journal of Chromatography A*, 1545, 32-47. doi: <https://doi.org/10.1016/j.chroma.2018.02.020>
- Wrzosek, K., Gramblicka, M., & Polakovic, M. (2009). Influence of ligand density on antibody binding capacity of cation-exchange adsorbents. *Journal of Chromatography A*, 1216(25), 5039-5044. doi: <https://doi.org/10.1016/j.chroma.2009.04.073>
- Wu, D., & Walters, R. R. (1992). Effects of stationary phase ligand density on high-performance ion-exchange chromatography of proteins. *Journal of Chromatography A*, 598(1), 7-13. doi: [https://doi.org/10.1016/0021-9673\(92\)85108-6](https://doi.org/10.1016/0021-9673(92)85108-6)
- Wu, J., Jiao, P., Zhuang, W., Zhou, J., & Ying, H. (2016). Modified DIX model for ion-exchange equilibrium of l-phenylalanine on a strong cation-exchange resin. *Chinese Journal of Chemical Engineering*, 24(10), 1386-1391. doi: <https://doi.org/10.1016/j.ciche.2016.07.009>
- Yamamoto, S., & Ishihara, T. (1999). Ion-exchange chromatography of proteins near the isoelectric points. *Journal of Chromatography A*, 852(1), 31-36. doi: [https://doi.org/10.1016/S0021-9673\(99\)00593-2](https://doi.org/10.1016/S0021-9673(99)00593-2)
- Yamamoto, S., Nakanishi, K., Matsuno, R., & Kamijubo, T. (1983). Ion exchange chromatography of proteins—predictions of elution curves and operating conditions. II. Experimental verification. *Biotechnology and Bioengineering*, 25(5), 1373-1391. doi: <https://doi.org/10.1002/bit.260250516>
- Yamamoto, S., Nakanishi, K., Matsuno, R., & Kamikubo, T. (1983). Ion exchange chromatography of proteins—prediction of elution curves and operating conditions. I. Theoretical considerations. *Biotechnology and Bioengineering*, 25(6), 1465-1483. doi: <https://doi.org/10.1002/bit.260250605>
- Yamamoto, S., Watler, P. K., Feng, D., & Kaltenbrunner, O. (1999). Characterization of unstable ion-exchange chromatographic separation of proteins. *Journal of Chromatography A*, 852(1), 37-41. doi: [http://dx.doi.org/10.1016/S0021-9673\(99\)00592-0](http://dx.doi.org/10.1016/S0021-9673(99)00592-0)
- Yang, T., Sundling, M. C., Freed, A. S., Breneman, C. M., & Cramer, S. M. (2007). Prediction of pH-Dependent Chromatographic Behavior in Ion-Exchange Systems. *Analytical Chemistry*, 79(23), 8927-8939. doi: <https://doi.org/10.1021/ac071101j>

- Yoon, B. J., & Lenhoff, A. M. (1992). Computation of the electrostatic interaction energy between a protein and a charged surface. *The Journal of Physical Chemistry*, 96(7), 3130-3134. doi:<https://doi.org/10.1021/j100186a064>
- Zhang, F., Skoda, M. W., Jacobs, R. M., Martin, R. A., Martin, C. M., & Schreiber, F. (2007). Protein interactions studied by SAXS: effect of ionic strength and protein concentration for BSA in aqueous solutions. *Journal of Physical Chemistry B*, 111(1), 251-259. doi:<https://doi.org/10.1021/jp0649955>
- Zhang, Y. J., & An, H. J. (2017). Technologies and strategies for bioanalysis of biopharmaceuticals. *Bioanalysis*, 9(18), 1343-1347. doi:<https://doi.org/10.4155/bio-2017-4981>
- Zhao, Y. Y., Wang, N., Liu, W. H., Tao, W. J., Liu, L. L., & Shen, Z. D. (2016). Charge Variants of an Avastin Biosimilar Isolation, Characterization, In Vitro Properties and Pharmacokinetics in Rat. *PLoS One*, 11(3), e0151874. doi:<https://doi.org/10.1371/journal.pone.0151874>
- Zurawski, V. R., & Foster, J. F. (1974). Neutral transition and the environment of the sulfhydryl side chain of bovine plasma albumin. *Biochemistry*, 13(17), 3465-3471. doi:<https://doi.org/10.1021/bi00714a007>

8 APPENDIX

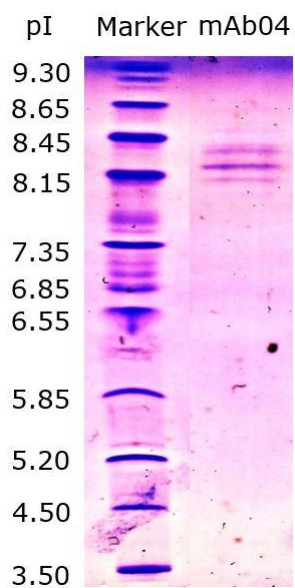


Figure 26. Isoelectric focusing of the antibody mAb04 sample. The monomer charge variants of mAb04 show different isoelectric points between 8.15 and 8.40.

9 CURRICULUM VITAE

PERSONAL DATA

Name: Gabriela Sánchez Reyes
Date of birth: 20.08.1990
Place of birth: Ciudad Victoria, Tamaulipas, Mexico
Family status: Single
Father: Humberto Gustavo Sánchez Morett
Mother: Martha Patricia Reyes Mata

SCHOOL CAREER

2003 – 2005 Colegio José de Escandón “La Salle”
30.06.2005 Middle School Degree (1.8)
2005 – 2008 Colegio José de Escandón “La Salle”
09.06.2008 High School Degree (1.8)

ACADEMIC CAREER

Winter semester Start of studies at Instituto Tecnológico y de Estudios Superiores de Monterrey “ITESM”
2008/2009 (Biotechnology Engineering)
20.12.2013 Bachelor of Science (2.4)
2014 – 2016 Master studies at University of Applied Sciences Mannheim
2016 Master Thesis (Influence of ligand density on the bind/elution behavior of antibody fragments in anion-exchange chromatography)
31.10.2016 Master of Science (1.5)

22.02.2017

Acceptance as Ph.D. candidate at the Medical Faculty
Mannheim of Ruprecht Karl University Heidelberg

10 ACKNOWLEDGMENT

First of all, I would like to express my appreciation and gratitude to Prof. Dr. Mathias Hafner for his support and the supervision of my doctoral thesis.

Special thanks to Prof. Christian Frech for this unique opportunity, as well as for his enthusiastic support, advice, and contribution to my work during my time at the Institute of Biochemistry at the University of Applied Sciences in Mannheim.

I would also like to thank Dr. Lars Peeck, Dr. Heiner Graalfs, Dr. Michael Schulte and Nina Weis at Merck KGaA, Darmstadt for the support on the entire project.

My sincere gratitude to my colleagues at the Institute of Biochemistry for their unconditional support and a pleasant working atmosphere. Especially to Dipl. Ing. Christiane Koch for all the laboratory guidance, not only for her technical expertise but for all the time and energy she gives to maintain the laboratory running. As well as, M.Sc. Carolin Stange for always being available inside and outside the lab. To Dr. Felix Wittkopp, thank you for shortly supervising my Master thesis. It was a pleasure working with you, and I am sure that our long discussions made me a better scientist. Thank you for believing in me and encouraging me to pursue a doctoral degree. And last but not least, to M.Sc. Jan Hedrich, thank you for tolerating my constant worrying and critical view of everything, especially of myself. I am thankful for the fruitful never-ending discussions and the much needed continuous support on MATLAB® programming.

Additionally, I would like to thank my friends and family because without their support, this journey would not have been possible. To all my friends scattered around the world, thank you for your thoughts, well-wishes, phone calls, e-mails, texts, visits, editing advice, and being there whenever I needed a friend. To my family, thank you for your unconditional encouragement to follow my dreams. I am especially grateful to my parents, who supported me emotionally and financially. Thank you for believing in me and wanting the best for me, always. Finally, my special gratitude goes to my partner M.Sc. Matthias Wagner, for always been there for me on all the ups and downs of this arduous journey. Thank you for encouraging me every single day and for making me laugh through the dark times.

“Gracias Totales.”

– Soda Stereo